THÈSE POUR OBTENIR LE GRADE DE DOCTEUR DE L'UNIVERSITÉ DE MONTPELLIER

En Mathématiques et modélisation

École doctorale I2S

Unité de recherche IMAG

Modeling, analysis and numerical simulation of the coagulation cascade

Présentée par Junyi Chen
le 16 Avril 2025

Sous la direction de Franck Nicoud

Devant le jury composé de

Pr. Franck Nicoud, Université de Montpellier	Direction de thèse
Pr. Yun Xu, Imperial College London	Rapporteur
Dr. Eléonore Riber, CERFACS, Toulouse	Examinateur
Dr. Joanne Dunster, University of Reading	Examinateur
Pr. Oscar Flores Arias, Carlos III University of Madrid	Rapporteur
Pr. Bijan Mohammadi, Université de Montpellier	Examinateur

UNIVERSITÉ DE MONTPELLIER

All models are wrong, but some are useful. - George E. P. Box

Abstract

Coagulation cascade is a series of biochemical processes critical for preventing bleeding and ensuring wound healing of which disorders lead to pathological issues. However, the existing coagulation models, often lacking experimental validation and simplification, present challenges in their practical application for understanding diseases such as thrombosis and haemophilia. This thesis focuses on mathematical modeling for the coagulation cascade, including optimizing parameters, model reduction, and finally application of venous thrombosis.

First, a novel optimizer of clotting factors using gradient-based and evolutionary optimization algorithms has been developed and used to fine-tune thrombin coagulation models. It is found that the types of models and selection of variables influence the complexity and the landscape significantly affects the optimization. The novel optimizer improves the efficiency to find the global minimum, especially for a very complex landscape.

An other achievement in this thesis is a multi-step reduction approach, simplifying large-scale coagulation models without compromising their predictive capability. This reduction approach combines the advantages of different reduction methods and reduces the size of coagulation models efficiently, while conserving the initial accuracy and robustness.

Finally, this thesis presents a 0-D coagulation model for venous thrombosis. This model incorporates time-dependent transport effects derived from mechanical features of 3-D simulations, along with biochemical interactions from the coagulation cascade. Simulations were conducted for both platelet-based and platelet-free models. The results highlight the critical influence of cascade stimulation, transport effects, and platelet involvement in the development of models for deep venous thrombosis.

Résumé

La cascade de coagulation est une série de processus biochimiques essentiels à la prévention des saignements et à la cicatrisation des plaies, dont les dysfonctionnements peuvent entraîner des pathologies graves. Cependant, les modèles actuels de coagulation, souvent dépourvus de validation expérimentale et simplifiés, posent des défis dans leur application pratique pour la compréhension des maladies telles que la thrombose et l'hémophilie. Cette thèse se concentre sur la modélisation mathématique de la cascade de coagulation, en abordant l'optimisation des paramètres, la réduction des modèles et, enfin, leur application à la thrombose veineuse.

Tout d'abord, un nouvel optimiseur des facteurs de coagulation, combinant des algorithmes d'optimisation basés sur le gradient et des stratégies évolutionnaires, a été développé et utilisé pour affiner les modèles de génération de thrombine. Il a été observé que le choix des modèles et la sélection des variables influencent fortement la complexité du paysage d'optimisation, ce qui impacte la recherche des minima globaux. Ce nouvel optimiseur améliore l'efficacité du processus en permettant d'identifier plus rapidement et plus précisément la solution optimale, en particulier dans des paysages complexes.

Un autre apport majeur de cette thèse est le développement d'une approche de réduction multi-étapes, permettant de simplifier les modèles de coagulation de grande taille sans compromettre leur capacité prédictive. Cette méthode exploite les avantages de différentes techniques de réduction et permet de diminuer efficacement la taille des modèles tout en préservant leur précision et leur robustesse initiales.

Enfin, cette thèse propose un modèle de coagulation 0-D appliqué à la thrombose veineuse. Ce modèle intègre des effets de transport dépendant du temps, dérivés des caractéristiques mécaniques issues de simulations 3-D, ainsi que les interactions biochimiques de la cascade de coagulation. Des simulations ont été réalisées pour des modèles avec et sans plaquettes. Les résultats mettent en évidence l'influence cruciale de la stimulation de la cascade, des effets de transport et de l'implication

des plaquettes dans le développement de modèles de thrombose veineuse profonde.

Contents

List of Figures

List of Tables

Acknowledgments

First and foremost, I would like to express my deepest gratitude to my supervisor, Prof. Franck Nicoud, for his guidance, support, and encouragement throughout this academic journey. His insightful advice and profound expertise support me to finish my research, and his mentorship has enriched my academic experience.

I extend my sincere appreciation to reviewers, Prof. Xu and Prof Arias and other jury members, Dr. Riber, Dr. Dunster and Prof. Mohammadi for their time, thoughtful feedback, and critical insights, which have greatly contributed to improving the quality of this thesis.

I am especially grateful to Éléonore and Quentin for their collaborative efforts, and to Barthelemy for generously providing essential data. I also appreciate Rojano Mendez, who patiently answered my questions at the beginning of this thesis.

My sincere thanks go to my team colleagues for their scientific discussions, technical assistance, and kind encouragement. They are Salomé, Morgan, Aurelio, Corentin, Pierre, Pierre-Louis, Francisco, Pascal, and Ougzan. In particularly, I would like to thank Simon Mendez for his support and for managing the team so effectively.

A special thanks to the dedicated lab staff, Nathalie, Céline, Brigitte, Sofia, and Baptiste, whose expertise and support have been vital to maintaining a productive and stable research environment.

Additionally, I extend my gratitude to my lab colleagues, Juliette, Chloé, Yefei, Tiziri, Pablo, Pierrick, Nikolas, Sofian, Antoine, Adam, Axel, Baptiste, Guillaume, Grégoire, Hermes, Luca, Victor, Ulysse, Tanguy, Trung, Yufei, and King Leung, for their friendship and collaboration. I would also like to acknowledge my office mates, Zanneb, Luca, Pascal and Pierrick, for their companionship from sunrise to sunset.

Beyond the academic and work aspect, I am grateful to my family and friends for their love, understanding, and encouragement during this challenging period. To my parents, thank you for your infinite love and support and for being my strong pillar. I also deeply appreciate my big family members for their care and encouragement, including my grandparents, my aunts, my uncles and my cousins.

I am especially thankful to my friends met in France and Europe, including Wanjun Chen, Laijiao Lan, Xiaoxuan Pei, Yucheng Peng, Ruihua Wang, Zixi Wang, Ting Wu, Mengyan Xu, Yang Yang, Yuedi Zeng, Romain, Chenghe Piao, Yuxuan

Xi, Guangqi Zhang, Jinghao Lu, Yilun Wang, Jing Zhu, Enrui Zhang, and Bikai Zhuang, for their friendship and support. Likewise, I extend my gratitude to my friends in China - Shujun Liu, Yaxin Zhang, Renjie Hao, He Su, Yanwei Liang, Xiang Guan, and Yunhao Li, Xinyu Zhao and Qi Zhang, for their kindness and ongoing encouragement.

Finally, to everyone who has contributed in any way to the successful completion of this thesis - your support and advice have not only enriched this work but have also played a crucial role in my personal and professional growth. Thank you.

C'est la vie.

Chapter 1

Introduction

1.1 Backgrounds and motivations

Hemostasis is a complex physiological process that ensures vascular healing under various conditions such as injury and trauma, as well as the proper flow of blood throughout the vascular tree. It relies primarily on the interplay between blood cells (platelets, red and white blood cells), and the coagulation cascade, which together lead to the formation of thrombus when required plugs. Disorders in hemostasis can result in bleeding or thrombosis, which leads to mortality. Central to this process is the coagulation cascade, a critical biochemical pathway that leads to the activation of clotting factors, ultimately resulting in the formation of fibrin strands and the stabilization of the platelet plug.

Over the past decades, mathematical and computational modeling has emerged as a powerful tool for understanding and developing the sophisticated mechanisms of coagulation cascade. When numerical models align with empirical data, they validate existing knowledge; when discrepancies arise, they highlight opportunities for discovering new pathways and mechanisms.

Coagulation modeling efforts have spanned a wide range of approaches, from differential equations to more sophisticated systems for closed and flow-based conditions [17]. Widely accepted models [18, 15, 19, 20] have significantly advanced our understanding of coagulation. A lack of comprehensive validation against experimental data undermines the reliability of the models and limits their clinical applicability [21]. Additionally, the complexity of some models hinders their accessibility and practical use in research and clinical settings [22].

To address these challenges, this thesis focuses on three key topics: parameter optimization, model reduction, and the 0-D modeling under flow for venous valves, based on Ordinary Differential Equations (ODEs). This work aims to enhance the understanding of coagulation mechanisms while improving their computational and clinical applicability.

1.2 Introduction to haemostasis and thrombosis biology

Hemostasis involves the formation of a blood clot inside a blood vessel to seal injuries and prevent excessive bleeding. The clotting process is critical for maintaining vascular integrity as illustrated in Figure 1.1. In contrast, thrombosis occurs when clot formation obstructs blood flow in the circulatory system. This obstruction disrupts vessels and organs, such as the heart and brain, leading to severe conditions like stroke, heart attack, or deep vein thrombosis [23, 4]. As illustrated in Figure 1.1, the coagulation cascade produces thrombin and converts fibrinogen into fibrin (secondary hemostasis). Before this, primary hemostasis occurs as circulating platelets adhere to the injury site through various biochemical interactions. This adhesion activates the platelets, enabling them to aggregate with others via fibrinogen to form an initial plug. However, this plug is not robust and requires reinforcement by fibrin strands for structural stability and strength.

1.2.1 Components of clotting formation

1. **Platelets**: These small blood cells play an important role in hemostasis and thrombosis. When a blood vessel is damaged, platelets are activated and aggregate at the injury site to form a temporary "platelet plug." Once activated, the platelets surfaces provide biding sites for further activation of clotting factors [24].

2. **Red blood cells**: Red blood cells (RBCs) play a complex role in hemostasis and thrombosis. RBCs impact thrombosis through multiple pathways like modulating viscosity. These effects are largely pro-thrombotic, though RBCs can exert both pro- and anti-thrombotic influences [25].

3. **Clotting Factors**: Within the liver, hepatocytes are involved in the synthesis of most clotting factors also called coagulation factors, mostly circulating in an inactive form in the blood [25]. When triggered by injury or contact to

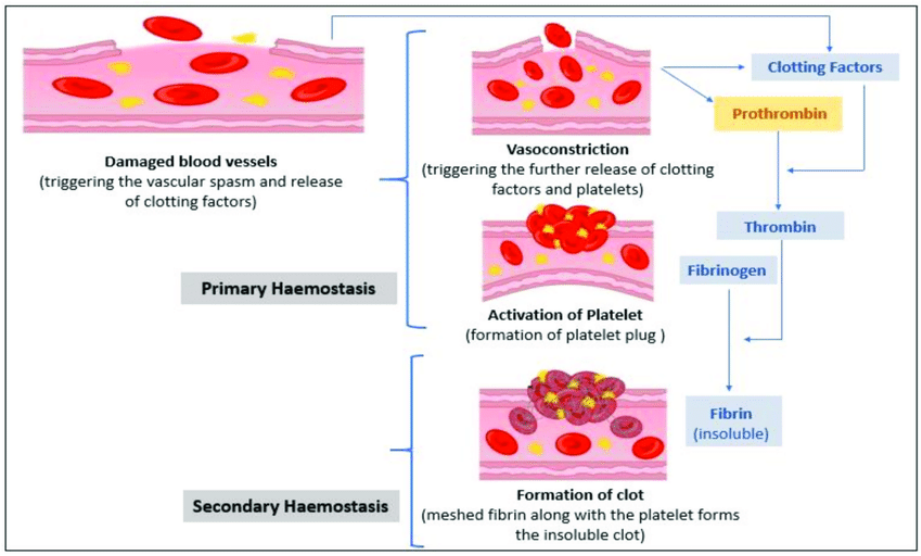

Figure 1.1: The process of clotting formation. Initially, a damaged blood vessel releases clotting factors, initiating the cascade. Prothrombin is converted into thrombin, which then transforms soluble fibrinogen into insoluble fibrin strands. Activated platelets form a platelet plug to limit blood flow, while fibrin strands adhere to the platelet plug, strengthening it and forming an insoluble blood clot. Adapted from [1].

negatively charged surfaces, they undergo a series of activation in the thrombin generation [26].

4. **Fibrin**: Fibrin along with activated platelets form stable clots. The fibrin generated from fibrinogen is activated by thrombin. Meanwhile, thrombin activates factor XIII which promotes fibrin cross-links. After this, fibrinolysis starts to dissolve clot, as a therapeutic approach to deal with thrombosis [27].

1.3 Introduction to coagulation cascade

The coagulation cascade consists of a series of enzymatic reactions that involve both the intrinsic and extrinsic pathways, leading to the production of thrombin which activates platelets and converse fibrinogen into fibrin, two structural components of clot [28] as shown in Figure 1.2. Both extrinsic pathway and intrinsic pathway serve as the initial trigger for coagulation, rapidly producing small amounts of thrombin. This thrombin activates other components of the coagulation cascade, such as factor V, factor VIII, and platelets, to propagate the clotting process through several

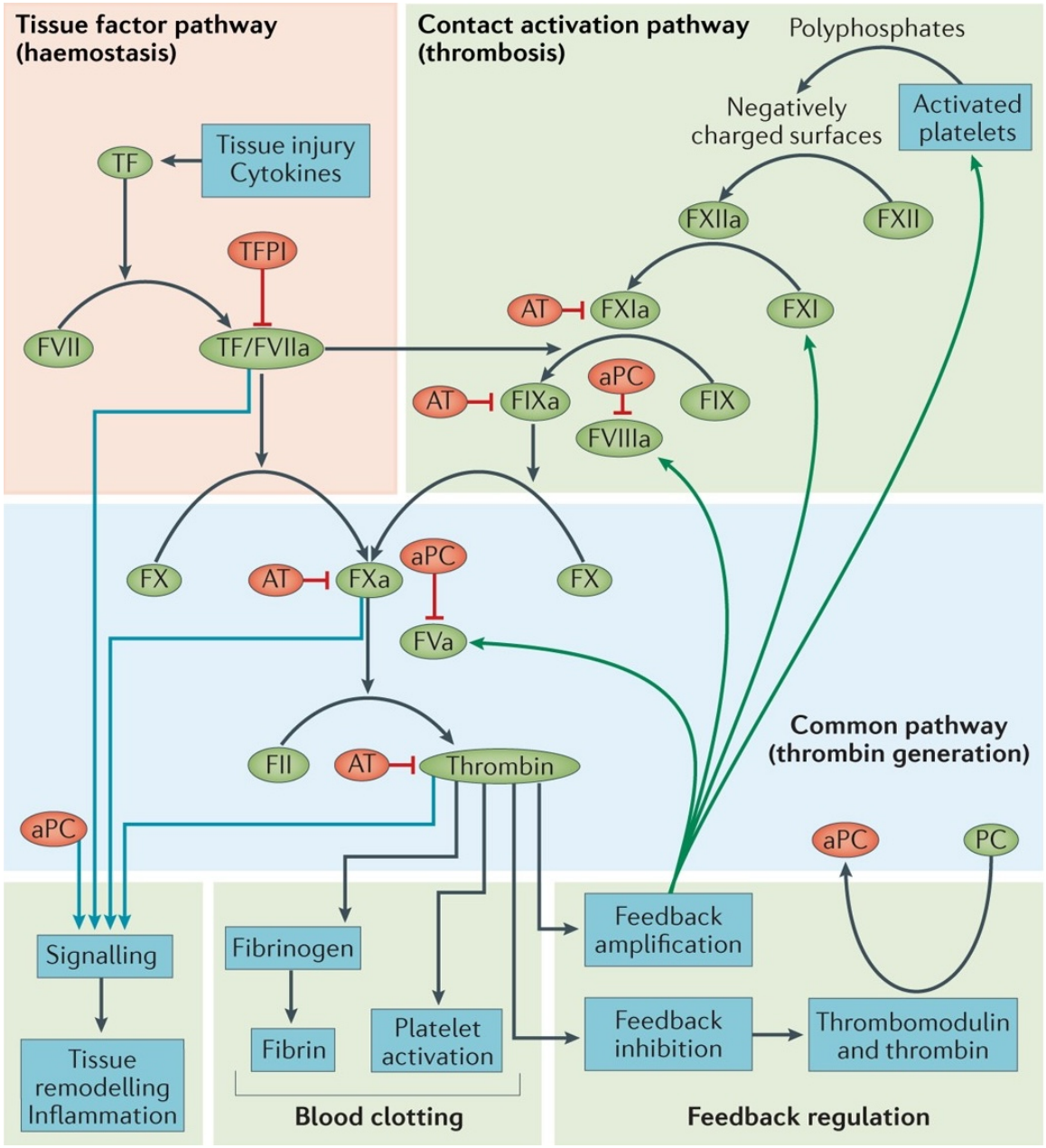

Figure 1.2: The coagulation cascade scheme. The system consists of two pathways to trigger: the tissue factor (TF) pathway and the contact activation pathway. Both converges at the activation of Xa to generate thrombin. (Abbreviations: a = activated; F = factor; PC = protein C). Adapted from [2].

feedback amplification loops.

1.3.1 The extrinsic pathway

The extrinsic pathway, also known as the tissue factor (TF) pathway, is initiated when blood is exposed to TF as shown in Figure 1.1. This exposure occurs due to vascular injury disrupting the endothelial layer. The process of extrinsic pathway is indicated in Figure 1.2. TF binds to factor VII, forming the TF=VII complex which converts factor VII to its active form, factor VIIa, in a calcium-dependent manner. The TF=VIIa complex plays a dual role in the coagulation cascade. It directly activates factor X to its active form factor Xa, which enters the common pathway and initiates the conversion of prothrombin to thrombin. It also activates factor IX to factor IXa, which subsequently amplifies thrombin production by forming the tenase complex (IXa=VIIIa) with factor VIIIa.

The extrinsic pathway is regulated to prevent excessive clotting. The pathway is regulated by tissue factor pathway inhibitor (TFPI), which limits excessive activation by binding to and inhibiting the TF=VIIa complex and factor Xa. Additionally, antithrombin III (ATIII), a serine protease inhibitor, plays a critical role in regulating the coagulation cascade by neutralizing thrombin, factor Xa, and other activated clotting factors.

1.3.2 The intrinsic pathway

Typically, as shown in Figure 1.3, the intrinsic pathway of coagulation is initiated upon contact with negatively charged surfaces, such as in medical devices with help of prekallikrein (PK).

As shown in Figure 1.2, this contact triggers the activation of factor XII, which undergoes auto-activation to form XIIa through surface adsorption. The next step involves the activation of factor XI to XIa by XIIa. factor XIa plays a pivotal role in propagating the coagulation cascade by activating factor IX to IXa. Activated factor IX (IXa), in conjunction with its cofactor VIIIa forms the tenase complex (IXa=VIIIa). This complex is crucial for catalysing the conversion of factor X to Xa, a key enzymatic step that bridges the intrinsic and common pathways. The tenase complex significantly amplifies thrombin production, ensuring a rapid and efficient clotting response. High molecular weight kininogen (HMWK) acts as a cofactor during these reactions, enhancing XIIa generation and further strengthening the activation signal [29]. The intrinsic pathway is regulated by feedback loops and

cofactor involvement ensuring robust thrombin generation in response to injury.

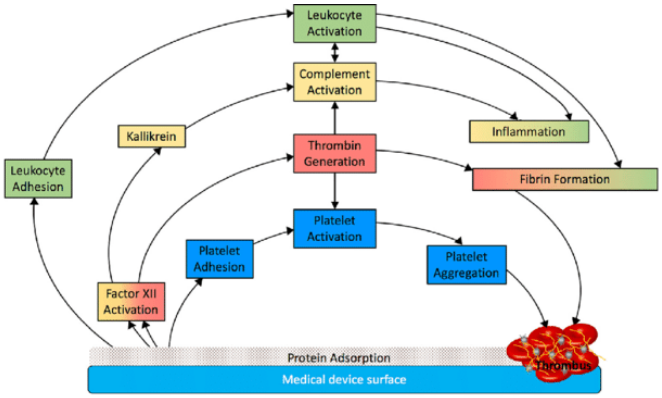

Figure 1.3: Blood contacting medical device associated thrombosis. Adapted from [3].

1.3.3 The common pathway

Both the intrinsic and extrinsic pathways converge at the common pathway, with factor Xa serving as the link. factor Xa, in complex with factor Va, calcium ions, and phospholipids, forms the prothrombinase complex (Xa=Va). This complex converts prothrombin (factor II) into its active form, thrombin, which is the key enzyme in the coagulation cascade. Thrombin is responsible for several critical functions, including the conversion of fibrinogen (factor I) into fibrin (factor Ia), cross-linking fibrin to stabilize clots, and initiating feedback mechanisms that further amplify the coagulation cascade.

1.3.4 Feedback mechanisms

Thrombin not only plays a central role in clot formation but also amplifies the cascade through positive feedback loops. Thrombin activates V, VIII, and XI, accelerating the production of thrombin and further amplifying the cascade. Thrombin also activates platelets, promoting platelet aggregation and the formation of a stable platelet plug. To prevent excessive clotting, the body has several negative feedback that regulate the coagulation cascade. These include inhibition of the TF=VIIa=Xa complex by tissue factor pathway inhibitor (TFPI), inhibition of multiple coagulation factors by antithrombin (ATIII), and proteolytic inactivation of Va and VIIIa by activated protein C (aPC) [30].

1.3.5 Fibrin formation and fibrinolysis

Fibrin formation is the final step of the coagulation cascade and plays a critical role in stabilizing blood clots. Once thrombin is generated in the common pathway, it converts fibrinogen (factor I), a soluble plasma glycoprotein, into fibrin monomers [28]. These monomers spontaneously polymerize to form insoluble fibrin strands, creating the structural scaffold of the clot. To stabilize the fibrin network, thrombin also activates factor XIII to factor XIIIa. This enzyme cross-links fibrin strands by forming covalent bonds between glutamine and lysine residues, increasing the mechanical strength and resistance of the clot to enzymatic degradation [28]. Fibrin serves as a meshwork that entraps platelets, red blood cells, and other components, reinforcing the hemostatic plug and preventing further blood loss.

Fibrinolysis is the process by which fibrin clots are degraded after their formation, restoring normal blood flow and preventing excessive clot accumulation [27]. This process is primarily mediated by the enzyme plasmin, which breaks down fibrin into soluble fibrin degradation products (FDPs). The balance between fibrin formation and fibrinolysis is essential for maintaining vascular integrity and preventing pathological condition.

1.4 Pathological bleeding disorders

There are many abnormalities associated with the blood clotting system. These abnormalities can be divided into two families depending on the blood clotting scenario: excessive clotting (thrombosis) and insufficient clotting (bleeding) as shown in Table 1.1. In this section, some disorders of blood coagulation are presented. Thrombosis results in the formation of a blood clot, also known as thrombus. They can results in the complete or partial occlusion of the vessel. Alternatively, they can detach and migrate with the flow causing the occlusion of smaller vessels in the circulatory system. This is a serious medical condition known as embolism and can potentially lead to dangerous complications (e.g. stroke).

1.4.1 Deep vein thrombosis

Deep vein thrombosis (DVT) is a condition where the clots form in deep veins, most commonly in the legs, possibly causing swelling, pain and discoloration of skin. This condition can be dangerous because the clot may travel through the blood stream to the lungs, causing a pulmonary embolism (PE). DVT begins with

Table 1.1:: Classification of blood clotting disorders and their potential causes.

Clotting disorder	**Causes**
Excessive clotting (Thrombosis)	
Deep venous thrombosis (DVT)	Prolonged immobility, surgery, genetic factors
Arterial thrombosis	Atherosclerosis, hypertension
Pulmonary embolism	DVT, hypercoagulability
Vessel occlusion	Atherosclerosis, trauma, vasculitis
Cancer-associated thrombosis	malignancies, chemotherapy
Inflammatory disease thrombosis	Autoimmune diseases, chronic inflammation
Inflammatory disease	chronic systemic inflammation
Insufficient clotting	
Hemophilia	Genetic deficiency in clotting factors (e.g., VIII or IX)
Anticoagulant therapy	Use of anticoagulants (e.g., warfarin, heparin) for medical treatment

the slow activation of the coagulation cascade, often due to endothelial injury or stasis. Figure 1.4 illustrates the mechanisms underlying venous valve function and dysfunction, distinguishing between healthy and pathological states. In the healthy valve cycle, effective muscle pump action generates sufficient oscillatory blood flow, which clears residual molecular and cells. Conversely, in the pathological valve cycle, weak muscle pump action leads to insufficient oscillatory flow, creating a hypoxic environment for accumulating cells and proteins.

1.4.2 Haemophilia

Haemophilia is a genetic disorder that impairs the body's ability to form thrombin, leading to excessive bleeding even from minor injuries. Individuals with haemophilia often experience spontaneous bleeding into joints, muscles, and soft tissues [31]. Haemophilia are classified into:

1. **Haemophilia A**: This is the most common form, caused by a deficiency of VIII, leading to improper activation of X and thus impaired thrombin generation and reduced fibrin formation for further clot formation.

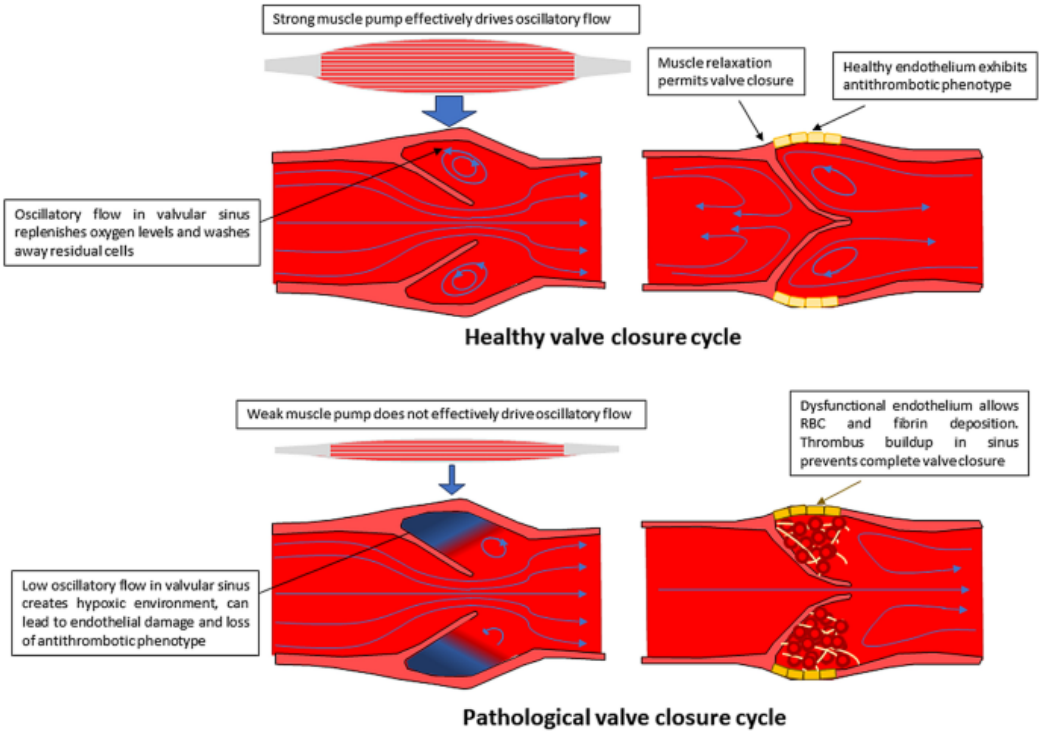

Figure 1.4: Schematic representation of venous valve function and dysfunction. The venous valve possessing antithrombotic properties, operates under oscillatory blood flow. Top left: The valve is open, allowing blood to flow unidirectionally from the lower extremities to the veins. Top right: The valve is closed, preventing retrograde blood flow (reflux). Bottom left: Weakened blood flow fails to transfer blood to the valve sinus, impairing endothelial function. Bottom right: Damaged endothelium fosters thrombus formation in sinus. Adapted from [4].

2. **Haemophilia B**: Also known as Christmas disease, this is caused by a deficiency in IX. Since factor IX is crucial for activating factor X, a deficiency similarly weakens the clotting process.

3. **Haemophilia C**: This is a rarer form caused by a deficiency in XI. Unlike Haemophilia A and B, Haemophilia C usually affects thrombin production less severely.

1.4.3 Thrombosis and Virchow's Triad

The concept of Virchow's Triad, introduced by Rudolf Virchow in 19th century is commonly used to explain the interactions of different risk factors of thrombosis [32]. According to Virchow's Triad, three primary conditions in Figure 1.5—blood stasis, endothelial injury, and hypercoagulability, act together or individually to increase the risk of clot formation.

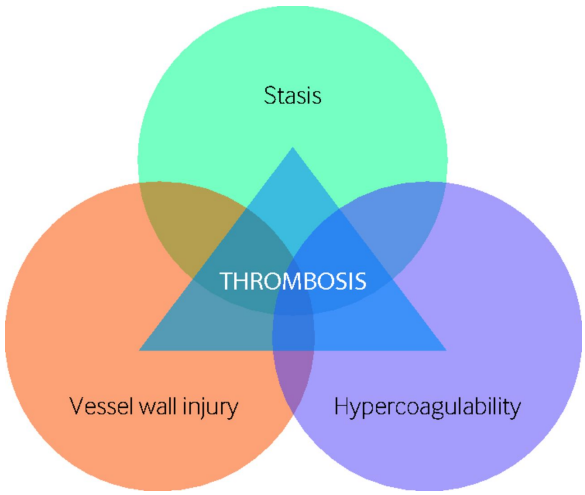

Figure 1.5: virchow's triad. Three factors contribute to thrombosis: stasis, hypercoagulability and vessel wall injury

Blood stasis

When blood flow slows down or becomes stagnant, it creates an environment conducive to thrombosis by allowing clotting factors and platelets to accumulate locally. Blood stasis, particularly venous stasis, can occur in situations such as:

- **Prolonged immobility**: Extended periods of immobility, such as during long

flights or extended bed rest, can significantly reduce blood flow, leading to venous stasis [33].

- **Heart failure**: In patients with heart failure, reduced cardiac output can lead to sluggish venous return, contributing to stasis in the venous system [33].
- **Varicose veins**: Abnormalities in the venous structure, such as varicose veins, can slow down blood flow and lead to stasis in local areas [34].

Endothelial injury (Vessel wall injury)

Endothelial injury refers to damage to the inner lining of blood vessels. Under normal conditions, clotting factors and platelets remain inactive. However, when the endothelial lining is disrupted, it exposes subendothelial tissues, triggering the coagulation cascade and platelet activation. Common causes of endothelial injury include:

- **Trauma or surgery**: Physical injury to blood vessels during trauma or surgical procedures can damage the endothelium, leading to clot formation [35].
- **Inflammation**: Inflammatory processes weaken the endothelial layer, making it more prone to injury. Chronic inflammation is associated with endothelial dysfunction and increased thrombogenicity [36].
- **Atherosclerosis**: Plaques formed in atherosclerosis can rupture, damaging the endothelium and contributing to thrombus formation, particularly in arteries [37].

Hypercoagulability

Hypercoagulability refers to an increased tendency for thrombus formation resulting from genetic or acquired conditions that disrupt the balance between clot formation and dissolution. Key causes of hypercoagulability include:

- **Genetic predispositions**: Inherited conditions, such as factor V Leiden mutation or deficiencies in natural anticoagulants (e.g., protein C, protein S, antithrombin), increase the risk of clot formation by impairing the regulation of thrombin generation [38].

- **Hormonal changes**: Hormonal changes, such as those induced by oral contraceptives or hormone replacement therapy, increase levels of clotting factors. For example, estrogen-containing contraceptives stimulate the production of procoagulant proteins, promoting clot formation [39].
- **Cancer**: Many cancers are associated with hypercoagulability due to the release of procoagulant substances by cancer cells, which activate the coagulation cascade. This phenomenon, often referred to as Trousseau's syndrome, is common in malignancies such as pancreatic and lung cancer [40].

1.5 Thrombin Generation Assay

The Thrombin Generation Assay (TGA) is a laboratory test designed to evaluate the capacity of plasma to generate thrombin, the central enzyme in the coagulation cascade. It addresses a gap left by traditional coagulation tests like prothrombin time (PT) and activated partial thromboplastin time (APTT), which are limited in their ability to capture the dynamic balance between procoagulant and anticoagulant forces. TGA measures thrombin generation through the continuous monitoring of a thrombin-specific fluorogenic substrate [41], providing several critical parameters as shown in Figure 1.6:

- **Lag time (τ_{lag})**: The time between activation and the initiation of thrombin generation.
- **Thrombin peak (IIa_{max})**: The maximum concentration of thrombin formed.
- **Time to peak (τ_{max})**: The time it takes to reach the thrombin peak.
- **Endogenous Thrombin Potential (ETP)**: The total amount of thrombin generated.

TGA has proven useful for understanding coagulation mechanisms in several clinical contexts. It has been instrumental in assessing patients with hemophilia [31], von Willebrand disease [42], venous thromboembolism (VTE) [43], and other diseases, aiding in the therapies. The assay is sensitive to various anticoagulants, including unfractionated heparin, low molecular weight heparin, and direct oral anticoagulants (DOACs), allowing for individualized treatment adjustments [44]. In summary, TGA captures the entire thrombin generation process, provides a deeper understanding of coagulation dynamics and supports the personal treatments for bleeding and thrombotic disorders.

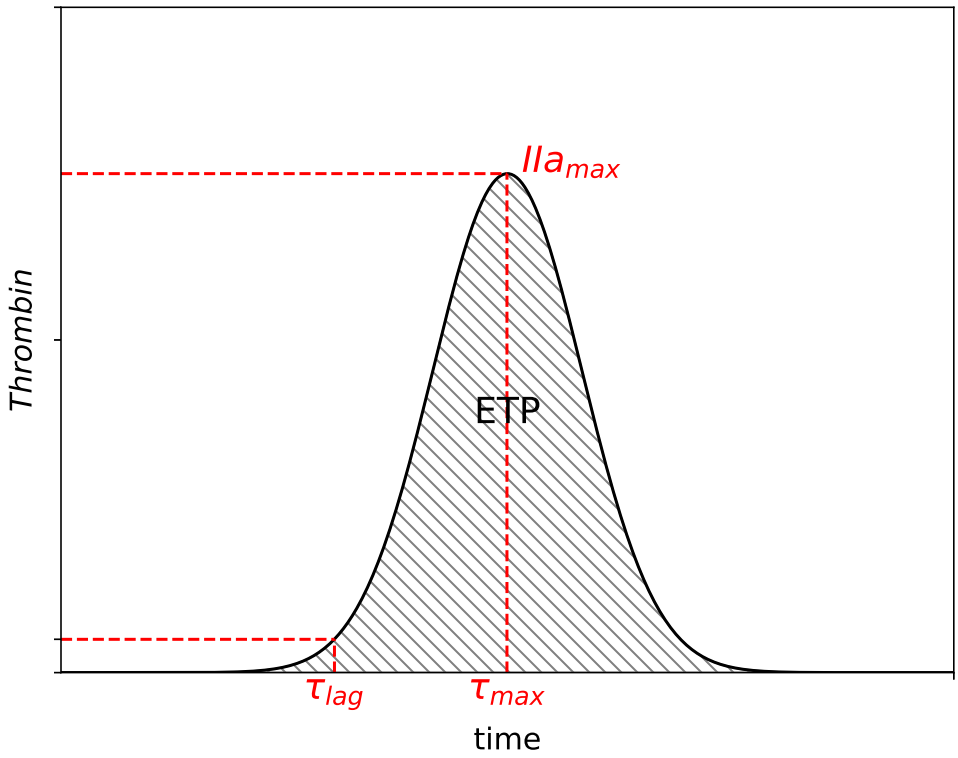

Figure 1.6: Quantities of interests in TGA. IIa_{max} (peak thrombin concentration), τ_{max} (time to peak), τ_{lag} (time to reach 10 nM of thrombin) and ETP (endogenous thrombin potential) for a thrombin formation curve in time. Adapted from [5].

1.6 Mathematical modelling

Mathematical modelling is a fundamental tool in understanding the coagulation process and predicting the outcomes of various physiological and pathological conditions. Models are designed to simulate different spatial scales, from simplest 0D models, which capture reactions in a uniform space, to complex 3D models that account for spatial heterogeneity, blood flow dynamics, and clot growth in the vascular, veins, organs or medical devices, etc. This introduces an overview of various types of models, their optimization, reduction methods, and their applications in published works.

1.6.1 Coagulation models in quiescent plasma

Mathematical models in quiescent plasma are the simplest type of coagulation models, where transport phenomena are neglected, and the system is assumed to be homogeneous. A computational model typically includes activation and self-regulating thrombin feedback reactions. These models assume that the amount of available phospholipidic surfaces is above the threshold required to trigger the cascade [45]. The coagulation cascade can be represented by a set of ODEs:

$$\frac{d\mathbf{X}}{dt} = \mathbf{R} \tag{1.1}$$

where $\mathbf{X}$ contains the concentrations of the n chemical species involved in the cascade and $\mathbf{R}$ is the vector gathering all the associated source terms. The ODE for each species can be figured out according to the law of mass action. A key purpose of these models is to represent the thrombin generation assay computationally. Such plasma-based models are widely used to simulate well-mixed systems, enabling researchers to isolate and analyze the roles of specific clotting factors in the coagulation cascade.

To the best of the author's knowledge, Nesheim et al. [46] developed the first mathematical coagulation model. Khanin and Semenov [47] proposed a model including the positive feedback effect of Va on thrombin generation. However, due to limited biological knowledge at that time, early models were often overly simplified, failing to capture the physical meaning of the coagulation process. For instance, crucial components such as factors VIII and IX (whose deficiencies can cause hemophilia) and inhibitors were ignored in Khanin's model. Hockin et al. [18] later developed a well-known detailed coagulation model, which was subsequently improved by Butenas et al. [15]. Zhu [48] integrated the intrinsic and extrinsic

pathways into a unified model that simulates thrombin generation under various conditions, including the absence of some inhibitors to simulate specific pathological conditions. An ODE-based "Platelet-Plasma" model was developed to predict blood stability under various enzyme perturbations, incorporating platelet activation dynamics through phosphatidylserine exposure [19]. All reaction rates depended on platelet activation are altered by a single function of thrombin concentration. This model bridges coagulation kinetics with platelet function. This model was improved by Anand et al. [49], integrating a neural network-based platelet calcium signaling model issued by Chatterjee et al. [50].

Owen et al. [21] highlighted that no existing ODE-based models accurately predict thrombin generation, with significant discrepancies between them and experiment observations. Even so, these models remain valuable for analyzing the roles of various clotting factors and certain medical applications. Lo et al. [51] introduced a kinetic Monte Carlo simulation and revealed limitations of coagulation models under sub-pM TF levels, where coagulation failed to initiate, emphasizing the challenges of modeling in low TF scenarios. Luan et al. [52] employed a computation model and sensitivity analysis to identify fragile mechanisms within the coagulation cascade, demonstrating that FX/FXa activity and thrombin-mediated platelet activation are particularly vulnerable. The findings align with the clinical efficacy of FX/FXa and direct thrombin inhibitors, supporting the use of computational models for rational anticoagulant target selection despite model uncertainties.

A deterministic computational model of extrinsic pathway and two empirical experimental systems were used to evaluate clinical cases concerning anticoagulants: wafarin, fondaparinux and Rivaroxaban [6] (See Figure 1.7). Bouchinita et al. [53] developed a model describing blood clotting during warfarin treatment. The function of warfarin is introduced by a Pharmacokinetics - Pharmacodynamics (PK-PD) sub-model. Dunster et al. [54] investigated the differences in factors between patients who experienced an early-age myocardial infarction (MI) and healthy controls using both plasma measurements and a mathematical model. The study suggests that models help identify individuals at risk for MI, predict recurrent risk, and guide anticoagulant therapy effectively. Lee et al. [55] established a QSP (quantitative systems pharmacology) model for non-bleeding baseline coagulation activity with data from clinically relevant in vivo biomarkers at baseline and changes in response to recombinant activated factor VII treatment . Menezes et al. [56] introduced a personalized methodology based on 0-D coagulation model for treating acute traumatic coagulopathy (ATC). Validated through in vitro experiments, the model contributed to individualized resuscitation strategies for ATC patients. Similarly, Ghetmiri et al. [57] developed a Goal-Oriented Coagulation Management

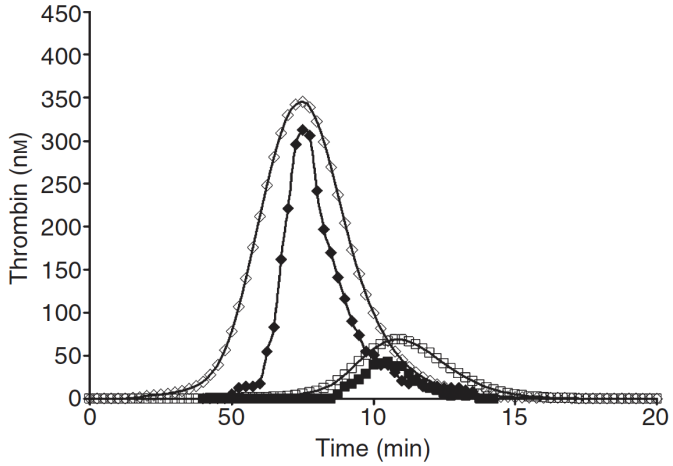

Figure 1.7: Comparison of computational and empirical thrombin generation profiles for an average healthy individual (diamonds) and an average warfarin-treated individual (squares). Open symbols represent computational predictions, while closed symbols represent empirical plasma measurements. 5 pM tissue factor (TF) stimulus was used in all cases. Figure is from [6].

(GCM) algorithm, a personalized approach for calculating coagulation factors. This algorithm integrates patient-specific factors, rapid concentration measurements, and an improved thrombin dynamics model for precise control for personalized treatment.

1.6.2 Coagulation models under blood flow

Blood flow affects the distribution of clotting factors, platelets even blood cells, as well as the mechanical forces on thrombus. Models involving blood flow require more complex representations to account for transport effect such as diffusion and convection. These models are critical for understanding how clots form in specific dynamic environments.

The first 0-D mathematical coagulation model under blood flow was proposed by Kuharsky et al. [58]. The model takes into account plasma-phase and surface-bound enzymes and zymogens, coagulation inhibitors, and activated and inactivated platelets. It includes both plasma-phase and membrane-phase reactions, and accounts for chemical and cellular transport by flow and diffusion, albeit in a simplified manner by assuming the existence of a thin and well-mixed fluid laye near the surface. This model was adapted by Elizondo et al. [59] to present a 0-D mathematical model for venous thrombosis (VT) due to slow flow. Recently, Miyazawa et al. [60, 61] improved this models family to account for the effects of the

half-activated factor V (V-h). An increased FV-h fraction was found to accelerate the thrombin generation process. A detailed explanation of these types of models is in Figure 1.8. These models allow to consider the effect of blood flow on thrombin concentration in addition to chemical reactions and provides a new perspective for the analysis of the effects of clotting factors on thrombin generation. However, like the 0D model in plasma, this model cannot accurately quantify clotting formation in specific applications.

The first one-dimensional (1-D) spatio-temporal mathematical model was developed by Zarnitsina et al. [62, 63]. The study provides insights into clot formation, its spatial spread, and growth from the injury site perpendicular to the vessel wall into the blood flow [62]. Spatial dynamics analysis demonstrated that above-threshold activation generated a high-speed thrombin concentration wave propagating from the activation zone [63].

Two-dimensional (2D) models include both length and width dimensions, providing more details about the spatial distribution of clotting factors, cells, and blood flow within a plane. These models use more complex Partial Differential Equations (PDEs) to represent diffusion, advection, and reactions of clotting factors over an area. Leiderman et al. [64] developed the first spatial–temporal mathematical model of platelet aggregation and coagulation under flow that includes details of coagulation biochemistry, chemical activation and deposition of blood platelets, as well as the two-way interaction between the fluid dynamics and the thrombosis growth. Chen et al. [65] developed a reduced coagulation model, accurately predicting thrombin and fibrin generation. Xu et al [66]. developed a two-dimensional multi-scale model to study thrombus formation in blood vessels. The model integrates macroscale blood flow dynamics with microscale platelet and fibrinogen interactions modeled using an extended stochastic discrete cellular Potts framework. Govindarajan et al. [8] used Leiderman's model to investigate the temporal changes in the spatial distributions of the key enzymatic (i.e., thrombin) and structural (i.e., platelets) components within a growing thrombus. The simulation was validated using experimental data in a "Y" shape flow-chamber (See Figure 1.9). On a more practical level, Dydek et al. [67] used numerical simulations to analyze thrombin formation and location relative to tissue factor (TF) position in disturbed flow induced by an open venous valve. The computational model incorporated hemodynamics, reaction kinetics, and chemical transport of 22 biochemical species. And a fluid-chemical model was developed to study thrombin transport and its role in Intra-Luminal Thrombus (ILT) formation within Abdominal Aortic Aneurysms (AAAs) by Biasetti et al. [68]. This model revealed that coherent vortical structures drive thrombin accumulation in the distal AAA, consistent with

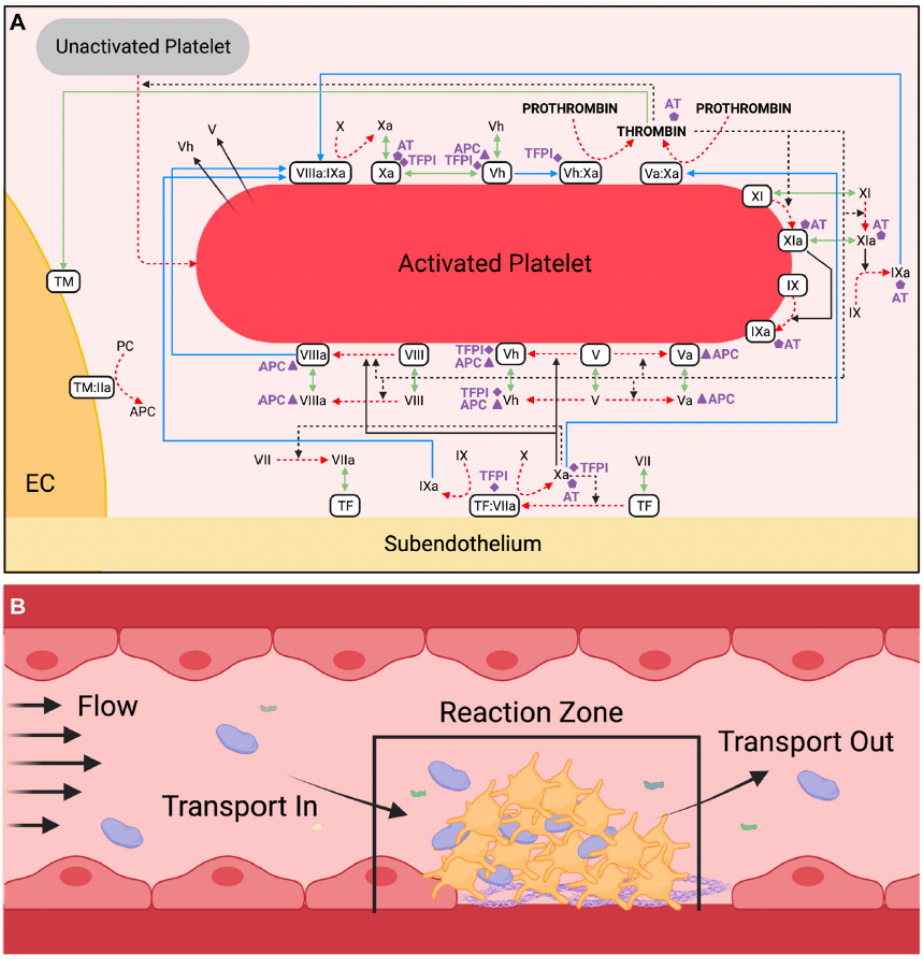

Figure 1.8: Schematic representation of coagulation reactions and the reaction zone included in the model. (A) Coagulation Reactions: Dashed red arrows indicate cellular or chemical activation processes, blue arrows represent chemical transport in the fluid or on surfaces, and green arrows depict binding and unbinding from cell surfaces. Rectangular boxes denote surface-bound species. Solid black lines indicate enzyme action in the forward direction, while dashed black lines show feedback enzyme action. Black lines with a fade indicate release from platelets, while purple shapes denote inhibitors. The lowercase "a" signifies the activated form of a species (e.g., X and Xa refer to clotting X and activated clotting X, respectively). (B) Reaction Zone: A schematic of the vessel, reaction zone, and transport of platelets and proteins as incorporated in the model. Abbreviations: APC, activated protein C; AT, antithrombin; TF, tissue factor; TFPI, tissue factor pathway inhibitor; EC, endothelial cell; Vh, partially activated V; PC, protein C; TM, thrombomodulin. Adapted from [7].

clinical observations of thicker ILTs in this region.

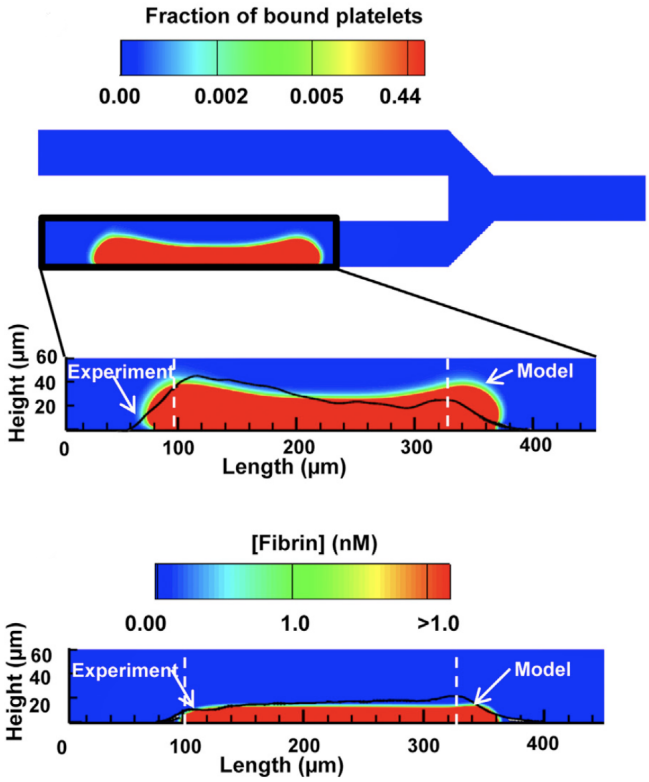

Figure 1.9: Comparison of thrombus growth predictions between computational models and experimental measurements at 430 seconds. Upper Panel: Spatial distribution of deposited platelets, with model predictions shown in color and experimentally measured platelet accumulation represented by the black line. The vertical white dashed lines mark the boundaries of the thrombogenic surface.Lower Panel: Spatial distribution of deposited fibrin, with model predictions in color and experimentally measured fibrin accumulation indicated by the black line. The vertical white dashed lines denote the beginning and end of the thrombogenic surface. Adapted from [8].

Three-dimensional (3D) models provide the most detailed and realistic simulations by capturing the full spatial dynamics of clot formation and growth. These models represent the vasculars, veins, organs or medical devices environments in three dimensions, accounting for the complex geometry, interactions between clotting factors, blood cells and blood flow. Bouchnita et al. [69] proposed a venous thrombus formation model and implemented it in 3D using a novel cell-centered finite-volume solver. The numerical simulations reproduced in vitro experiments of blood coagulation in microfluidic capillaries. Additionally, a simplified one-equation

model of thrombin distribution was derived, enabling analysis of clotting initiation under varying platelet counts, shear rates, and clotting factors. Jimoh-Taiwo [70] proposed a CFD model that considers the biochemical reactions between thrombin and fibrinogen, pulsatile blood flow, and clot growth in a three-dimensional patient-specific common femoral vein to simulate the DVT as well. Rojano et al. [9] performed simulation considering the effects of reactions and transport of clotting factors into a CFD solver in a cannulated left ventricle (See Figure 1.10). Shankar

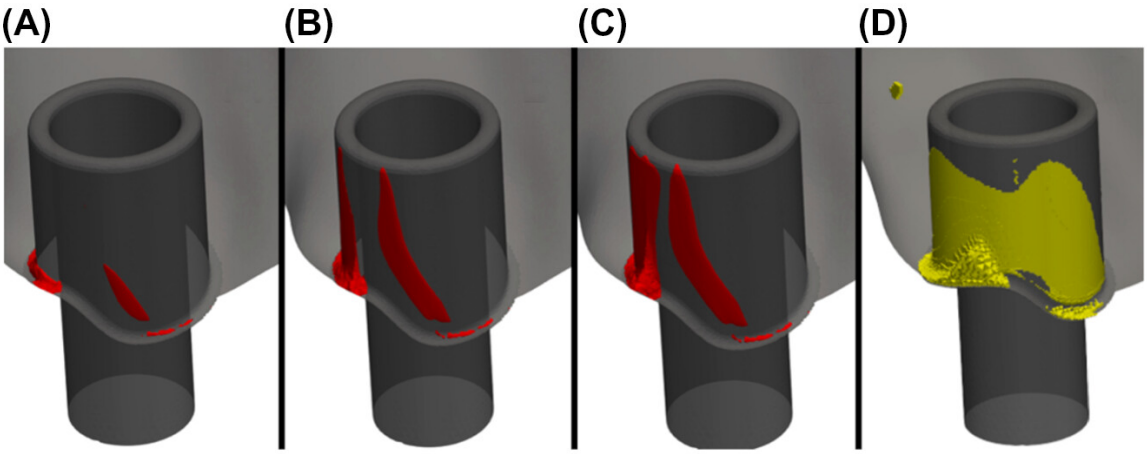

Figure 1.10: Regions of thrombin concentration (more than 1 nmol/m3) around the VAD inlet cannula at 20 seconds (A), 50 seconds (B), and 150 seconds (C). Region in which velocity magnitude less than 0.005 m/s. The figure is adapted from [9].

et al. [71] developed a pioneering 3D multiscale framework for simulating thrombus growth under flow conditions on surfaces presenting collagen and tissue factor (TF). The model integrates a Neural Network (NN) for platelet signaling rather than traditional chemical scheme for facilitating blood flow computation. This framework is the first to incorporate patient-specific platelet phenotypes, enabling robust and clinically relevant 3D simulations of thrombus growth.

An ideal mathematical model of coagulation would encompass all biochemical processes, account for the mechanistic contributions of solid components such as vessel walls and circulating cells, and integrate precise measurements of clotting factor concentrations, reaction kinetics, and the spatial and velocity profiles of all molecules and solids in blood flow. Complex models face two significant drawbacks: high computational cost and substantial uncertainty. These challenges highlight the necessity of adopting strategies like model reduction and parameter optimization to strike a balance between accuracy, computational efficiency, and reliability.

1.6.3 Optimization of coagulation cascade models

On the one hand, no existing model can accurately fit the experimentally obtained thrombin generation [21]. On the other hand, neither the reaction mechanism nor the reaction constants and initial concentrations are precisely known. These quantities are taken as average or normal values in the theoretical model and are estimated by fitting experimental data [44]. Therefore, the optimization of mathematical models is critical for aligning simulated outcomes with experimental or clinical observations.

Optimizations for coagulation cascade involve fine-tuning parameters, such as rate constants or initial concentrations, to achieve the best fit to target data. Rojano et al. [5] optimized an intrinsic pathway model of [19] by adjusting parameters slightly, improving the prediction of thrombin generation under different levels of VIII and the improvement was validated by comparison with experimental data. Rojano et al. [9] developed a simple extrinsic pathway model and using optimization tool to define the initial concentrations in the reduced model. Ratto et al. [72] developed a patient-specific modeling approach for coagulation. The method starts with fine-tuning parameters of a reduced kinetic model to fit experiment data, which is then applied to analyze spatial distributions of blood factors under flow conditions and to assess the outcomes of treatments for coagulation disorders. Sagar et al. [73] developed a optimizer named Dynamic Optimization with Particle Swarms (DOPS), a novel hybrid meta-heuristic that combined multi-swarm particle swarm optimization with dynamically dimensioned search (DDS). The authors compared the performance of DOPS with other commonly used meta-heuristics such as differential evolution (DE), simulated annealing (SA) and dynamically dimensioned search (DDS). DOPS outperformed other common meta-heuristics on the optimization test for a coagulation cascade model.

These optimizations achieved good fits from the aspect of thrombin generation. However, these studies did not explore the highly complex landscape of coagulation models, nor did they analyze the nature of the obtained minima. While their solutions may appear optimal based on small numerical errors, there is no guarantee that they correspond to a true global minimum. Figure 1.11 shows that different patients have different levels of clotting factors and generation of thrombin-antithrombin in coagulation dynamics. Although this figure is based on real statistics, instead of simulation, it indicates the complexity of coagulation dynamics.

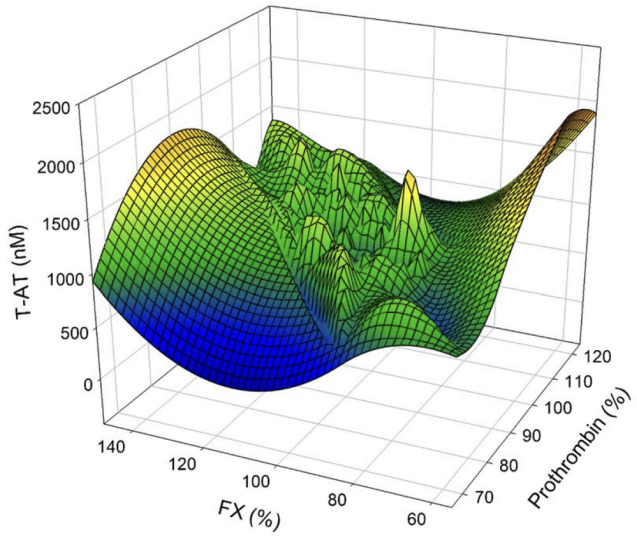

Figure 1.11: Prothrombin and factor X levels on T-AT formation from 122 patients [10].

1.6.4 Model reduction of coagulation cascade

The application of detailed models is often constrained by substantial parameter uncertainties. Additionally, the complexity of such models limits their practical application in scenarios involving complex flow configurations. Reducing the number of parameters to a minimum is crucial, avoiding the incorporation of redundant parameters [74]. The primary aim of this chapter is to simplify coagulation models by reducing equations, or parameters while preserving essential system dynamics.

Rojano et al. [75] developed a novel reduced model comprising only eight chemical reactions by a sensitivity analysis using two techniques to identify the most influential parameters in an existing detailed coagulation model. Following calibration via Bayesian inference, the reduced model demonstrated strong predictive capabilities across various initial conditions. Chen et al. [65] presented a reduced coagulation model based on experimental measurements, incorporating a thin-film assumption for the clot core with zymogen levels equated to those in a flowing plasma. Sagar et al. [76] developed a hybrid modeling approach combining ODEs with logical rules to simulate the coagulation cascade. The model consisted of five differential equations and logical rules resulting in a formulation significantly smaller than traditional mechanistic models. Hansen et al. [77] introduced an automated framework to generate reduced-order models. The framework consists of nested optimizations, where an outer optimization selects the optimal species for the

reduced-order model and an inner optimization selects the optimal rate constants for the new coagulation models. Lacroix [78] presented a reduced model consists of 15 factors interacting within 8 PDEs to simulate the formation and subsequent fibrinolysis of a clot in quiescent plasma. By adjusting the initial concentration of anti-thrombin (ATIII) and degradation constant of fibrin, the model is able to replicate the size of the clot. However, the modification of initial concentration of ATIII and rate constant indicates that the model lose the original physical robustness. Orfao et al. [44] developed a linear model more helpful for mathematical analysis and parameter estimation than a non-linear model. The linearization preserved the global behavior of the system and gave suitable results that precisely reproduce numerical simulation. However, the linear model is not a positive system, limiting its application.

1.7 Main objectives and summary

While mathematical models are powerful tools for analyzing coagulation cascade, significant challenges exist due to high complexity and uncertainties. These challenges highlight the need for advanced optimization techniques to effectively explore complex parameter landscapes. Additionally, model reduction and simplification are valuable tools for simplifying optimization and enhancing applicability.

To be clinically relevant, computational models of thrombosis must be both efficient and patient-specific. Specifically, the models should be reduced to enhance interpretability and applicability. At the same time, parameters must be carefully optimized and tuned to ensure predictive accuracy and being patient-specific. Additionally, reducing the dimensionality of the model is crucial for accelerating computation. In certain cases, it is essential to couple fluid–structure interaction (FSI) with biochemical processes to capture key aspects of thrombus formation. However, 3D FSI simulations are computationally expensive. This motivates the need to reduce the model from three dimensions (3D) to a simpler framework.

Chapter 1 focuses on optimizing coagulation models, highlighting the impact of variable selection and landscape complexity on outcomes. To address the challenge of local minima, a hybrid optimization strategy is introduced, combining gradient-based and evolutionary algorithms to achieve global solutions and accurate thrombin generation predictions under diverse conditions.

In Chapter 2, a multi-stage reduction strategy is presented to reduce coagulation

models while maintaining their dynamic accuracy. Using different physical-based method, the reduction is validated for both extrinsic and intrinsic pathways models, demonstrating robust performance in clinical scenarios such as hemophilia A.

Chapter 3 examines the interplay between blood flow and coagulation dynamics in venous sinus leaflets. Computational simulations reveal effects of stimulus, anticoagulants, hemodynamic characteristics and selection of models on thrombin generation, offering some insights for predict risk of DVT and tailoring anticoagulant therapies.

The final chapter summarizes the findings and discusses the clinical and computational implications future research directions are proposed.

Chapter 2

How well can a coagulation model be fitted?

This chapter forms the basis of a manuscript currently under consideration for publication, titled "On the Impact of Model Complexity on the Optimization of Coagulation Models: A Computational Study Using Gradient-Based and Evolutionary Strategies" authored by Junyi Chen and Franck Nicoud, and submitted to Mathematical Modelling of Natural Phenomena.

Abstract

Accurately optimizing models of coagulation cascade is crucial for developing effective treatments for bleeding disorders and preventing thrombotic diseases. This chapter focuses on the optimization of coagulation models, comparing the results across multiple existing models with different complexity (number of parameters to be optimized, number of chemicals, tendency of the model to show local minima). Namely, the initial concentrations of the chemical species are first perturbed randomly from their reference values and then optimized to recover the original thrombin generation. The findings suggest that the complexity of the coagulation models significantly affects the optimization process, with more complex models presenting additional challenges for optimization because of the presence of a large number of local minima. It is shown that the density of the latter can become so large that the use of a gradient-based optimization method is hopeless as soon as the distance between the initial and optimal positions is greater than 1% in the species concentration space. Finally, by combining gradient-based methods and evolutionary

strategies, the global optimization problem can be successfully solved. This study highlights the important role of model complexity in parameters optimization of coagulation models and provides a way for improving optimization techniques in coagulation modeling.

2.1 Introduction

Over the last decades, significant progress has been made in characterizing the individual components of the hemostatic system, including the coagulation cascade, platelet activation, and fibrinolysis [79]. Characterizing the individual components has multiple potential health benefits. To name but a few, it would contribute to a better control of wound treatment [80], based by promoting the design of efficient hemostatic materials [81]; help understand and reduce the thrombogenicity of any artificial surface, one of the main limitations to the development of blood-contact devices (extracorporeal circulation, artificial valves, ventricular assist devices, etc) [82]; help design patient-specific treatments to limit the occurrence of venous thromboembolism, one of the main causes of death in hospitals [83].

From a computational point of view, many models have been developed to integrate the available knowledge about biochemistry and provide a systems-level understanding of the process [84]. Mathematical models for coagulation can be classified into three categories: homogeneous models, pseudo-homogeneous models and heterogeneous models [85]. Homogeneous models describe the coagulation cascade as a set of ordinary differential equations (ODEs) and all the species are uniformly distributed and well mixed throughout the fluid phase. They have been developed for 40 years and one of the most famous model of this category was issued by Hockin et al. [18]. Pseudo-homogeneous models and non-homogeneous models are both cell-based models, which have been proposed for 20 years but not applied very widely [86]. For example, Chatterjee et al. [19] considered the activation of platelets by introducing a coefficient pre-multiplying the constant rates of those biochemical reactions which mainly occur over the membrane of activated platelets, instead of describing the whole activation process. The initiation of thrombin generation can be achieved either by adding exogenous tissue factor (TF), which corresponds to the extrinsic pathway, or by lowering the levels of corn trypsin inhibitor (CTI), a substance that impedes the generation of XIIa, representing the intrinsic pathway. These pathways eventually merge at the activation point from factor X to Xa. Xa then collaborates with its cofactor Va to constitute the prothrombinase complex, a crucial element in the conversion of prothrombin (II) to thrombin (IIa). Rather

than introducing an ad-hoc pre-multiplying coefficient, the heterogeneous model proposed by Fogelson et al. [20] considers platelets as separate entities which have a finite number of adhesion sites on their surface. Bouchnita et al. [69] derived a methodology to study the interplay between the platelets count, the injury site and the blood flow and its effect on coagulation in a tube under venous conditions.

In the core of coagulation process is thrombin (IIa), a key enzyme interacting with various sub-systems and factors, converting fibrinogen into fibrin and activating platelets. There is no doubt that figuring out the production of thrombin by experimental approaches is very relevant to assess the coagulation profile of individuals. To this respect, Thrombin Generation Assays (TGA) where the time evolution of thrombin in a blood sample at rest is monitored are widely used in the clinical routine and research [22] to assess the coagulation profile of individuals. For example, TGAs play role in the diagnosis and management of bleeding disorders, including hemophilia [87] and von Willebrand disease [42], by helping understand and personalize treatment plans based on hemostatic capability [88]. However, experiments consume a lot of resources. If based on accurate biochemical schemes, the computational approach is more economical and faster, and it gives the opportunity to integrate and quantify reaction details, which can help the design of experiments in turn [17, 89].

Any mathematical model for coagulation involves parameters (rate constants, initial concentrations) which are not perfectly known and may change depending on the patients and their condition. It is therefore useful to develop tools capable of optimizing the parameters on a case-by-case basis so that the coagulation models, once properly tuned, can predict the generation of thrombin or other clotting factors accurately and efficiently. Some modern computation technologies have been used to find the suitable parameters and outputs for biochemistry reactions including coagulation cascade. Machine learning can explore massive design spaces to identify correlations and multi-scale modeling can predict system dynamics to identify causality [90]. Chelle et al. [91] optimized kinetic rates with evolutionary algorithm, but a poor agreement was reached when the whole set of rate constants was treated as the variables to optimize. Rojano et al. [9] used a python package called S-timator using both least square optimization and artificial neural networks to optimize the parameters and make them fit well to some numerical data. Hansen et al. [77] employed evolutionary algorithms in both their outer and inner optimization processes to choose the most effective species and search for the best rate constants. The purpose of their work was to create the method of reduction of the models instead of optimization, so that they did not pay much attention to verify optimization results. Ranc et al. [5] modified certain rate constants

and concentrations based on their expertise and intuition, aiming to enhance the prediction of thrombin generation more effectively than with the original models. [92] optimized the rate constants in the process to establish a reduced model and pay some attention to the landscape, although the size of this reduced model is relatively small. Ratto et al. [72] proposed a patient-specific modelling approach to study blood coagulation, taking into account the complications of the process and the large inter-patient variation of blood factors and physiological conditions. They used conventional thrombin generation tests to determine parameters of a reduced kinetic model, which is then used to study spatial distributions of blood factors and blood coagulation in flow.

It is quite intuitive to think that the surface response of a dynamical system is all the more prone to contain minima as the dimension of the vector of unknowns is large. These minima can be either local or global and should be treated and discussed carefully. In order to find the global minima more efficiently and exactly, some researchers have combined the evolutionary strategies and gradients-based methods to optimize models from various research areas [93, 94]. By combining these two types of methods, these authors leveraged the strengths of each algorithm to efficiently explore the search space and converge to the global minimum. To the best of our knowledge, no one has yet applied hybrid optimization techniques to coagulation mathematical models.

The objective of this chapter is to study to what extent the parameters of a coagulation scheme can be optimized and what is the impact of the number of unknowns on the optimization process and the complexity of models (number of parameters to be optimized, number of chemicals, tendency of the model to show local minima). The numerical framework, the optimization strategies and the coagulation schemes considered are described in Section 2.2. The results are discussed in Section 3.4, where it is shown that a classical gradient-based optimization procedure can be effective for a reduced order scheme (5 species) and a sophisticated scheme with only 4 variables to optimize. After identifying the large number of local minima as the reason for the failure of the optimization for a 10-species scheme, the results of a combined gradient/CMAES approach are discussed to show the potential of this optimization procedure.

2.2 Methods

2.2.1 Details of coagulation models and reference cases

This study presents the optimization of two distinct models for the extrinsic pathway of the coagulation cascade. Both models consist in a set of ordinary differential equations (ODEs) that describes the time evolution of various coagulation factors, along with the rates of enzymatic reactions that govern the dynamics of the system; they were both validated through previous academic researches [15, 9]. Measuring rate constants experimentally can be challenging, costly and time-consuming, even impossible. When dealing with a large number of unknown parameters, finding a unique solution to this problem often becomes unfeasible [95, 96]. Additionally, large models exhibit a widespread sensitivity to parameter (kinetic rate) values, spanning across several orders of magnitude. This characteristic, known as "sloppiness," has been identified as a significant obstacle to accurate parameter estimation [97]. On the other hand, accurately determining the exact initial concentrations is critical, as it provides essential insights into the initial conditions of experiments or chemical reactions, enabling more accurate predictions of their progression and outcomes. It should also be noted that, unlike rate constants which describe biochemical interactions at protein/molecule level, initial concentrations are specific to individuals and may even vary considerably over time depending on the patient's condition (fatigue, dehydration, infection, ...). This makes the development of methodologies able of correctly assessing/adjusting the physical parameters of coagulation models all the more essential where initial concentrations are concerned.

Butenas' extrinsic pathway model

This sophisticated model of the extrinsic pathway with 38 species and 28 reactions was originally proposed by [18] and improved by Butenas et al. [15]. The cascade is initiated by tissue factor (TF) binding to factor VII, forming the extrinsic tenase complex TF=VIIa (representing the joined TF-VII complex). This complex then activates factor X to Xa, which then binds to activated factor V to convert factor II to IIa. During this process, antithrombin III, protein C (PC), and tissue factor pathway inhibitor (TFPI) act as inhibitors (refer to Figure 2.1a; only some key species are shown). The reactions of this scheme are shown in Table 2.1, while the initial concentrations are displayed in Table 2.2.

Table 2.1:: Chemical reactions defining Butenas' extrinsic pathway model [15].

No.	Reaction	k_1	k_{-1}	k_{cat}
1	$TF + VII \longleftrightarrow TF{=}VII$	$3.2 \times 10^6\ M^{-1}s^{-1}$	$3.1 \times 10^{-3}\ s^{-1}$	
2	$TF + VIIa \longleftrightarrow TF{=}IIa$	$2.3 \times 10^7\ M^{-1}s^{-1}$	$3.1 \times 10^{-3}\ s^{-1}$	
3	$TF{=}VIIa + VII \longrightarrow TF{=}VIIa + VIIa$	$4.4 \times 10^5\ M^{-1}s^{-1}$		
4	$Xa + VII \longrightarrow Xa + VIIa$	$1.3 \times 10^7\ M^{-1}s^{-1}$		
5	$IIa + VII \longrightarrow IIa + VIIa$	$2.3 \times 10^4\ M^{-1}s^{-1}$		
6	$TF{=}VIIa + X \longleftrightarrow TF{=}VIIa{=}X \longrightarrow TFVIIa{=}Xa$	$2.5 \times 10^7\ M^{-1}s^{-1}$	$1.05\ s^{-1}$	$6\ s^{-1}$
7	$TF{=}VIIa + Xa \longleftrightarrow TF = VIIa{=}Xa$	$2.2 \times 10^7\ M^{-1}s^{-1}$	$19\ s^{-1}$	
8	$TF{=}VIIa + IX \longleftrightarrow TF{=}VIIa{=}IX \longrightarrow TF{=}VIIa + IXa$	$1 \times 10^7\ M^{-1}s^{-1}$	$2.4\ s^{-1}$	$1.8\ s^{-1}$
9	$II + Xa \longrightarrow IIa + Xa$	$7.5 \times 10^3\ M^{-1}s^{-1}$		
10	$IIa + VIII \longrightarrow IIa + VIIIa$	$2 \times 10^7\ M^{-1}s^{-1}$		
11	$VIIIa + IXa \longleftrightarrow IXa{=}VIIIa$	$1 \times 10^7\ M^{-1}s^{-1}$	5.0×10^{-3}	
12	$IXa{=}VIIIa + X \longleftrightarrow IXa{=}VIIIa{=}X \longrightarrow IXa{=}VIIIa + Xa$	$1 \times 10^8\ M^{-1}s^{-1}$	$1 \times 10^{-3}\ s^{-1}$	$8.2\ s^{-1}$
13	$VIIIa \longleftrightarrow VIIIa_1 + VIIIa_2$	$6.0 \times 10^{-3}\ s^{-1}$	$2.2 \times 10^4\ s^{-1}$	
14	$IXa{=}VIIIa{=}X \longrightarrow IXa + X + VIIIa_1 + VIIIa_2$	$1.0 \times 10^{-3}\ s^{-1}$		
15	$IXa{=}VIIIa \longrightarrow IXa + VIIIa_1 + VIIIa_2$	$1.0 \times 10^{-3}\ s^{-1}$		
16	$IIa + V \longrightarrow IIa + Va$	$2.0 \times 10^7\ M^{-1}s^{-1}$		
17	$Xa + Va \longleftrightarrow Xa{=}Va$	$4.0 \times 10^8\ M^{-1}s^{-1}$	$0.2\ s^{-1}$	
18	$Xa{=}Va + II \longleftrightarrow Xa{=}Va{=}II \longrightarrow Xa{=}Va + mIIa$	$1.0 \times 10^8\ M^{-1}s^{-1}$	$103\ s^{-1}$	$63.5\ s^{-1}$
19	$Xa{=}Va + mIIa \longrightarrow Xa{=}Va + IIa$	$1.5 \times 10^7\ M^{-1}s^{-1}$		
20	$Xa + TFPI \longleftrightarrow Xa{=}TFPI$	$9.0 \times 10^5\ M^{-1}s^{-1}$	$3.6 \times 10^{-4}\ s^{-1}$	
21	$TF{=}VIIa{=}Xa + TFPI \longleftrightarrow TF{=}VIIa{=}Xa{=}TFPI$	$3.2 \times 10^8\ M^{-1}s^{-1}$	$1.1 \times 10^{-4}\ s^{-1}$	
22	$TF{=}VIIa{=}Xa + TFPI \longrightarrow TF{=}VIIa{=}Xa{=}TFPI$	$5 \times 10^7\ M^{-1}s^{-1}$		
23	$Xa + ATIII \longrightarrow Xa{=}ATIII$	$1.5 \times 10^3\ M^{-1}s^{-1}$		
24	$mIIa + ATIII \longrightarrow mIIa{=}ATIIIa$	$7.1 \times 10^3\ M^{-1}s^{-1}$		
25	$IXa + ATIII \longrightarrow IXa{=}ATIII$	$4.9 \times 10^2\ M^{-1}s^{-1}$		
26	$IIa + ATIII \longrightarrow IIa{=}ATIII$	$7.1 \times 10^3\ M^{-1}s^{-1}$		
27	$TF{=}VIIa + ATIII \longrightarrow TF{=}VIIa{=}ATIII$	$2.3 \times 10^2\ M^{-1}s^{-1}$		
28	$IXa + X \longrightarrow IXa + Xa$	$1.4 \times 10^{-7}\ M$	$8 \times 10^{-4}\ s^{-1}$	

Table 2.2:: The concentration of factors of Butenas' model [15]. The other initial concentrations are set to 0.

Factor	VII	VIIa	X	IX	II	VIII	V	TFPI	ATIII	TF
Concentration (nM)	6.67	0.0667	106.67	60.0	933.0	0.4667	13.33	1.667	2267.0	0.001

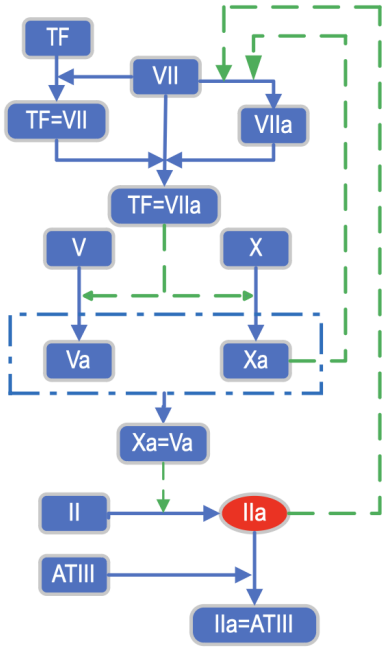

(a) Butenas et al. [15] model of the extrinsic pathway.

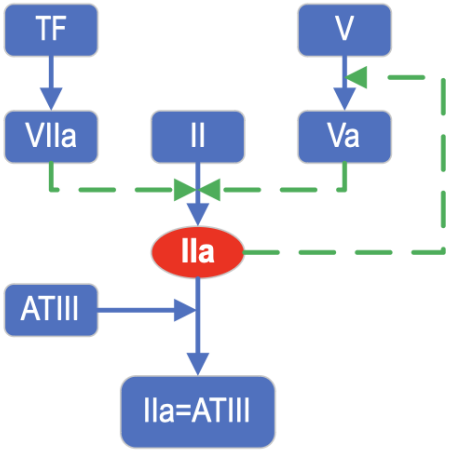

(b) Rojano et al. [9] model of the extrinsic pathway.

Figure 2.1: Comparative display of extrinsic pathway models highlighting key species and reactions. The arrows indicate the direction of the activation or conversion processes. Blue lines show direct transformations, while green dashed lines represent activations influenced by other factors. Non-zero Factors: TF (Tissue Factor), VII, V, X, II (Prothrombin); activated factors: VIIa, TF=VII, TF=VIIa, Va, Xa, IIa (Thrombin); complexes: Xa=Va (Prothrombinase complex), IIa=ATIII (Thrombin-Antithrombin complex). (a) Butenas' model (Full): This model illustrates the complex interactions between various factors, activated factors, and complexes. (b) Rojano's model (Reduced): A reduced model that focuses on the interactions between various factors, activated factors, and complexes.

Rojano's extrinsic pathway model

Rojano et al. [9] proposed a reduced model of the extrinsic pathway, which was used to simulate a Left Ventricular Assist Device (LVAD) in 3D fluid model. This coagulation model consists of five reactions and eight species, as shown in Table 2.3. The cascade is triggered by TF activating factor VII into VIIa, which in turn activates factor II to IIa (thrombin). The model also includes a positive and an inverse feedback. IIa activates factor V to Va, and Va further activates factor II. In addition, IIa combines with ATIII to form IIa=ATIII, which consumes thrombin (refer to Figure 2.1b). The initial concentrations of the species at time t = 0 are shown in Table 2.4.

Table 2.3:: Reactions defining Rojano's extrinsic pathway model [9].

No.	Reaction	$k_m[M]$	$k_{cat}[s^{-1}]$	$k[s^{-1}]$
1	TF $\longrightarrow$ VIIa			2.283×10^{-3}
2	VIIa + II $\longrightarrow$ VIIa + IIa	3.01908×10^{-7}	0.109473	
3	IIa + V $\longrightarrow$ IIa + Va	7.907×10^{-10}	1.17856×10^{-3}	
4	Va + II $\longrightarrow$ Va + IIa	2.029×10^{-7}	11.71	
5	IIa + ATIII $\longrightarrow$ IIa=ATIII	11.701	7243.5×10^{3}	

Table 2.4:: Reference initial concentrations for Rojano's extrinsic pathway model [9]. The other initial concentrations are set to 0.

Factor	TF	V	II	ATIII
Concentration (nM)	50	20	1610.98	3576.03

2.2.2 Definition of the optimization problem

The coagulation cascade can be represented by a set of ODEs:

$$\frac{d\mathbf{X}}{dt} = \mathbf{R} \tag{2.1}$$

where $\mathbf{X}$ contains the concentrations of the n chemical species involved in the cascade and $\mathbf{R}$ is the vector gathering all the associated source terms. In order to compute the source terms $\mathbf{R}$, it is needed to know the rate constants, the initial concentrations of each species and the reaction scheme. Then the ODEs for each

species can be figured out according to the law of mass action, which states that the rate of reaction is proportional to the product of the concentrations of the reactants. For example, for the reaction #26 in [15] scheme in Table 2.1:

$$\text{IIa} + \text{ATIII} \longrightarrow \text{IIa=ATIII} \tag{2.2}$$

translates into:

$$\frac{d[IIa = ATIII]}{dt} = k[IIa][ATIII] \tag{2.3}$$

where k is the rate constant of the reaction.

In this study, enzymatic reactions are simulated using the Michaelis–Menten equation. This approach is particularly suitable when the enzyme concentration is constant and significantly lower than the substrate concentration. The Michaelis–Menten equation is derived under the quasi steady-state assumption and is defined as follows:

$$v = \frac{d[P]}{dt} = \frac{V_{\max}[S]}{K_m + [S]} \tag{2.4}$$

Here, $V_{\max} = k_{\text{cat}}[E]_0$ represents the maximum reaction velocity, with k_{cat} being the catalytic constant and $[E]_0$ the initial enzyme concentration. The Michaelis constant K_m is a value that depends on the constants of the reaction. As an example, consider reaction #2 from Table 2.3, which follows the Michaelis-Menten kinetics:

$$\text{VIIa} + \text{II} \longrightarrow \text{VIIa} + \text{IIa} \tag{2.5}$$

The rate of formation of product IIa in this reaction is described by the following ordinary differential equation (ODE):

$$\frac{d[IIa]}{dt} = \frac{k_{cat}[VIIa]_0[II]}{K_m + [II]} \tag{2.6}$$

This equation captures the essence of the enzymatic reaction dynamics in the models used, where k_{cat} is the rate at which the enzyme catalyses the conversion of the substrate to the product. The source terms corresponding to all the reactions in Tables 2.1 and 2.3 can be computed like exemplified above in Eqs. 2.3 and 2.6. This leads to two sets of differential equations relevant to the schemes described in Tables 2.1 and 2.3, and which can be solved numerically. The dynamics of all species in the coagulation cascade were determined by solving the associated ordinary differential equations (ODEs).

For optimization, a computation was performed firstly using the original values reported in Tables 2.2 and 2.4 as reference, respectively. Next, the initial values were

changed randomly by adding or subtracting a certain amount of each chemicals, which creates a perturbation or disturbance in the system. The objective of the optimization problem is then to recover the reference state by minimizing the distance between the outcomes of the optimized and reference models. Considering the crucial role of thrombin as the final product of this cascade, the cost function was defined in the following manner:

$$f(\mathbf{x}) = \int_0^{t_{\text{final}}} \left[IIa(t;\mathbf{x}^*) - IIa(t;\mathbf{x})\right]^2 dt \tag{2.7}$$

In this formulation, $IIa(t;\mathbf{x}^*)$ denotes the target concentration of thrombin obtained when the reference initial concentration vector $\mathbf{x}$ is as specified in Tables 2.2 and 2.4. Conversely, $IIa(t;\mathbf{x})$ represents the thrombin concentration for any value of $\mathbf{x}$ assessed during the optimization process. The variable t_{final} denotes the end of the time range for the simulation. This expression is classical and informative for calibrating models parameters [96]. For clearer and more efficient comparisons, the following relative error, which is nothing but a scaled version of the cost function, Eq. 2.7, will be used to display the results:

$$\epsilon = \frac{\int_0^{t_{\text{final}}} \left[IIa(t;\mathbf{x}^*) - IIa(t;\mathbf{x})\right]^2 dt}{\int_0^{t_{\text{final}}} \left[IIa(t;\mathbf{x}^*)\right]^2 dt} \tag{2.8}$$

The original loss function is scaled by the L2-norm of IIa over time. The numerator represents the total squared error between the optimized thrombin concentration $IIa(t;\mathbf{x})$ and the reference thrombin concentration $IIa_(t;\mathbf{x}^*)$, integrated over time. This quantifies the deviation of the simulation from the experimental or reference. The denominator, serves as a normalization factor by integrating the squared reference thrombin concentration over time. This normalization ensures that the error measurement is relative to the overall thrombin generation.

If the traditional Euclidean distance in the state space of n dimensions were used to evaluate the distance between two outcomes of any of the two coagulation models, the species with a large concentration would disproportionately influence the results, causing a biased representation of the true distribution of the outcomes. To overcome this issue, the following normalized distance is introduced:

$$\begin{aligned} D &= \sqrt{\sum_{i=0}^{n} \frac{(x_i^* - x_i)^2}{(x_i^*)^2}} \\ &= \sqrt{\sum_{i=0}^{n} \left(1 - x_i'\right)^2} \end{aligned} \tag{2.9}$$

where the summation is performed over the species with non zero initial value (see Tables 2.2 and 2.4). Moreover, x_i^* and x_i are the reference and optimized concentration of the i_{th} chemical species, respectively. $x' = x/x^*$, where x^* stands for the initial value of the reference given in Tables 2.2 and 2.4. Another advantage of this normalization is to reduce the numerical errors due to the large variety of values taken by the different concentrations.

2.2.3 The basic optimization algorithms

This section outlines the optimization methods employed in this study: Truncated Newton Conjugate Gradient (TNC), Covariance Matrix Adaptation Evolution Strategy (CMA-ES), and the Broyden–Fletcher–Goldfarb–Shanno (BFGS). Each method offers distinct advantages suited to specific types of optimization problems. It solves optimization problems:

$$\min_{\mathbf{x}} f(\mathbf{x}) \quad \text{subject to} \quad \mathbf{l} \leq \mathbf{x} \leq \mathbf{u}, \tag{2.10}$$

where $f(\mathbf{x})$ is the objective function, and $\mathbf{l}$ and $\mathbf{u}$ represent the lower and upper bounds of the variables $\mathbf{x}$.

Truncated Newton Method (TNC)

The term "truncated" in TNC refers to the fact that the Newton direction is not computed exactly but is approximated using an iterative method, such as the conjugate gradient (CG) method. The search direction in Newton methods is determined by solving the equation:

$$\nabla^2 f(x_k) p_k = -\nabla f(x_k), \tag{2.11}$$

where $\nabla f(x_k)$ represents the gradient of the objective function at the current iteration x_k, and $\nabla^2 f(x_k)$ is the Hessian matrix, which captures second-order curvature information. The solution p_k to this equation determines the search direction, which is then used to update the solution iteratively:

$$x_{k+1} = x_k + \alpha_k p_k, \tag{2.12}$$

where α_k is the step size determined through a line search.

The Truncated Newton Conjugate Gradient (TNC) method does not require the explicit computation of the Hessian matrix. Instead, it approximates the

Newton direction iteratively using the Conjugate Gradient (CG) method, using only first-order gradient information. This approach significantly reduces computational costs while still capturing second-order curvature effects [98]. TNC was used to detect the local minima in this chapter.

Limited-memory Broyden–Fletcher–Goldfarb–Shanno with Box constraints (L-BFGS-B)

The L-BFGS-B algorithm is particularly suited for optimization problems involving simple bound constraints and large-scale problems where computing and storing a full Hessian matrix is infeasible. A key advantage of L-BFGS-B is the memory efficiency, as it uses a limited number of gradients and updates to approximate the Hessian, making it scalable for high-dimensional problems [99].

Initially, it set the initial point x_0 within the defined bounds. Meanwhile, it initializes the limited-memory approximation of the inverse Hessian, typically as the identity matrix or a suitable diagonal matrix. For each iteration k, the algorithm performs the following steps. Firstly, the gradient $\nabla f(x_k)$ at the current point and search direction are computed.

$$H_k d_k = -\nabla f(x_k), \tag{2.13}$$

where H_k is the limited-memory approximation of the inverse Hessian matrix. H_k is updated using information from the previous iterations. The new point is adjusted to respect the bounds by projecting the search direction:

$$x_{k+1} = \mathrm{Proj}_{\mathrm{bounds}}(x_k + \alpha d_k), \tag{2.14}$$

where α is the step size determined using a line search that satisfies the Wolfe conditions [100]. The limited-memory approximation of the inverse Hessian matrix, H_k, is refined by incorporating the position differences $s_k = x_{k+1} - x_k$ and the gradient differences $y_k = \nabla f(x_{k+1}) - \nabla f(x_k)$, which capture the changes in position and gradient between iterations. The algorithm terminates when the norm of the gradient satisfies:

$$\|\nabla f(x_k)\|_{final} \leq \epsilon, \tag{2.15}$$

where ϵ is a predefined tolerance. As discussed next, L-BFGS-B was used as the outer optimization for the global optimization to reduce the search space. The outer optimization is commonly referred to as the upper-level optimization task in bi-level optimization.

Covariance Matrix Adaptation Evolution Strategy (CMAES)

CMAES is particularly effective for high-dimensional and complex search spaces, where it estimates and updates a covariance matrix to adaptively capture dependencies between variables. By leveraging statistical learning principles, CMA-ES efficiently navigates intricate, non-convex landscapes [101].

The algorithm begins by initializing key parameters, including the population size λ, the number of selected parents μ, recombination weights w_i, and adaptation coefficients for the covariance matrix and step size. The evolution paths for step size and covariance adaptation are initially set to zero, while the covariance matrix $\mathbf{C}^{(0)}$ is initialized as the identity matrix. The step size $\sigma^{(0)}$ and the initial mean vector $\mathbf{m}^{(0)}$ are chosen based on the specific problem being optimized [101].

At each iteration, a new population of candidate solutions is sampled from a multivariate normal distribution centered at the current mean vector:

$$\mathbf{x}_k^{(g+1)} \sim \mathcal{N}\left(\mathbf{m}^{(g)}, \left(\sigma^{(g)}\right)^2 \mathbf{C}^{(g)}\right), \quad k = 1, \ldots, \lambda. \tag{2.16}$$

Once the new population is generated, the best-performing individuals are selected based on the objective function values, and their weighted average is used to update the mean vector:

$$\mathbf{m}^{(g+1)} = \sum_{i=1}^{\mu} w_i \mathbf{x}_{i:\lambda}^{(g+1)}, \quad \sum_{i=1}^{\mu} w_i = 1, \quad w_i > 0. \tag{2.17}$$

This recombination step ensures that the search distribution is gradually shifted toward promising regions in the search space. To control the step size, the algorithm adapts the step length based on the evolution path, which accumulates information over multiple iterations. The step size update mechanism enables CMA-ES to balance exploration and exploitation dynamically, preventing premature convergence while ensuring efficient progress toward the optimum. A key strength of CMA-ES is its ability to adapt the covariance matrix, allowing it to capture correlations between variables.

The algorithm proceeds iteratively until a predefined stopping criterion is met, such as reaching a maximum number of iterations or satisfying a convergence threshold. The adaptive nature of CMA-ES makes it particularly well-suited for problems where gradient-based methods struggle, such as rugged, multi-modal, or highly non-convex landscapes. As discussed next, , CMA-ES was used as the inner optimization of hybrid optimizer to find the global minimum. The inner optimization is commonly referred to as the lower-level optimization task.

Calculation of the gradients

The adjoint method was used for calculating the gradients of the error function Eq. 2.8 with respect to the initial conditions. The advantage of adjoint method is twofold: first, it is more accurate than finite differences (FD) because the adjoint allows computing the gradients locally, without introducing a finite amplitude variation of the input; second, the associated computational cost increases with the number of outcomes and not with the number of input parameters, as in the case of FD. In the case of coagulation schemes, where the number of outcomes is generally small (only one in the present study, the error defined in Eq. 8) and the number of inputs much larger (up to 10 in the present case), this makes the adjoint-based gradient method more computationally efficient [102]. A comprehensive mathematical derivation and analysis of the adjoint-based gradient computation for coagulation models has been presented recently in [103].

Combination of evolutionary algorithm and gradient-based optimization

The complexity of the coagulation model makes it challenging to find the exact global minimum using either gradient-based or evolutionary algorithm strategy alone. To address this issue, a hybrid optimization that combines these two methods was used to optimize the model and locate the global minimum.

Figure 2.2 shows the schematic of the hybrid optimizer. The optimization process consists of two loops: outer and inner. In the outer optimization, 100 L-BFGS-B optimizations are performed. In both outer and inner optimizations, the variables are normalized concentrations x' mentioned above, thus their optimal value is 1. Then, the average value of each variable (initial concentration of each non-zero clotting factor) is computed. The average value is calculated from the results of 100 optimizations in outer optimizer using the L-BFGS-B algorithm. If the average value of a variable is close to unity (i.e., within the range of 0.999 to 1.001), this variable is fixed at its averaged value for the next stage (inner optimizer). In addition, because the concentrations of each species are not infinite, it is beneficial that concentrations of each species subject to bounds between 0 and 2. While parameters are normalized around 1, the algorithm is constrained to adjust these within the specified bounds of 0 and 2 during the optimization. The bounds for the variables (initial concentrations of non-zero clotting factors) are updated based on the results of the outer stage and set as strict min/max bounds. In the inner stage, only one CMA-ES optimization is performed for searching the global minimum using the new set of variables and bounds.

In this new algorithm, L-BFGS-B method is used to fix some influential variables that always keep the same values and narrow the bounds of the others. This step reduces the overall dimensionality and enables the CMA-ES based inner optimizer to more efficiently and accurately search for the global minimum. Notably, in the outer optimization stage, the optimizer never satisfies the convergence criteria in terms of distance to the reference, highlighting the necessity of employing the hybrid optimization strategy.

Implementation in computer language

The stiff BDF integration method provided by the Python3 package scipy.integrate.solve_ivp was used to obtain the dynamics of concentrations of species by solving the sets of ODEs (Eqs. 2.3 and 2.6). A tolerance value of 10^{-10} was set for the integration process, which proves sufficient to avoid measurable numerical errors for the problems considered.

All gradients-based computation experiments use Python version 3.8.5 and SciPy version 1.13.0. The optimization routines discussed were implemented using SciPy's optimize.minimize function. For example, the application of the L-FBGS-B method was executed with a convergence tolerance of 1×10^{-10} on the function value. The method-specific parameters are detailed in Table 2.5. CMA-ES simulations were performed using python 3.8.5 and cma package, of which parameters are displayed in Table 2.5 as well.

Table 2.5:: Comparison of parameters for optimization methods: TNC, L-BFGS-B, and CMA-ES

Parameter	TNC	L-BFGS-B	CMA-ES
`maxiter`	Not applicable.	10000.	Not applicable.
`tol`	1×10^{-10}	1×10^{-10}	Not applicable.
`fmin`	1×10^{-10}	1×10^{-10}	1×10^{-10}
`popsize`	Not applicable.	Not applicable.	50
`sigma`	Not applicable.	Not applicable.	one-sixth of the length of each variable's variation
`maxfun`	10000	10000	Not applicable.
`eta`	0.25	Not applicable.	Not applicable.
`stepmx`	5	Not applicable.	Not applicable.

For optimization method, details are shown in Section 2.2.3. For the gradient-

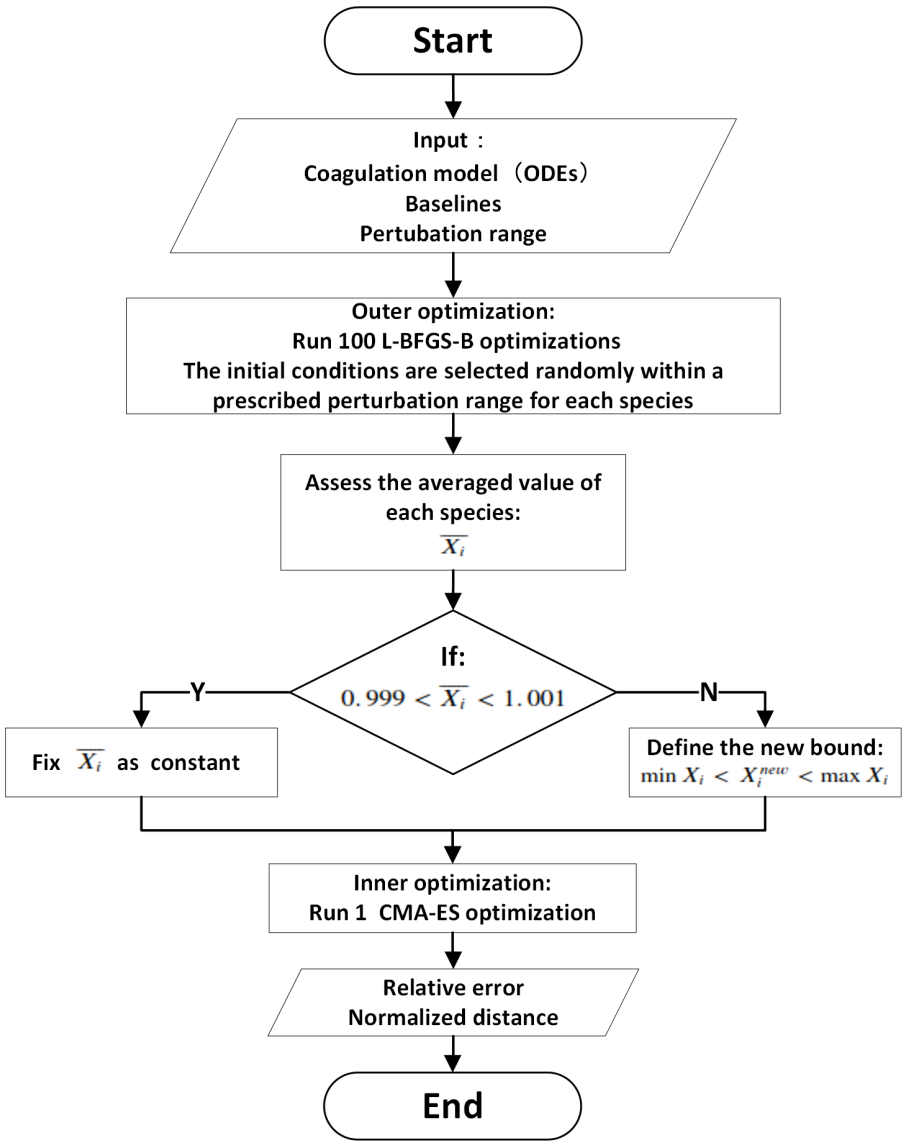

Figure 2.2: Workflow of hybrid global optimizer. The workflow initiates with inputting the model, references, and perturbation range. In the outer optimization, 100 L-BFGS-B runs with randomly perturbed initial conditions determine parameter stability. Parameters within 0.1% of reference are fixed; others proceed to inner optimization via a single CMA-ES run for refinement. The final evaluation includes relative error and normalized distance to the global minimum.

based methods (refer to Table 2.5), the tolerances for gradients and loss function were set to 10^{-6} and 10^{-10}, respectively. In addition, the maximum step of the line search was set to 5, and the severity of the line search was set to 0.25 for TNC. For CMA-ES, the population size was 50 at first and the initial normalized sigma (initial standard deviation in each coordinate) was set to one sixth of the length of normalized bounds. The increase population size was set to 0.5.

2.3 Numerical testing and validation of optimizer

This study optimized two models under different conditions. In order to clearly state the conditions and results, the different conditions are presented in Table 2.6.

2.3.1 TNC-based optimization of Rojano's model

The reduced extrinsic pathway model of Rojano et al. [9] involves five species and eight kinetic parameters, out of which we considered four non-zero initial concentrations of species as variables for optimization. The optimization condition is M_8_5_04 in Table 2.6. The initial variables were randomly varied by up to 20% of the reference. 100 random tests were conducted with varying initial guesses and considering gradient-based optimization (20 perturbed by 1%, 20 perturbed by 5%, 20 perturbed by 10%, 20 perturbed by 15%, 20 perturbed by 20%). Table 2.7 shows the scaled loss function and solutions (normalized initial concentrations). The results show very small distances and relative errors, representative of a numerical global minimum (see Figure 2.3a). Figure 2.4 shows the details of optimization cases when the initial guess is within 20% of the reference. For the reduced model (M_8_5_04), Figure 2.4a displays the time evolution of thrombin before and after optimization and shows that the latter closely aligns with the target and with a relative error close to machine precision $\times 10^{-15}$ (see Figure 2.4b). In this context, different colors in the figure are used to represent distinct perturbations ranges for initial guesses from the reference values for each species.

2.3.2 TNC-based optimization of the Butenas' model

The model of Butenas et al. [15] has 34 species and 45 kinetic parameters. Like for Rojano's model aforementioned, the initial guess of the species concentration was randomly selected in the range from 80% to 120% of the reference values depicted in

Table 2.6:: Summary of different optimization conditions considered. The identifier for each optimization condition is constructed as follows: the first and second integer values denote the number of species and reactions, respectively; the final integer specifies the number of initial concentrations set as variables during the optimization process. If a letter (e.g., _04a, _04b) is appended, it indicates different variable selection configurations under the same model and number of variables.

Identifier	**Coagulation Model**	**No. species**	**No. reactions**	**Variables**	**Description**
M_8_5_04	Rojano's model	8	5	ATIII, II, TF, V	All 4 non-zero initial concentrations were set as variables.
M_38_28_04a	Butenas' model	38	28	ATIII, II, TF, TFPI	4 out of 10 non-zero initial concentrations were set as variables.
M_38_28_04b	Butenas' model	38	28	V, IX, TF, TFPI	4 out of 10 non-zero initial concentrations were set as variables.
M_38_28_10	Butenas' model	38	28	ATIII, II, IX, TF, TFPI, V, VII, VIII, VIIa, X	All 10 non-zero initial concentrations were set as variables.

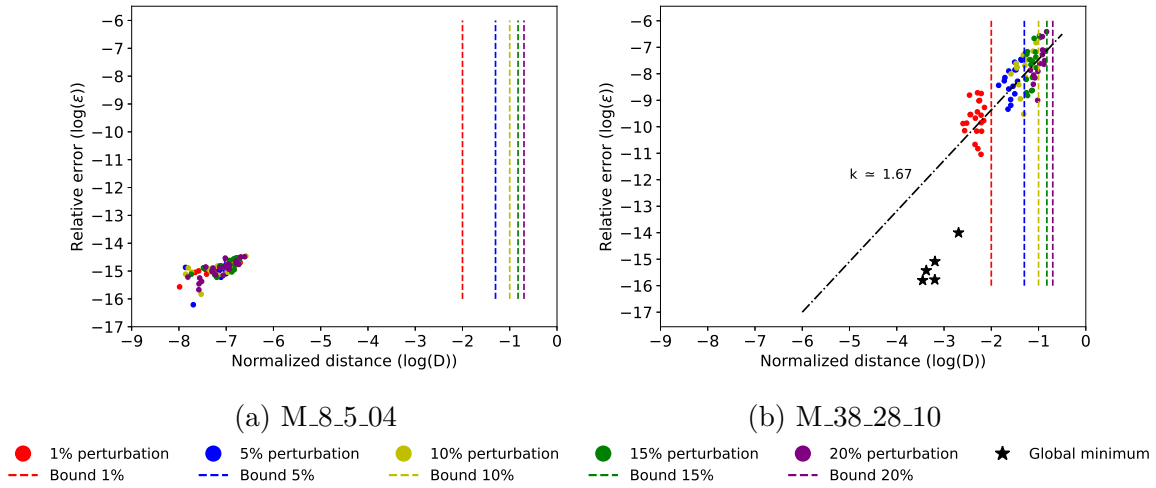

(a) M_8_5_04 (b) M_38_28_10

Figure 2.3: This figure illustrates the relationship between the relative error ϵ (Eq. 2.8) and the normalized distance for the optimization process of Rojano's and Butenas' models using the TNC algorithm under conditions M_8_5_04 and M_38_28_10 in Table 2.6. The plot shows how the initial guess deviations affect the optimization results. Each dot's color represents a specific percentage of random perturbation in the initial guess. The black stars mark the global minimum points. The vertical dashed lines indicate the theoretical maximum distances for each perturbation amplitude. The black dash-dot line shows the trend of error change with distance, characterized by a slope of approximately 1.67.

Table 2.7:: Results of the optimization of Rojano's model using TNC (The initial values are obtained by perturbing the reference values by up to 20%).

	ATIII	II	TF	V	Relative error	
Min	99.9%	99.9%	99.9%	99.9%	6.170 10^{-17}	×
Max	100.0%	100.0%	100.0%	100.0%	3.447 10^{-15}	×

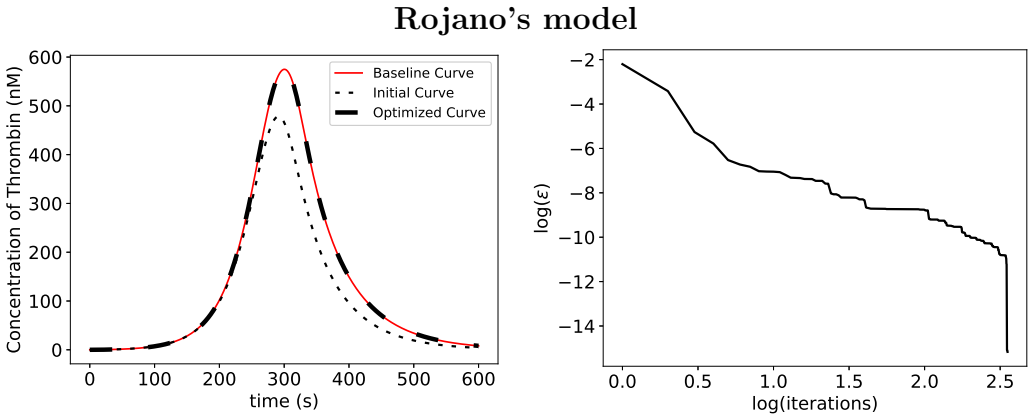

(a) Time evolution of thrombin for the reference, initial guess and optimized concentrations of the species depicted in Table 2.4 using TNC

(b) Convergence curve

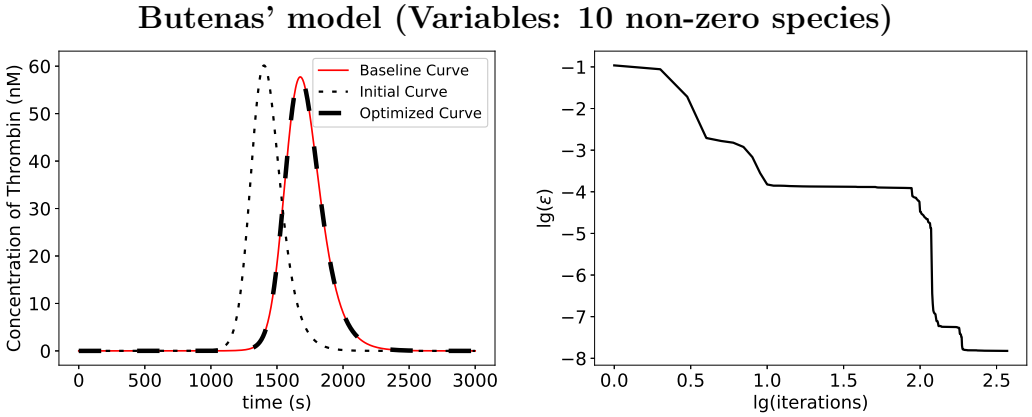

(c) Time evolution of thrombin for the reference, initial guess and optimized concentrations of the species depicted in Table 2.2 using TNC.

(d) Convergence curve

Figure 2.4: Optimization outcomes for Rojano's (M_8_5_04) and Butenas' (M_38_28_10) models using TNC. The amplitudes of perturbation for the initial concentrations are 20%. (a): Time evolution of thrombin for the reference, initial guess, and optimized concentrations in Rojano's model. (b): Convergence curve for Rojano's model, showing the optimization trajectory. (c): Time evolution of thrombin for the reference, initial guesses, and optimized outcomes for Butenas' model with 10 non-zero species. (d): Convergence curve for Butenas' model, demonstrating the iterative optimization progress.

Table 2.2. The Butenas' model with all 10 variables under condition of M_38_28_10 required multiple iterations for optimization. For clarity on the convergence process of one such case refer to Figure 2.4d. The relative error initially stood at approximately 1×10^{-1} and ultimately reduced to around 1×10^{-8}, as depicted in Figure 2.4d. Figure 2.3b presents the outcomes of 100 random tests derived from a range of initial guesses, with each color corresponding to a specific deviation from the reference. The 'Red' dashed line in the figure illustrates the distance between the reference and a set of concentrations corresponding to exactly 1% perturbation. Furthermore, the red dots represent the optimized results obtained from initial guesses where all species are within a +/-1% perturbation range of their respective reference values. In other words, these red dots are the outcomes when each species starts from a value that is no more than 1% higher or lower than its reference. In the same ways, different series of dot correspond to initial perturbations bounded by 5%, 10%, 15% and 20% (see the legend in Figure 2.3 for the color code). In the reduced model $M\_8\_5\_04$, the relative error consistently remains minimal, aligning with the observations in Figure 2.4a. In the Butenas' model scenario $M\_38\_28\_10$, with all variables within 20% perturbation, although the relative error remains consistently low (10^{-8}; see Figure 2.5b), there is a notable deviation in the normalized distance as high as 15%. This deviation suggests potential challenges in accurately retrieving reference values through the optimization process.

2.3.3 Indication of complexity of Butenas' model

It is fair to assume that the difficulty in retrieving the reference conditions through the optimization process, as well as the large dispersion of the results (see Figure 2.3b), is due to the presence of local minima. To further analyse the model response, the distance between the optimized solution and the reference is plotted against the initial-reference distance in Figure 2.5. For the reduced order scheme (under M_8_5_04 condition), the optimized solution is always very close to the reference point: no matter what the initial condition is, the final result almost reaches the reference (see to Figure 2.5a).

In order to get more insights of complexity, it is necessary to explore the optimization of Butenas' model with 10 dimensions deeper. In this case (under M_38_28_10 condition), the dispersion of results is significant for initial perturbations greater than 2% (see Figure 2.5b). Nevertheless, a general trend towards an increase of the optimized-to-reference distance is clearly apparent when the initial-to-reference distance increases. The distance to the reference point can increase or decrease during the optimization process with the same probability in Figure 2.5b. Figure 2.3b

reveals that there is a trend for the error ϵ to increase with the optimized-to-reference distance, as the black dash-dot line reflects with a slope around 1.67; thus the surface response contains a lot of local minima, but the quality (in terms of error value) of these minima improves when they are closer to the global minimum.

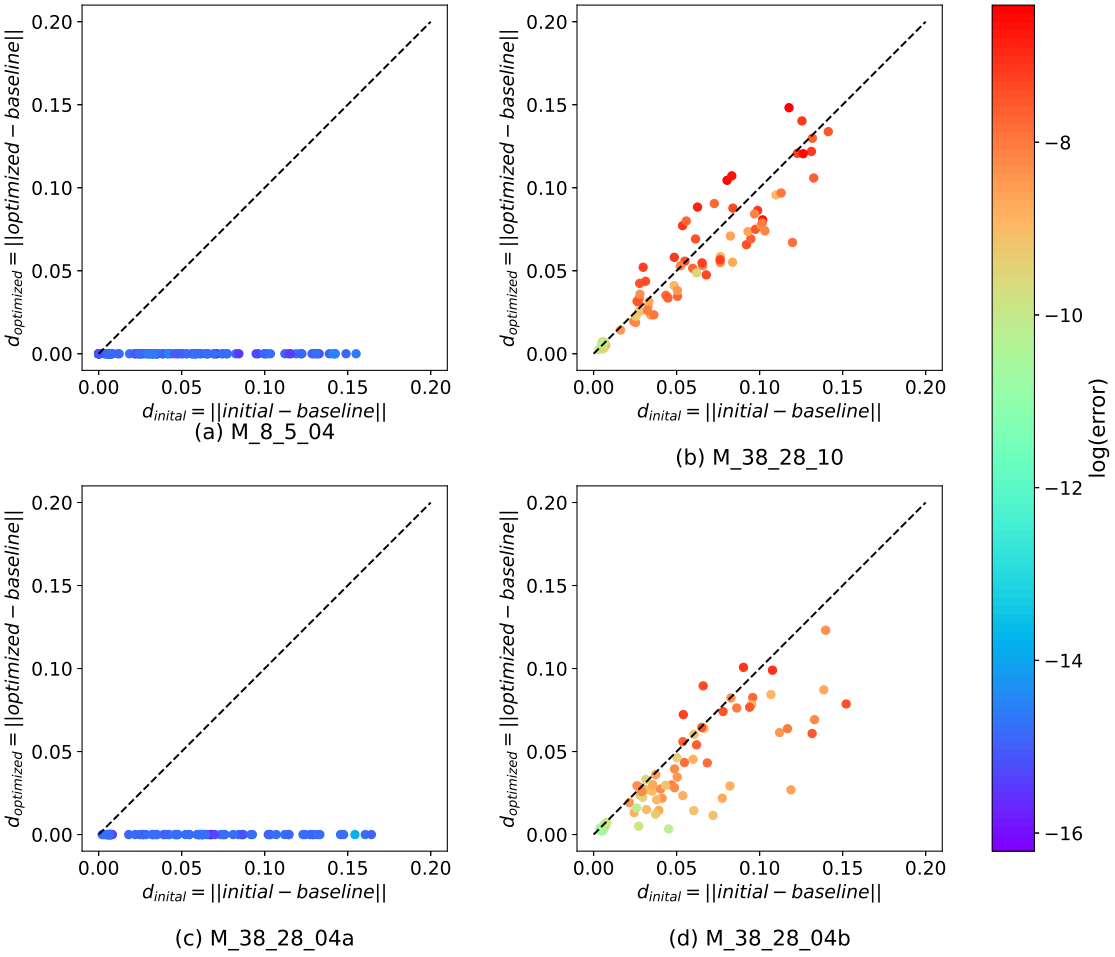

Figure 2.5: Comparative analysis of distances between initial parameter guesses and reference values versus distances between optimized minimum parameters and reference. This figure illustrates how variations in initial guesses impact the optimization trajectory and final model accuracy in predicting thrombin generation. Different sub-figures correspond to different conditions in Table 2.6.

Optimization with +/-1% perturbation of initial guesses

To further characterize the surface response of the M_38_28_10 case, a new condition is considered where the reference concentrations perturbed by a small amount

(+/-1%) are used as initial conditions. Contrary to Sections 2.3.1 and 2.3.2 where the initial perturbations were randomly selected within the +/- 1% range, the perturbation values for each species are exactly equal to +/-1% (See Table 2.8). A key aspect of this setup is the randomization of the +/- signs for each species. This means that while the magnitude of deviation from the reference is consistent across species, the direction of the change (increase or decrease) varies. The results obtained from 5 different choices of the sign of the perturbations are shown in Table 2.8, which shows that the optimization process leads to different solutions, even if the initial perturbation is only 1 % in amplitude. In some cases and for certain species, the converged solution is even further from the reference value than the initial guess (see the bold entries in Table 2.8). This behavior has been already evident in Figure 2.5b, where several dots lie above the dashed line, indicating that the normalized distance became larger after optimization.

To further investigate if the results displayed in Table 2.8 do correspond to local minima, the Hessian matrix was calculated and its eigenvalues examined. The eigenvalue analysis of the Hessian matrix is a fundamental step to ensure that minimum points were correctly identified and avoid saddle points which are characterized by negative eigenvalues. All of the eigenvalues are positive as shown in Table 2.9, indicating that the optimization results correspond to minima. It is worth noting that the variables were normalized before calculating the eigenvalues to ensure accuracy and consistency. Figure 2.6, which corresponds to Case 1 in Tables 2.8 and 2.9, shows that the optimizer reached the minimum for all the species. Table 2.8 demonstrates that the outcomes are influenced not only by the distance of the initial guesses from the reference but also significantly by the direction of change for each species.

Optimization in 4 dimensional sub-spaces

In the initial approach using all 10 variables (condition M_38_28_10), multiple local minima were encountered, making it challenging to pinpoint the global minimum (refer to Figure 2.3). By considering a sub-optimization problem with only 4 variables, the aim is to reduce dimensionality. This might help in simplifying the landscape of the problem, allowing for a clearer understanding of its inherent complexities and a more direct route to the global minimum. Firstly, only the four most sensitive species were chosen as the variables, namely ATIII, factor II, TF and TFPI (condition M_38_28_04a). The sensitivity of the variables was assessed by calculating the absolute value of the gradients of error scaled by each reference

Table 2.8:: Perturbation tests of $+/-1\%$ from reference using TNC. The initial values are obtained by perturbing the reference values by + 1%; the only difference between the different cases is the sign in front of each perturbation. The entries contain the scaled concentrations before and after optimization.

	Case 1		Case 2		Case 3		Case 4		Case 5	
	Initial guess	Results	Initial guess	Result	Initial guess	Result	Initial guess	Result	Initial guess	Result
ATIII	99.0%	99.9%	99.0%	100.1%	101.0%	100.0%	101.0%	99.9%	99.0%	100.0%
II	99.0%	99.9%	99.0%	100.1%	101.0%	100.1%	99.0%	99.9%	101.0%	100.1%
IX	99.0%	100.3%	99.0%	99.0%	101.0%	100.7%	101.0%	**101.5**%	99.0%	99.5%
TF	99.0%	99.4%	99.0%	98.8%	101.0%	100.8%	99.0%	99.5%	99.0%	100.0%
TFPI	99.0%	**98.8**%	99.0%	99.2%	101.0%	100.7%	101.0%	100.5%	101.0%	100.1%
V	99.0%	99.4%	101.0%	**101.4**%	99.0%	99.4%	99.0%	99.0%	99.0%	**98.9**%
VII	99.0%	99.3%	101.0%	**101.1**%	99.0%	**98.6**%	99.0%	99.0%	101.0%	100.6%
VIII	99.0%	100.0%	101.0%	101.0%	99.0%	98.6%	99.0%	99.4%	99.0%	99.7%
VIIa	99.0%	**98.6**%	101.0%	100.9%	99.0%	99.4%	101.0%	**101.1**%	101.0%	**101.4**%
X	99.0%	**101.7**%	101.0%	**97.9**%	99.0%	99.5%	101.0%	**101.2**%	101.0%	**98.8**%
Relative Error	3.598×10^{-4}	8.546×10^{-10}	1.807×10^{-3}	1.838×10^{-10}	1.906×10^{-3}	1.838×10^{-10}	1.906×10^{-3}	1.569×10^{-11}	9.618×1.023^{-2}	9.618×10^{-10}

Table 2.9:: Eigenvalues of the Hessian computed at the optimal point. The Hessian matrix was calculated after normalization.

EV index	Case 1	Case 2	Case 3	Case 4	Case 5
1	1.77×10^{10}	1.77×10^{10}	1.75×10^{10}	1.77×10^{10}	1.76×10^{10}
2	7.90×10^{8}	7.91×10^{8}	7.89×10^{8}	7.89×10^{8}	7.88×10^{8}
3	1.68×10^{7}	1.70×10^{7}	1.70×10^{7}	1.67×10^{7}	1.70×10^{7}
4	3.35×10^{5}	3.16×10^{5}	3.16×10^{5}	3.17×10^{5}	3.16×10^{5}
5	1.11×10^{5}	1.24×10^{4}	1.17×10^{4}	1.19×10^{4}	1.18×10^{4}
6	3.72×10^{4}	4.37×10^{3}	4.20×10^{3}	4.15×10^{3}	4.12×10^{3}
7	9.44×10^{2}	2.35×10^{3}	2.43×10^{3}	2.40×10^{3}	2.38×10^{3}
8	1.81×10^{4}	1.69×10^{2}	1.30×10^{2}	1.35×10^{2}	1.31×10^{2}
9	9.97×10^{3}	1.02×10^{3}	9.94×10^{2}	1.02×10^{3}	1.00×10^{3}
10	8.82×10^{3}	8.34×10^{2}	8.34×10^{2}	7.88×10^{2}	7.28×10^{2}

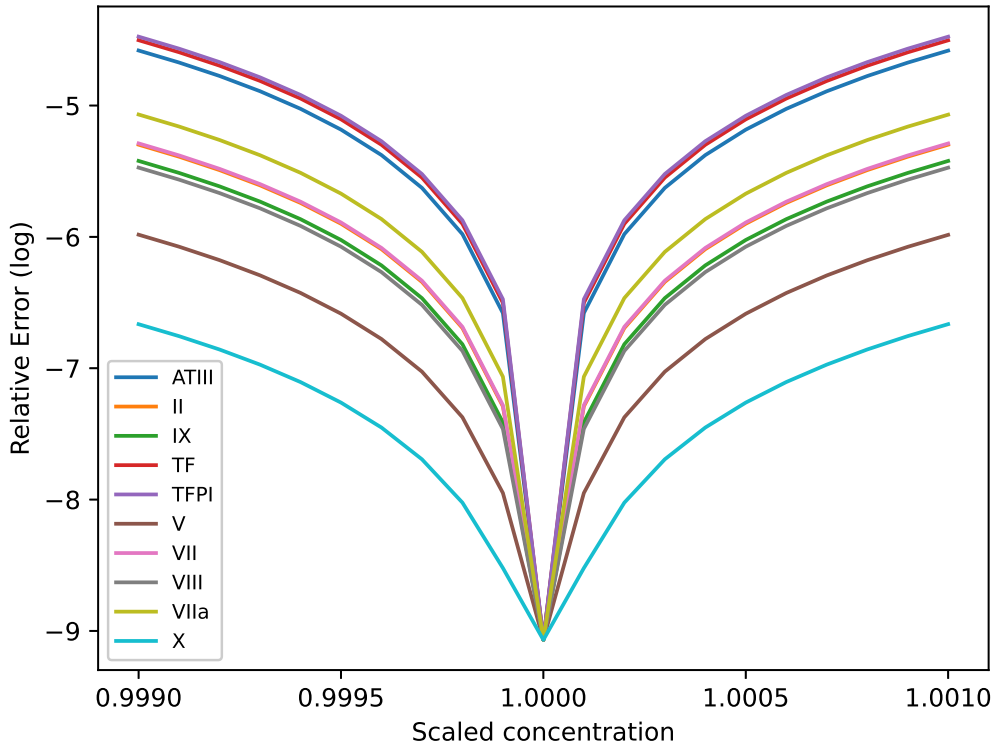

Figure 2.6: Trends of species near local minima. The abscissa is the concentration scaled by its corresponding value after optimization; the ordinate is the error when only one species is deviated from the optimal value.

concentration. The analysis ranks the species based on their influence, where higher gradients indicate greater sensitivity. The sensitivity analysis of the species yielded the following ranking based on their impact on ϵ of Eq. 2.8: ATIII, II, TF, TFPI, IX, V, VII, VIII, and X. Table 2.10 shows that the variables almost converge to the reference values in all the cases and the relative error after optimization is very small, in any case less than 1.7×10^{-14}, very close to machine precision. On the other hand, Table 2.10 demonstrates that when a different set of four variables (specifically IX, V, TF, and TFPI, condition M_38_28_04b) is optimized, there is a noticeable dispersion in both the concentrations and the loss function values. In Figs. 2.7a and 2.7b, distinct behaviors and results of loss function and distance are depicted for the two cases where only 4 variables were considered. The primary difference between these two cases is the presentation of local minimum. The second 4-variable case exhibits a lot of local minima, while the first 4-variable case demonstrates only one global minimum. In Figure 2.7b, it is shown that the optimizer finally got different points and the relative error of loss function reaches about 1×10^{-12} and the distribution is wide. If the normalized distance is less than 1%, the relative error is less than 1×10^{-9}. Generally, Figure 2.7 suggests that the difficulty in optimizing is related to the species (number and type) rather than the kinetic scheme itself.

Figs. 2.5c and 2.5d indicates similar phenomenon as well. In Butenas' model involving the optimization of condition M_38_28_04a, it was consistently observed that the optimized solutions closely align with the reference point. This holds true across various initial conditions, as the final outcomes invariably converge near the reference, as illustrated in Figure 2.5c. In contrast, when optimizing either M_38_28_04b (as detailed in Table 2.2), the results exhibit notable dispersion. Despite this variability, there is a discernible pattern where the distance from the optimized solution to the reference tends to increase in proportion to the initial-to-reference distance. Notably, in 4 out of 100 instances, the distance post-optimization is even larger when only M_38_28_04b are optimized, as shown in Figure 2.5d. Figs. 2.5c and 2.5d also suggest a correlation between the error ϵ and the optimized-to-reference distance. This indicates that the response surface is characterized by numerous local minima of decreasing quality when located further from the global minimum.

By comparing the two scenarios, it becomes evident that different variables will present different complexity, although in the same size dimensions. However, the quality of these minima, as measured by the error value, tends to improve as they approach closer to the global minimum.

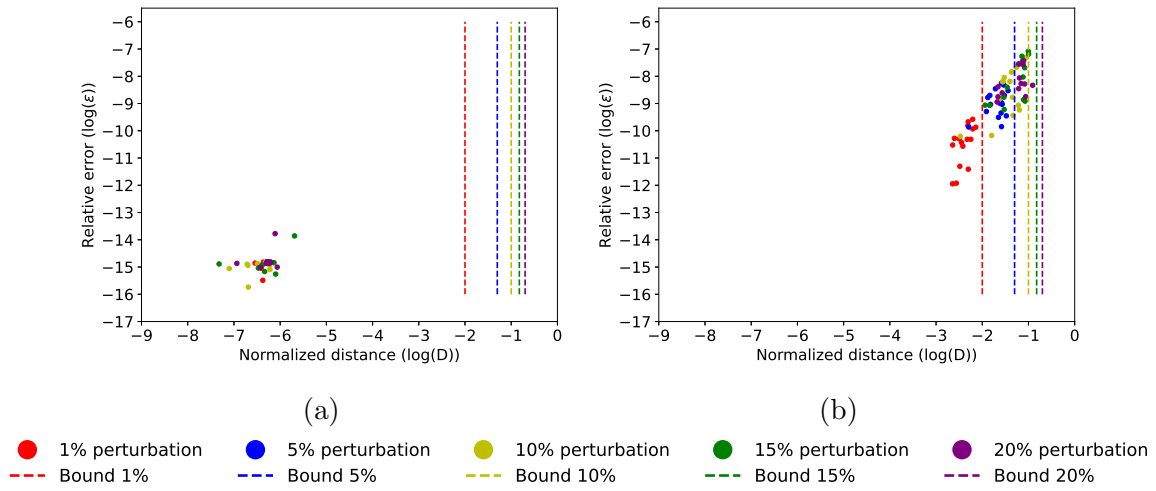

Figure 2.7: Relative error ϵ (Eq. 2.8) versus the normalized distance (Eq. 2.9) between minimum reached and reference for the optimization of Butenas' model using TNC (optimization of two sets of four variables). The dots signifies that the initial guess for each variable deviates by no more than corresponding percentage of random perturbation. The vertical dashed lines indicate the theoretical maximum distance corresponding to each amplitude of random perturbations. Different colors represent different perturbations values. (a) Optimization condition is M_38_28_04a in Table 2.5. The coagulation model adapted here is Butenas's model. Four initial concentrations are considered as varibales: ATIII, II, TF and TFPI; (b). Optimization condition is M_38_28_04b in Table 2.5. The coagulation model adapted here is Butenas's model. Four initial concentrations are considered as varibales: IX.V.TF and TFPI

Table 2.10:: Results of optimization of Butenas' model with four variables (either ATIII, II,TF and TFPI (M_38_28_04a) or V, IX, TF,and TFPI(M_38_28_04b)) using TNC. The initial values are obtained by perturbing the reference values by up to 20%.

	ATIII	II	TF	TFPI	Relative error
Min	100.0%	100.0%	99.9%	99.9%	1.834×10^{-16}
Max	100.0%	100.0%	99.9%	99.9%	1.676×10^{-14}
	V	IX	TF	TFPI	Relative error
Min	99.6%	97.9%	94.3%	96.2%	1.132×10^{-12}
Max	116.3%	107.8%	111.4%	110.6%	8.194×10^{-8}

2.3.4 Seeking for the global minimum

It has been demonstrated that gradient-based method is incapable to identify the global minimum under condition M_38_28_10. However, gradient-based methods play a supportive role in global optimization. On one hand, TNC is not directly integrated into the core methodology of the hybrid optimizer due to its high tendency to become trapped in local minima. Instead, it is used to illustrate the complexity challenges inherent in full coagulation models. On the other hand, even another gradient-based method, L-BFGS-B, fails to consistently find the global minimum in 100 independent random optimizations. However, it proves effective in optimizing a subset of variables. Its results were subsequently utilized in the outer optimization step of the novel hybrid optimization approach. Consequently, an efficient evolutionary algorithm, CMA-ES was utilized to search for the global minimum under condition M_38_28_10. Given that performing this type of optimization in a 10-dimensional space is computationally expensive, only 5 results are presented, as displayed in Table 2.11. This table provides a comparative analysis of the optimization outcomes for two distinct methods, CMA-ES and L-BFGS-B, across five different scenarios characterized by unique random initial guesses. The table displays key metrics such as the percentage values for various coagulation factors, relative errors, and distances to the reference for each case. These findings indicate that despite using the CMA-ES algorithm, locating the global minimum remains a challenge and neither method consistently achieves a global minimum. This phenomena highlights the importance of using hybrid optimization under these conditions.

Table 2.11:: Comparison of optimization outcomes using CMA-ES and L-BFGS-B methods across five different cases, each initiated with a unique random guess. This table showcases the variability and performance consistency of each method under identical conditions with varied initial guesses. M_38_28_10 is being solved.

	Case 1		Case 2		Case 3		Case 4		Case 5	
	CMA-ES	L-BFGS-B	CMA-ES	L-BFGS-B	CMA-ES	L-BFGS-B	CMA-ES	L-BFGS-B	CMA-ES	L-BFGS-B
ATIII	99.9%	99.8%	99.9%	99.6%	99.9%	100.0%	99.9%	100.0%	99.9%	99.8%
II	99.9%	99.7%	99.9%	99.3%	99.9%	100.0%	99.9%	100.1%	99.9%	99.8%
IX	104.3%	112.0%	102.8%	106.0%	104.1%	111.2%	104.4%	103.0%	105.6%	111.8%
TF	83.1%	81.1%	83.7%	82.4%	83.8%	81.7%	83.6%	84.2%	84.9%	79.1%
TFPI	86.6%	89.5%	86.1%	87.5%	87.2%	87.4%	87.3%	86.3%	89.7%	79.8%
V	101.3%	97.9%	99.9%	97.1%	101.2%	103.5%	101.4%	99.6%	104.4%	88.8%
VII	115.7%	102.3%	115.5%	115.4%	114.7%	112.6%	114.2%	116.2%	112.5%	108.9%
VIII	100.8%	101.6%	100.9%	106.5%	100.8%	96.8%	100.7%	99.7%	100.8%	91.1%
VIIa	116.7%	114.7%	114.9%	118.9%	115.7%	117.1%	115.6%	115.4%	114.8%	111.9%
X	100.6%	110.7%	100.4%	114.8%	100.5%	102.1%	100.5%	99.4%	99.9%	109.2%
Relative error	2.53×10^{-14}	3.42×10^{-11}	2.47×10^{-14}	1.36×10^{-10}	2.31×10^{-14}	3.24×10^{-11}	2.36×10^{-14}	1.42×10^{-12}	5.61×10^{-14}	2.11×10^{-10}
Distance to reference	0.101	0.098	0.096	0.117	0.095	0.105	0.094	0.097	0.087	0.122

To start the global optimization, L-BFGS-B was used to optimize 100 random optimization with initial guesses varying from 80% to 120% of the reference as the outer global optimization. The final results of these optimizations are shown in Table 2.12, which shows that the concentrations of ATIII and II do not vary a lot from one case to the other. Thus, the concentrations of these species were fixed during the following inner optimization, while the ranges observed for the other variables were set as strict min/max bounds. With the new bounds and variables remaining, the inner optimization used CMA-ES and the global minima obtained are shown in Table 2.13 for 5 different initial guesses. Both the relative error and optimized-to-reference distance are very small. The best relative error is 1.68×10^{-16} with a distance of 6.38×10^{-4} and the max value is 1.00×10^{-14} with a distance of 2.03×10^{-3}. Low levels of distances and relative errors of the five solutions demonstrate that they are indeed much better than the solutions from the gradient based method (See Figure 2.3b). These five minima are identified as numerical global minima, as the corresponding error values approach machine precision.

Table 2.12:: Summary of outer optimization (in hybrid optimizer) outcome of 100 L-BFGS-B optimizations (perturbation up to 20%).

Name	ATIII	II	IX	TF	TFPI	V	VII	VIII	VIIa	X
Lower	100%	100%	88%	83%	86%	88%	82%	95%	90%	94%
Upper	100%	100%	114%	108%	111%	114%	113%	102%	116%	107%

Table 2.13:: Summary of some outcomes of inner optimization (in hybrid optimizer) using CMA-ES.

	Case 1	Case 2	Case 3	Case 4	Case 5
ATIII	fix at 100%	fix at 100%	fix at 100%	fix at 100%	fix at 100%
II	fix at 100%	fix at 100%	fix at 100%	fix at 100%	fix at 100%
IX	100.0%	99.8%	99.9%	99.9%	100.0%
TF	99.9%	100.0%	100.0%	100.1%	99.9%
TFPI	99.9%	100.0%	100.0%	100.0%	100.0%
V	100.0%	100.0%	100.0%	100.0%	100.0%
VII	100.0%	100.0%	100.0%	100.0%	100.1%
VIII	100.0%	100.0%	100.0%	100.0%	100.0%
VIIa	100.0%	99.7%	99.9%	99.9%	100.1%
X	100.0%	100.0%	99.9%	100.0%	100.0%
relative error	3.74×10^{-16}	1.00×10^{-14}	8.22×10^{-16}	1.59×10^{-16}	1.68×10^{-16}
distance to reference	4.21×10^{-4}	2.03×10^{-3}	6.42×10^{-4}	3.53×10^{-4}	6.38×10^{-4}

2.4 Optimization using experiment data

So far, the optimization algorithms are tested in a fully defined parameter space where all reaction rates and initial conditions are precisely known. This allows for a detailed evaluation of algorithm efficiency and convergence properties. However, real-world applicability requires moving beyond numerical validation and applying the optimization framework to experimental data. The experimental data were chosen based on their clinical relevance, availability of time-resolved thrombin generation profiles, and compatibility with the model structure. Only well-characterized assays with known initial conditions were used to ensure meaningful optimization and reliable validation.

Firstly, optimization of Butenas' model was performed targeting at experiment data from [5] rather than numerically generated reference. The comparison in Figure 2.8 highlights the improved accuracy of thrombin generation predictions following optimization. In Figure 2.8a, where the optimization is based on 10 clotting factors, the optimized model shows closer agreement with the experimental data (black dots) compared to the original model. However, slight deviations remain in the start time, the peak time and the timing of thrombin decay which corresponds to systematic errors between experiment and this mathematical model. In order to diminish the natural error, the rate constants were set as variables as well. In Figure 2.8b, where the optimization includes 10 clotting factors and 44 rate constants, the optimized model shows an even stronger alignment with the experimental data.

2.4.1 Optimization in the pathological conditions of hemophilia A

A promising clinical application of this study involved adjusting the initial concentrations of the extrinsic pathway model to simultaneously predict experimental data curves under three different conditions of Factor VIII variation, simulating haemophilia A: 100% (normal level), 50% (moderate deficiency), and 15% (severe deficiency). The error Eq. 2.7 are slightly modified, for simulate the TGA under different conditions, in sections 2.4.1 and 2.4.2. To simulate the hemophelia A conditions, the loss function are nothing but just a summation of error under different level of VIII:

$$\epsilon = \epsilon_{VIII_{100\%}} + \epsilon_{VIII_{50\%}} + \epsilon_{VIII_{15\%}} \tag{2.18}$$

Eq. 2.18 represents the total error, ϵ, as the sum of errors across three experimental conditions: $VIII_{100\%}$, $VIII_{50\%}$, and $VIII_{15\%}$. Each term quantifies the relative

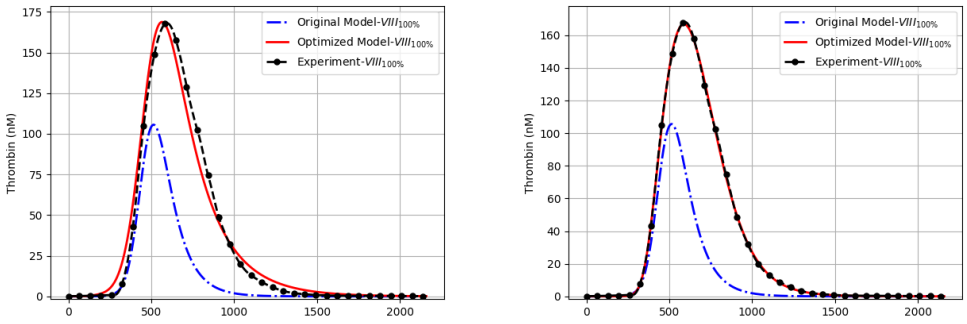

(a) (b)

Figure 2.8: Comparison of thrombin generation under two optimization scenarios. (a) Thrombin generation comparing the original model (blue dashed line), optimized model (red solid line), and experimental data. The variables are 10 clotting factors. (b) Thrombin generation comparing the original model (blue dashed line), optimized model (red solid line), and experimental data [5]. The variables are 10 clotting factors and 44 rate constants.

error between the optimized thrombin concentration and the experimental thrombin concentration over time under the corresponding factor VIII level. For example,

$$\epsilon_{VIII_{15\%}} = \frac{\int_0^{t_{\text{final}}} \left[IIa(t;\mathbf{x}^*|_{15\%VIII}) - IIa(t;\hat{\mathbf{x}}|_{15\%VIII})\right]^2 dt}{\int_0^{t_{\text{final}}} \left[IIa(t;\mathbf{x}^*|_{15\%VIII})\right]^2 dt} \tag{2.19}$$

In Eq. 2.19, $\hat{\mathbf{x}}|_{VIII=15\%}$ represents the parameter set $\hat{\mathbf{x}}$, where the concentration of Factor VIII is reduced to 15% of its corresponding value at the 100% condition (the optimized value). The numerator calculates the time-integrated squared differences between the simulated thrombin concentration, $IIa(t;\hat{\mathbf{x}}|_{15\%VIII})$, and the experimental thrombin concentration, $IIa(t;\mathbf{x}^*|_{15\%VIII})$, for the $VIII_{15\%}$ condition. The denominator normalizes this error using the total thrombin concentration from the experimental data under the $VIII_{15\%}$ condition.

In Figure 2.9, the original model shows noticeable discrepancies when predicting the thrombin concentration at different levels of Factor VIII (100%, 50%, and 15%). The optimized model (error refers to Eq. 2.18), on the other hand, closely matches the experimental data across all three conditions. This close alignment underscores the effectiveness of the optimization process in improving the models robustness under different Factor VIII levels, thereby improving its predictive accuracy. Table 2.14 shows that significant adjustments were made to the initial concentrations of several factors, notably factor II, IX, V, X and TF. However, some species hit the

bounds as shown in boldface in Table 2.14. This means that due to the constraints of bounds, the obtained minimum is not a mathematically optimal solution.

Table 2.14:: Final Optimized Initial Concentrations for VIII variations

Factor	Original initial concentrations (nM)	Optimized initial concentrations (nM)
ATIII	2267	2615.5
II	933	1941.7
IX	60	**30.6**
TF	0.001	0.0017
TFPI	1.667	1.728
V	13.33	5.01
VII	6.67	4.73
VIII	0.4667	**0.4**
VIIa	0.0667	0.103
X	106.67	**54.2**

2.4.2 Optimization in the conditions of anticoagulants treatment

Therapeutic agents regulating the coagulation cascade are essential in managing thrombotic disorders. Low molecular weight and synthetic heparins such as fondaparinux (Fpx) are widely used for both acute and long-term treatment of venous thromboembolism (VTE). In [6], computational models were compared with experimental data across different Fpx levels. Simulations predicted that 125 nM Fpx would approximately double the duration of the initiation phase and reduce thrombin generation rates by 2-fold. Empirical evaluations in synthetic coagulation proteomes proved these findings, showing a 2-fold prolongation of the initiation phase and a 1.5-fold suppression of peak thrombin generation rates. Although the simulations capture the overall trends observed in the experiments, they do not perfectly align with the experimental data. Additionally, initial concentrations of clotting factors are not directly measured. Therefore, it is meaningful to optimize the initial concentrations of mathematical models to fit the experiment observations.

Numerically, the function of Fpx was incorporated into the model by adding relevant equations to the existing differential equation framework. Experimental conditions were respected by setting the initial tissue factor (TF) concentration to 5 pM. Variables optimized in the model included the initial concentrations of FII, FV, FVII, FVIIa, FVIII, FIX, FX, TFPI, and ATIII. Based on the reaction scheme

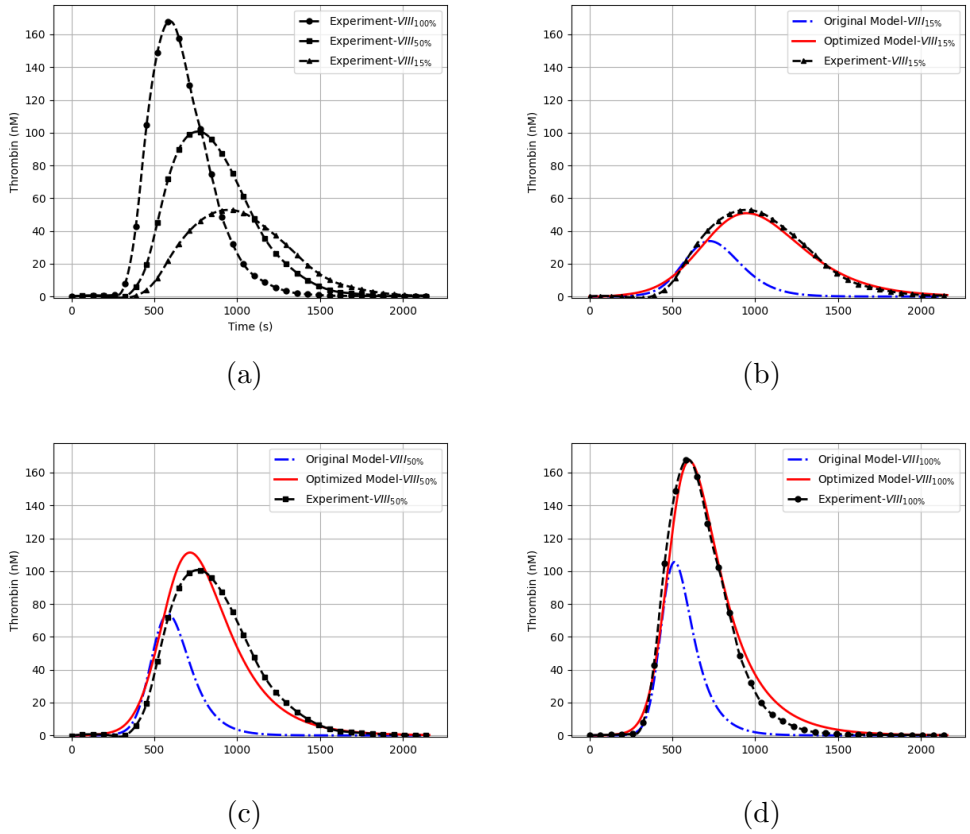

Figure 2.9: Thrombin generation for FVIII concentration levels (100%, 50%, and 15%) obtained from experimental data, the original model (blue dashed line), and the optimized model (red solid line; error refers to Eq. 2.18). (a) Experimental thrombin generation for $VIII_{100\%}$ (black dashed line with circle), $VIII_{50\%}$ (black dashed line with square), and $VIII_{15\%}$ (black dashed line with triangle). (b) Thrombin generation for $VIII_{15\%}$ comparing the original model, optimized model, and experimental data. (c) Thrombin generation for $VIII_{50\%}$ comparing the original model, optimized model, and experimental data. (d) Thrombin generation for $VIII_{100\%}$ comparing the original model, optimized model, and experimental data.

presented in Table 3.4, the reactions involving anticoagulants (See Table 2.15) were incorporated into the extrinsic pathway model. To ensure consistency with the original framework described in [6], the initial concentrations in the scheme were adjusted to align with the earliest version of the model as detailed in Table 2.16.

Figure 2.10 illustrates the comparison of thrombin generations obtained from experimental data, the original model, and the optimized model with or without Fpx treatment. For the 0 nM Fpx condition (see Figure 2.10a), the original model overestimates the thrombin peak, indicating that optimization significantly improves the fit to experimental data in untreated conditions. Under the 12.5 nM Fpx condition (see Figure 2.10b), both the original and optimized models predict reduced thrombin generation and time delay due to the anticoagulant effect of Fpx. Specifically, the peak values of thrombin concentration decrease from over 200 nM to below 150 nM, while the time to reach this peak is delayed from approximately 450 seconds to around 830 seconds for both. However, the optimized model again provides a closer match to the experimental data, particularly in the non-peak area. The original model overestimates thrombin levels and peak duration, suggesting that it fails to fully capture the inhibitory impact of Fpx even the optimized model underestimates the peak value.

Table 2.15:: Chemical reactions defining anticoagulation [6].

No.	Reaction	k_1	k_{-1}
1	$\text{Fpx} + \text{ATIII} \longleftrightarrow \text{Fpx=ATIII}$	$1 \times 10^8\ M^{-1}s^{-1}$	3.6
2	$\text{Fpx=ATIII} + \text{Xa} \longleftrightarrow \text{Fpx=ATIII=Xa}$	$3.1 \times 7.1^5\ M^{-1}s^{-1}$	
3	$\text{Fpx=ATIII} + \text{IXa} \longleftrightarrow \text{Fpx=ATIII=IXa}$	$3.1 \times 10^4\ M^{-1}s^{-1}$	
4	$\text{Fpx=ATIII} + \text{mIIa} \longrightarrow \text{Fpx=ATIII=mIIa}$	$7.1 \times 10^3\ M^{-1}s^{-1}$	
5	$\text{Fpx=ATIII} + \text{TF=VIIa} \longrightarrow \text{Fpx=ATIII=TF=VIIa}$	$2.3 \times 10^2\ M^{-1}s^{-1}$	
6	$\text{Fpx=ATIII} + \text{Xa=Va} \longrightarrow \text{Fpx=ATIII=Xa=Va}$	$8.6 \times 10^3\ M^{-1}s^{-1}$	
7	$\text{Fpx=ATIII} + \text{IIa} \longleftrightarrow \text{Fpx=ATIII=IIa}$	$1.4 \times 10^4\ M^{-1}s^{-1}$	

Multi-species optimization

The multi-objective optimization of thrombin (IIa), factor Xa, and factor VIIa dynamics was explored for several reasons. By including the dynamics of multiple species in the optimization process, the complexity is expected to be distributed across multiple species' dynamics. This would improve the likelihood of numerous local minima, as the optimization process becomes more constrained by the interplay of species. From aspect of clinical treatments, not all interventions should focus

Table 2.16:: Optimized initial concentrations with Fpx [6].

Factor	Original initial concentrations (nM)	Optimized initial concentrations (nM)
ATIII	3600.0	2490.00
II	1400	1461.60
IX	90	114.91
TFPI	2.50	0.93
V	20.00	24.00
VII	10	4.73
VIII	0.70	0.14
VIIa	0.10	0.12
X	160.00	224.00

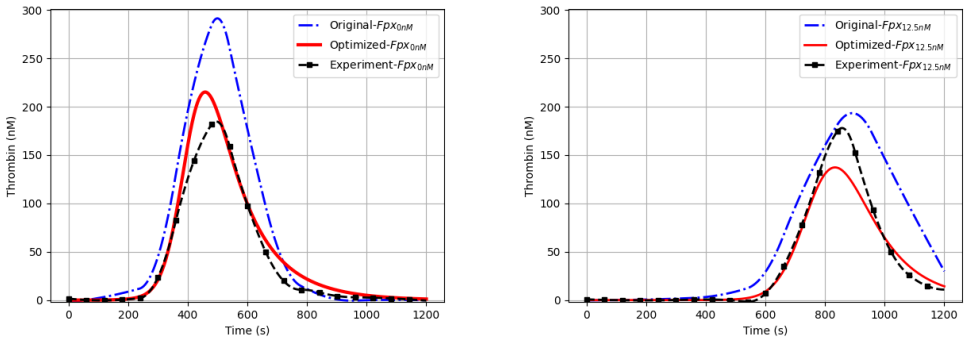

(a) (b)

Figure 2.10: Thrombin generation with or without fondaparinux treatment obtained from experimental data (black dashed line with square), the original model (blue dashed line), and the optimized model (red solid line). (a) Thrombin generation for 0 nmol fondaparinux. (b) Thrombin generation for 12.5 nmol fondaparinux.

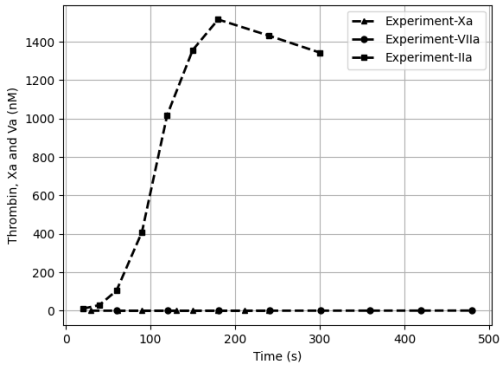

(a) Experimental data of generation of three species

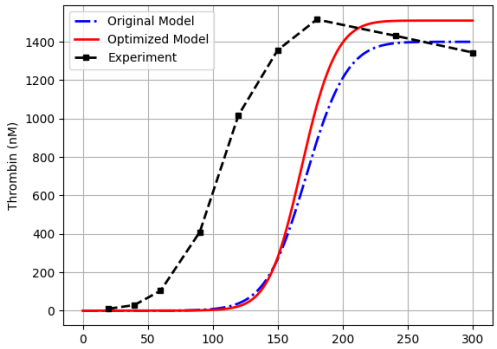

(b) IIa generation

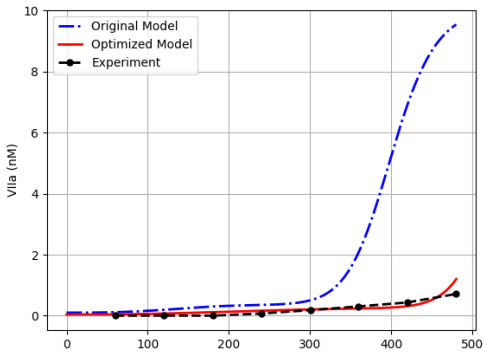

(c) VIIa generation

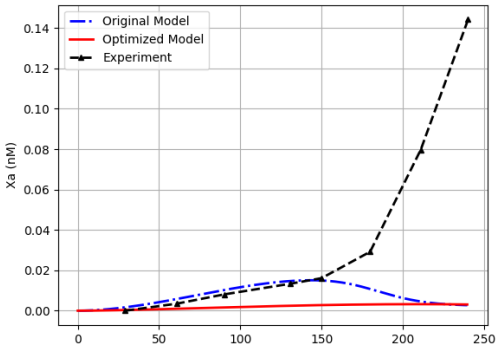

(d) Xa generation

Figure 2.11: Dynamics of three species (IIa, VIIa and Xa), comparing the original model (blue dashed line), optimized model (red solid line), and experimental data (black dashed line with symbols). (a) Experiment data: IIa; square; VIIa: cycle;Xa: triangle. (b) IIa generation. (c) VIIa generation. (d) Xa generation.

solely on thrombin. For example, anticoagulant drugs such as fondaparinux (Fpx) and heparin primarily target factor Xa, a critical enzyme upstream of thrombin in the coagulation cascade, meaning that the dynamics of Xa is worth evaluating as well. In addition, whether multiple species can be optimized at the same time can also evaluate the quality of the model. If the simulation result of multiple species cannot fit the experimental results together, it indicate the drawbacks of the scheme to some extent.

The multi-objective optimization process aims to minimize the combined error in the generation dynamics of thrombin (IIa), factor VIIa ($VIIa$), and factor Xa (Xa). The total loss function is defined as:

$$\epsilon = \epsilon^{IIa} + \epsilon^{VIIa} + \epsilon^{Xa} \tag{2.20}$$

Each term quantifies the deviation of the simulated species‘ dynamics from the corresponding experimental reference data. For example, the term ϵ^{Xa} in the loss function is defined as:

$$\epsilon^{Xa} = \frac{\int_0^{t_{\text{final}}} \left[Xa(t;\mathbf{x}^*) - Xa(t;\mathbf{x})\right]^2 dt}{\int_0^{t_{\text{final}}} \left[Xa(t;\mathbf{x}^*)\right]^2 dt} \tag{2.21}$$

where $Xa(t;\mathbf{x}^*)$ is the experimental Xa dynamics over time. $Xa(t;\mathbf{x})$ is the optimized dynamics of Xa using the current parameter set $\mathbf{x}$. The numerator computes the time-integrated squared difference between the experimental and optimized Xa dynamics. The denominator normalizes the error using the total integrated experimental dynamics of Xa. The same formulation applies for ϵ^{IIa} and ϵ^{VIIa} respectively.

The experiments in [104] served as the reference for this section. Butenas et al. [104] investigated the generation dynamics of thrombin, factor Xa, factor VIIa, and factor XIa, using highly sensitive and specific chromogenic and fluorogenic assays. The experimental setup utilized a reconstituted system comprising physiological concentrations of key coagulation factors, including factors II, VII, IX, X, XI, V, and VIII. The experiments were conducted using identical samples, which were subsequently divided into subsets for specific assays targeting individual species. This ensured consistency across all measurements except for the stimulus. The dynamics of thrombin (IIa) generation were primarily driven by 1.25 nM TF=VIIa complex, whereas the generation of Xa and VIIa was initiated directly by 1.25 nM TF. To align with the experimental setup, the initial concentrations of inhibitors (ATIII and TFPI) were set to zero. The variables considered in the model included factors II, VII, IX, X, XI, V, and VIII. For thrombin (IIa) generation, the system was initialized with TF = 0 and (TF=VIIa) = 1.25 nM to mimic experimental

conditions. Conversely, for the dynamics of VIIa and Xa, the initial setup was defined with TF = 1.25 nM and (TF=VIIa) = 0.

Figure 2.11 displays the dynamics of the three species, comparing the original model, optimized model (error refers to Eq. 2.20), and experimental data. In Figure 2.11b, the thrombin generation of optimized model aligns more closely with the experimental data compared to the one of original model. The peak thrombin level is reached more accurately, even the improvement is slight. However, neither model fully aligns with the experimental data (black dashed line with solid cycle). The timing of the peak is delayed in both models. In experiment, the thrombin concentration decreased after peak, although in absence of inhibitors. VIIa generation performs best among the three dynamics as shown in Figure 2.11c, due to the optimized model improves the match with the experimental data significantly. For Xa generation in Figure 2.11d, the optimized model displays no improvement over the original model. Both the original and optimized curves fail to closely follow the experimental data. They underestimate Xa generation, particularly during the late stages, where the experimental data shows a sharp rise that is not captured in the simulations. The results reveal that while the dynamics of VIIa were successfully optimized to closely match the experimental measurements, the dynamics of IIa and Xa showed significant deviations and were not optimized effectively.

2.5 Discussion and conclusions

This research contributes significantly to a relatively unexplored area, as there are only a few studies dedicated to the optimization of coagulation models to the extent presented here. Rojano et al. [9] optimized a simplified model to predict the dynamics of thrombin using a Python package designed for chemical reactions. Hansen et al. [77] applied a evolutionary algorithm for both internal and external optimization in model reduction. Ranc et al. [5] adjusted some rate constants and concentrations according to their knowledge and intuition in order to predict the generation of thrombin better than original models. However, no previous study has undertaken automated optimization of an exceedingly original model, analysed its complexity, and verified the minima as comprehensively as this study has.

As a reduced model, Rojano's model lacks a complex landscape, which eases the process of identifying global minima (refer to Figure 2.5a). On the other hand, Butenas' scheme under condition M_38_28_10 presents a more complex landscape. The prevalence of local minima in coagulation model optimization was shown in Figure 2.5b. These findings are useful for assessing the reliability of coagulation

cascade models. Models with numerous local minima, despite aligning well with experimental data, might depend on suboptimal parameters. This phenomenon reflects the inherent complexity of systems with numerous interconnected pathways and species. It suggests that model reduction could be advantageous while preserving its accuracy. The random variation of the +/- signs across species in the initial guesses introduces a diverse range of starting conditions. This diversity allows for a more comprehensive exploration of the model's response to changes in initial conditions. The findings from this approach underscore the importance of considering both the magnitude and the direction of initial perturbations when analysing the sensitivity and dynamics of the model.

The number of variables and their selection significantly influence the scheme's complexity as well, even when the model structure, reactions, and equations remain unchanged. For example, optimization under condition M_38_28_04a using classical gradient-based methods successfully led to the global minima (see Figure 2.5c). However, when the variables comply with M_38_28_04b, non-unique solutions were obtained, indicating a landscape peppered with local minima, as illustrated in Figure 2.5d. This observation highlights the importance of proper variable selection when modifying or optimizing concentrations in these models. It also indicates the importance of model reduction rather than just reduce dimensions based on a original model as well for avoiding existence of local minima in process of modifying coagulation models.

It is also observed that gradient-based optimization algorithms struggle to effectively identify global minima. The tendency of optimized solutions to cluster near the initial guesses suggests a propensity for the optimization process to settle into local minima. This results in suboptimal solutions, despite minimal gradients and a positive Hessian matrix.

Consequently, a hybrid optimizer was developed that combines gradient-based techniques with evolutionary strategies like CMAES to effectively locate global minima in models with complex landscape. This two-step strategy involves initially attempting to reduce the dimensions using a gradient-based optimizer and then using the hybrid optimizer to find global minima. The results demonstrate that the complexity of models with numerous local minima can be overcome, and a global minimum can be found, although this process is challenging and computationally intensive due to high cost of the outer and inner optimizations. In addition to error, the eigenvalues of the Hessian matrix and the distance between optimized variables and the reference were also used as criteria to determine whether a solution represents a global minimum. This hybrid approach and identification are particularly beneficial when model reduction is not anticipated or dynamics of each

species are requested.

The optimizations presented in this study demonstrates significant potential for clinical applications. While optimizing clotting factors alone improves the model's accuracy, incorporating rate constants addresses additional dynamics and enables a better fit to experimental data (Figure 2.8). This finding highlights the potential of parameters optimization for improving the predictive capability of coagulation models. By adjusting the initial concentrations of clotting factors, the optimized models accurately predicted thrombin generation under varying pathological conditions, including hemophilia A and anticoagulant treatment with fondaparinux (Fpx). For hemophilia A, the optimizer enabled precise alignment with experimental thrombin generation data across different levels of Factor VIII deficiency, enhancing the model's robustness and predictive accuracy (Figure 2.9). Similarly, for Fpx treatment, the optimized model successfully incorporated anticoagulant reactions and captured the effects of varying Fpx concentrations on thrombin generation, achieving closer agreement with experimental observations (Figure 2.10). The multi-species optimization result presented in Figure 2.11 reveals that the improvements achieved through optimization are insufficient to address the discrepancies between numerical simulations and experimental data. This highlights the inherent complexity of coagulation cascade and the limitations of currently used models in accurately capturing the dynamics of several species individually. The findings suggest that optimization efforts should go beyond concentration adjustments for multi-target optimization. Further optimization may not only involve fine-tuning rate constants but also rebuild the reaction mechanisms themselves.

In conclusion, this study focuses on a thorough examination of coagulation model optimization and its complexity under various conditions, ultimately developing a method to identify global minima. Although this chapter focuses on optimizing the initial concentrations of clotting factors, It is also expected that the optimized parameters (rate constants) will be capable of predicting outcomes for different experimental conditions such as varying initial concentrations.

Chapter 3

Multi-Step model reduction of coagulation cascade

The content of this chapter is based on a paper published in Biomechanics and Modeling in Mechanobiology, titled "Multistep Model Reduction of Coagulation Schemes" authored by Junyi Chen Quentin, Cazeres, Eleonore Riber, and Franck Nicoud.

Abstract

This chapter introduces a comprehensive multi-step model reduction technique for coagulation models, specifically targeting the dynamics of thrombin generation. By employing a synergistic approach that combines Direct Relation Graph with Error Propagation, chemical lumping, Quasi Steady State Assumption, and conservation analysis, the method efficiently reduces the complexity of original coagulation models without compromising accuracy. Applied to both extrinsic and intrinsic coagulation pathway schemes, this approach significantly diminishes the number of species and reactions, demonstrating its robustness through varied simulation conditions in the context of haemophilia. The findings underscore the potential of this reduction method to facilitate more efficient computational simulations that retain the essential characteristics of different coagulation models.

3.1 Introduction

Over recent decades, there has been considerable advancement in understanding the components of the hemostasis, encompassing the coagulation cascade, the formation of platelet plug, and fibrinolysis [79]. From the perspective of computational modeling, numerous frameworks have been devised to synthesize this biochemical knowledge, aiming to offer a comprehensive view of the system's dynamics [84]. For instance, Butenas et al. [15] introduced a model focused on the extrinsic pathway, comprising 34 species and 45 reactions, which has served as a foundation for many subsequent models. [52] developed a model that captures not just thrombin generation but also platelet activation, featuring 92 species and 148 reactions; Fogelson et al. [20] created a model that depicts clot formation under flow conditions, including 76 species and 105 reactions. Thrombin (IIa) being a key enzyme which interacts with various sub-systems and factors, converting fibrinogen into fibrin and activating platelets, in vivo experiments monitoring the evolution of thrombin concentration over time (Thrombin Generation Assay-TGA) are widely used as a global assessment of coagulation [89]. It is therefore natural to consider TGA and associated coagulation factors when developing schemes reduction strategies relevant to coagulation.

Advancements in numerical algorithms of CFD and computational capabilities have made it feasible to conduct precise and efficient numerical simulations of highly complex systems combining hemodynamics and coagulation cascade schemes which benefiting the evaluation of the thrombosis formation. Leiderman et al. [64] developed the first spatial–temporal mathematical model of platelet aggregation and coagulation under flow that includes details of coagulation biochemistry, chemical activation and deposition of blood platelets, as well as the two-way interaction between the fluid dynamics and the thrombosis growth. [66] developed a two-dimensional multi-scale model to study thrombus formation in blood vessels. On a more practical level, [105] used numerical simulations to analyze thrombin formation and location relative to tissue factor (TF) position in disturbed flow induced by an open venous valve.

Due to complex coagulation models involve dozens of species and hundreds of reactions, reduced coagulation model is essential to capture the key mechanisms, and practically to enable integration into Computational Fluid Dynamics (CFD) simulations. Additionally, complex models demand significant computational resources, limiting their feasibility for simulations in detailed geometries and maybe leading to convergence difficulties.

For instance, Bouchnita et al. [69] developed a model with only 7 species and 13 kinetic rates to simulate clots in a straight 3D tube. Wagenvoord et al. [106] proposed a reduced 10-species "minimal model" for thrombin generation, which showed good results when fitted to different experimental thrombin generation curves. However, the lack of a reported reaction rate parameter fitting procedure and the need to refit parameters for each case limit the usefulness of this model. A 2D model proposed by Sorensen et al. [107], adopts a more phenomenological approach, grouping most of species into categories like agonists and defines a reactive network that is broadly intended to reproduce coagulation dynamics. A highly reduced extrinsic pathway coagulation model (8 ODEs) under flow presented by Chen et al. [65] simulated fibrin formation and thrombin generation, accurately reflecting experimental data.

These models are reduced and more suitable for CFD applications. However, systematic and automatic reduction methods are desirable to further streamline the process and improve efficiency. Sagar et al. [76] developed a hybrid modeling approach combining ODEs with logical rules to simulate the coagulation cascade. The model consisted of five differential equations and logical rules resulting in a formulation significantly smaller than traditional mechanistic models. Hansen et al. [77] reduced a coagulation model from 34 species to 9 species using genetic algorithm. However, reactions in this reduced model of extrinsic pathway lose their original physical meaning. Mendez et al. [75] proposed a deeply simplified model with optimized rate constants. Ratto et al. [72] simplified a model to only three ordinary difference equations (ODEs) using conventional approximations which needs a large degree of mathematical derivation and expert intervene, and kinetic parameters adjustment to fit clinical data under different conditions. However, these methods are not physical method.

In different scientific communities (e.g. combustion, weather forecast, and other branches of biochemistry) sharing the objective to simplify chemical schemes, various physics-based reduction techniques have been developed. In contrast to other, aforementioned more intrusive methodologies, physics-based reduction methods seek to preserve as much as possible the structure of the original chemical kinetic model: all relevant chemical pathways are included, and there is no kinetic parameter optimization [108]. These guiding principles enhance robustness in complex simulations and improve the chemical interpretability of Computational Fluid Dynamics (CFD) results. For example, physic-based reduced model allows for the direct application of real diffusion coefficients, avoiding the limitations introduced by meta-species in intrusive reduction methods [77]. In some cases, CFD simulations need to capture multiple chemical species. This reduction method serves as a

strong foundation for such applications by preserving key biochemical interactions while simplifying the system [109]. In the context of thrombus formation, thrombin generation is essential for coagulation, while other clotting factors contribute to different stages of clot development, such as fibrin, which stabilizes the clot structure [78]. Using a physics-based reduction approach, the model efficiently incorporates multiple key species into CFD simulations, ensuring both accuracy and computational efficiency.

The objective of this chapter is to investigate to what extent coagulation models can be reduced by using physics-based methods. The coagulation framework as well as the reduction strategies considered are described in Section 3.2 and Section 3.3 respectively. Some outcomes of the proposed reduction methodology are discussed in Section 3.4.4 and 3.4.5, where it is shown that the reduced models reflect the thrombin generation accurately. The robustness of the scheme reduction procedure is further discussed in Section 3.4.6 where a variety of initial concentrations of coagulation factor VIII is considered to mimic haemophilia A conditions.

3.2 Coagulation framework

3.2.1 Computational models of coagulation cascade

This chapter presents the reduction of two existing computational models for the different pathways of the coagulation cascade. Both models consist in a set of ordinary differential equations (ODEs) that describes the time evolution of various coagulation factors, along with the rates of enzymatic reactions that govern the dynamics of the system; they were both validated through previous academic research [15, 19, 5]. In these computational models, the coagulation cascade can be represented by a set of ODEs:

$$\frac{d\mathbf{S}}{dt} = \mathbf{R} \tag{3.1}$$

where $\mathbf{S}$ contains the concentrations of the n chemical species involved in the cascade and $\mathbf{R}$ is the vector gathering all the associated source terms. The concentration evolution of all species in the coagulation cascade is determined by solving the corresponding set of ordinary differential equations (ODEs). In order to compute the source of terms $\mathbf{R}$, it is needed to know the rate constants, the concentrations of each species and the reaction scheme. This ODE system describes a 0D model for thrombin generation assay (TGA), where species dynamics are governed by reaction kinetics without spatial dependence. The system tracks the temporal evolution of clotting factors, with initial conditions defined by their concentrations at t = 0.

Then the ODEs for each species can be figured out according to the law of mass action, which states that the rate of reaction is proportional to the product of the concentrations of the reactants.

0D models can easily be implemented in CFD solvers to study the interplay between hemodynamics and coagulation. This was for example done by using an in-house numerical platform named YALES2BIO [110], [111] and [9] who used OpenFoam and [105] who relied on Comsol Multiphysics.

Extrinsic pathway model

An extrinsic pathway model was originally proposed by [18] and improved by [15]. This scheme was tested against independent experimental data by [5], who proposed a slightly modified version of this scheme; this is the one used in the present chapter. The cascade is initiated by tissue factor (TF) binding to factor VII, forming TF=VIIa complex. This complex then activates factor X to Xa, which then binds to activated factor V to convert factor II to IIa. During this process, protein C (PC), antithrombin III (ATIII), and tissue factor pathway inhibitor (TFPI) act as inhibitors. The details of this model is shown in appendix 3.6.1.

Intrinsic pathway model

The intrinsic pathway model proposed by [19] and modified by [5] was used in this chapter. The intrinsic pathway begins when factor XII is activated to XIIa once adsorbed to negatively charged surfaces. Then XIIa converts prekallikrein (PK) to kallikrein (K), further activating more factor XII to factor XIIa that activates factor XI to factor XIa. factor XIa activates factor IX to factor IXa. This cascade continues, leading to the activation of factor X to factor Xa in the presence of factor VIIIa, eventually converting II to IIa. This scheme is detailed in appendix 3.6.1 as well.

3.2.2 Quantities of interests and basic notations

Thrombin Generation Assay (TGA) is a comprehensive dynamic test that simultaneously measures thrombin production and its inhibition in real-time, as illustrated in Fig. 3.1. This figure also offers a physical interpretation of critical metrics used to analyse the outcome of a TGA, including: (i) the Endogenous Thrombin Potential (ETP), which evaluates the overall amount of thrombin

production; (ii) the peak thrombin level (IIa_{max}), denoting the highest concentration of thrombin achieved; (iii) the time to peak (τ_{max}), which is the duration required to reach IIa_{max}; and (iv) the lag time (τ_{lag}), the time needed to generate 10 nM of thrombin.

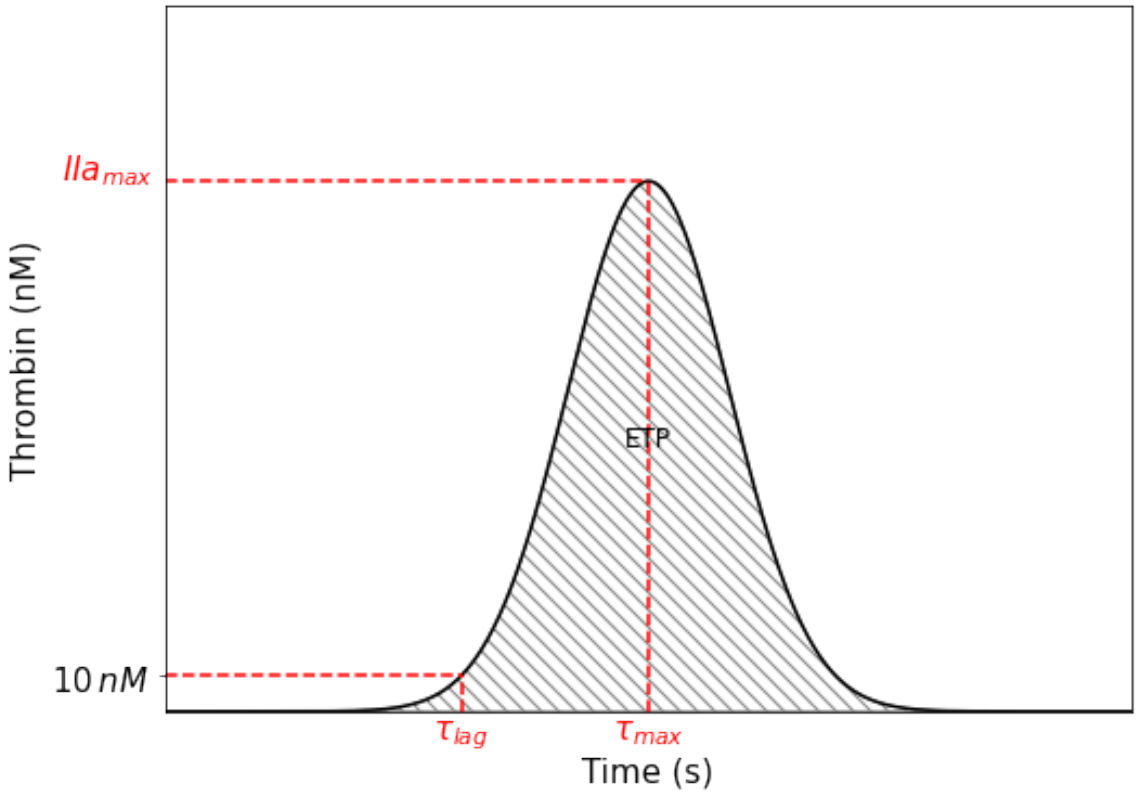

Figure 3.1: Quantities of interests. IIa_{max} (peak thrombin concentration), τ_{max} (time to peak), τ_{lag} (time to reach 10 nM of thrombin) and ETP (endogenous thrombin potential). Adapted from [5].

The chapter aims to simplify coagulation models while preserving accuracy in thrombin generation. To determine whether the model reduction is acceptable, an error metric is required. The error used in this work accounts for the quantities of interest depicted in Fig. 3.1 and is defined as:

$$E = \frac{\left(\frac{|ETP - ETP^{reduced}|}{ETP} + \frac{|IIa_{max} - IIa_{max}^{reduced}|}{IIa_{max}} + \frac{|\tau_{max} - \tau_{max}^{reduced}|}{\tau_{max}} + \frac{|\tau_{lag} - \tau_{lag}^{reduced}|}{\tau_{lag}}\right)}{4} \tag{3.2}$$

The superscript 'reduced' in Eq. 3.2 corresponds to the values of the reduced model. Here, equal weighting is assigned to these parameters because each is considered

equally important in the context of TGA, and each contribution is properly scaled. The error metric framework is inherently flexible; alternative weightings may be applied to emphasize particular parameters if certain outputs are regarded as having higher clinical or experimental priority.

It proves useful to introduce fundamental parameters in chemical kinetics. Considering both forward and backward reactions separately, the rate of the j^{th} reaction, denoted by ω_j, is given by:

$$\omega_j = k_j \prod_{i=1}^{n_S} [S_i]^{\nu'_{i,j}}, \tag{3.3}$$

where $[S_i]$ represents the concentrations of the i^{th} species, and n_S represents the overall number of species. The rate coefficient of reaction j is denoted by k_j. The stoichiometric coefficient for species i in the j^{th} reaction is $\nu_{i,j}$; it reads:

$$\nu_{i,j} = \nu''_{i,j} - \nu'_{i,j} \tag{3.4}$$

where $\nu'_{i,j}$ and $\nu''_{i,j}$ represent the stoichiometric coefficients of species i in reaction j on the reactant and product sides, respectively. In practice, $\nu''_{i,j}$ is either 0 or +1, $\nu'_{i,j}$ is either 0 or +1, so that $\nu_{i,j}$ is either −1, 0 or +1. Additionally, the production and consumption rates of species i are defined as follows, where n_R represents the total number of reactions:

$$P_i = \sum_{j=1}^{n_R} \max(0, \nu_{i,j} w_j) \tag{3.5}$$

$$C_i = \sum_{j=1}^{n_R} \max(0, -\nu_{i,j} w_j) \tag{3.6}$$

The formation rate of a species in a chemical reaction scheme can be determined by accounting for all reactions where the species is produced or consumed. The general expression for the net rate of production of species i is:

$$R_i = \sum_{j=1}^{n_R} \nu_{i,j} \omega_j \tag{3.7}$$

3.3 Physics-based reduction methods

The methods combined into the proposed multi-step strategy are the Direct Relation Graph with Error Propagation (DRGEP, for both species and reactions), Chemical Lumping, the Quasi Steady State Approximation (QSSA) and Conservation Analysis. The following subsections explain the principles and implementation of the aforementioned methods.

3.3.1 Direct Relation Graph with Error Propagation (DRGEP)

The principle of the DRGEP methodology is to identify the species and reactions that are not influential to key metrics and remove them from the schemes [112]. In order to quantify how much each species or reactions influence the evolution of the target species T, the so-called Direct Interaction Coefficients (DIC) are computed. Denoting i any species different from T, the coefficient which measures the influence of i on T reads:

$$d_{Ti} = \frac{\left|\sum_{j=1}^{n_R} \nu_{T,j}\omega_j\delta_i^j\right|}{\max(P_T, C_T)} \tag{3.8}$$

$$\delta_i^j = \begin{cases} 1 & \text{if the } \ jth \text{ reaction involves species } i, \\ 0 & \text{otherwise.} \end{cases} \tag{3.9}$$

where n_R is the number of reactions in the scheme, $\nu_{T,j}$ the stoichiometric coefficient of species T in the reaction j, ω_j the net rate of progress of reaction j, C_T and P_T the consumption and production rates of species T. For reactions, the DIC between a target species T and one reaction j is:

$$d_{Tj} = \frac{|\nu_{T,j}\omega_j|}{\max(P_T, C_T)}. \tag{3.10}$$

The coefficient d_{Ti} gives an evaluation of the dependence of target T on species i at time t when Eq. 3.8 is evaluated. To obtain a measure of the overall dependence of target T on species i throughout the TGA, we can consider the maximum value D_{Ti}:

$$D_{Ti} = \max_{\text{all paths,time}} d_{Ti} \tag{3.11}$$

The maximum over all paths in Eq. 3.11 means that there are multiple paths linking target and specific species, and the path that provides the highest value is used. A "path" refers to a sequence of linked species. A path begins from a target species and follows the directed edges to a destination. In Fig. 3.2, species A is the target, and paths such as A $\longrightarrow$ B $\longrightarrow$ D and A $\longrightarrow$ C $\longrightarrow$ D illustrate possible paths to reach species D. Global DRGEP coefficient of reaction j on target T named D_{Tj}, is calculated in a similar way:

$$D_{Tj} = \max_{\text{time}} d_{Tj} \tag{3.12}$$

Species or reactions are ranked based on global DRGEP coefficients (Eqs. 3.11 or 3.12) and gradually removed starting from the one with the smallest value, until the

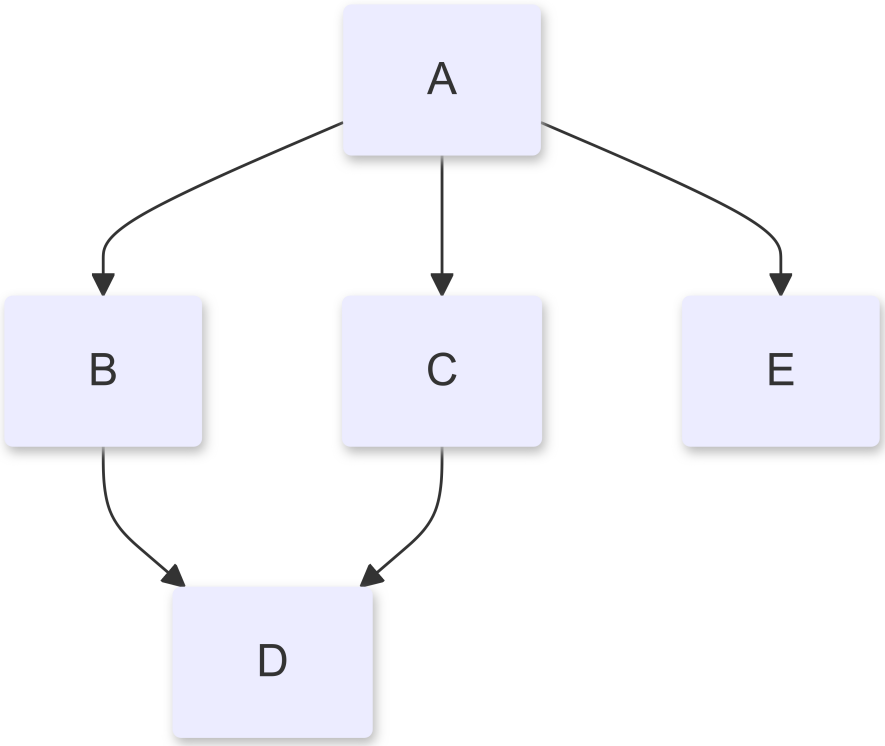

Figure 3.2: Concept of a "path" in DRGEP. Starting from the target species A, paths such as A $\longrightarrow$ B $\longrightarrow$ D and A $\longrightarrow$ C $\longrightarrow$ D demonstrate possible paths to reach species D.

error in the target quantities (Eq. 3.2 in this study) meets a user-defined criterion. Subsequently, the DRGEP coefficient is recalculated using the resulting reduced scheme. Iterations continue as long as the error on target quantities remains below a specific threshold (the user-defined criterion).

3.3.2 Chemical Lumping

Chemical lumping groups species with similar properties into one entity, with the aim of reducing the number of species without significantly altering the dynamics of the system [113]. In certain communities, such as combustion, candidate species for lumping are identified based on their molecular structures and thermodynamic properties. However, applying such criterion to species involved in processes like the coagulation cascade is very challenging. Hence, an alternative mathematical approach to lumping proposed by [114] is used in this study. This approach relies on the evolution of species concentrations to identify candidates and form lumped groups. Firstly, a normalized formation rate R_i^* for species i is defined as follows:

$$R_i^* = \frac{R_i}{[S_i]} \tag{3.13}$$

where R_i is the formation rate for species i.

If the initial concentrations of the two species i and i' are identical and the ratio:

$$\gamma_{ii'} = \frac{R_i^*}{R_{i'}^*} \tag{3.14}$$

does not vary over time, two species i and i' can be lumped. Note that if $[S_i] = [S_i'] = 0$, the ratio in Eq. 3.14 is redefined as $\gamma_{ii'} = \frac{R_i}{R_{i'}}$.

In nonlinear models, the conditions that initial concentrations are identical and that $\gamma_{ii'}$ is constant over time is usually not met consistently, hence it is relaxed allowing for an approximate lumping if:

$$|\gamma_{ii'} - \bar{\gamma}_{ii'}| \leq \epsilon \tag{3.15}$$

where $\bar{\gamma}_{ii'}$ is the time-averaged value of $\gamma_{ii'}$, and ϵ is a predefined tolerance. This tolerance is not unique and can produce different acceptable results over a wide range [114]. Note that the methodology can also be extended to deal with more than two individual components. Consider an original set of species $S = S_i$, $i = 1, \ldots, n_S$ and subdividing it into I lumped groups; within each group $\mathcal{L}_I$, a representative species is designated. The concentration of this representative is defined by:

$$[\tilde{S}_I] = \sum_{i \in \mathcal{L}_I} [S_i] \tag{3.16}$$

The fractional numbers α are assessed as [114]:

$$\alpha_i = \frac{R_i}{R_i + \sum_{j\in\{J\}} \gamma_{ij} R_{ij}} \tag{3.17}$$

Where J includes all the species lumped to a specific complex except species i. The concentrations of species S_i are calculated from the concentrations of grouped species and fraction number as:

$$[S_i] = \alpha_i[\tilde{S}_I] \tag{3.18}$$

New stoichiometric coefficients of lumped system are defined as:

$$\tilde{\nu}_{I,j} = \sum_{i\in\mathcal{L}_I} \nu_{i,j} \tag{3.19}$$

where $\mathcal{L}_I$, for $I = 1, \ldots, \tilde{n}_S$, represents a partition of the set S. New rate constants for the lumped system are then defined following the method outlined in [113]. This allows us to express the reaction rate in terms of lumped variables as:

$$\begin{aligned}
\omega_j &= k_j \prod_{I=1}^{n_S} ([S_i])^{\nu_{i,j}} \\
&= k_j \prod_{i=1}^{n_S} (\alpha_i[\tilde{S}_I])^{\nu_{i,j}} \\
&= k_j \prod_{i=1}^{n_S} \alpha_i^{\nu_{i,j}} \prod_{I=1}^{\tilde{N}_S} \prod_{i\in L_I} [\tilde{S}_I]^{\nu_{i,j}} \\
&= k_j \prod_{i=1}^{n_S} \alpha_i^{\nu_{i,j}} \prod_{I=1}^{\tilde{N}_S} [\tilde{S}_I]^{\sum_{i\in\mathcal{L}_I} \nu_{i,j}} \\
&= k_j \prod_{i=1}^{n_S} \alpha_i^{\nu_{i,j}} \prod_{I=1}^{\tilde{N}_S} [\tilde{S}_I]^{\tilde{\nu}_{I,j}}.
\end{aligned} \tag{3.20}$$

3.3.3 Quasi Steady State Assumptions

The concept of QSSA is that the production and consumption rates of some intermediate species are balanced, so that their concentration remain relatively constant throughout the reaction process [115]; the ODEs for the concentration of these particular species can then be removed from the set of equations to solve. Despite being over a century old, the Quasi-Steady-State Approximation (QSSA) remains widely used for simplifying complex reaction networks while preserving

essential system dynamics. QSSA also plays an important role in Computational Fluid Dynamics (CFD) simulations, where overcoming stiffness is a major challenge. For instance, [116] proposed the Iterative Dynamic Chemical Stiffness Removal (IDCSR) method, which builds upon QSSA principles and achieved substantial speed-up in both 0-D and 2-D simulations.

Several refinements have been developed to enhance QSSA's accuracy and applicability, such as Total QSSA (tQSSA), Prefactor QSSA (pQSSA) and Stochastic QSSA [117]. Beyond QSSA, alternative reduction techniques, such as Computational Singular Perturbation (CSP) [118] and Intrinsic Low-Dimensional Manifolds (ILDM) [119], transform coordinate systems to exploit timescale separation. However, these two methods may compromise physical interpretability when applied to complex biochemical systems. As a representative of these timescale exploitation methods, standard QSSA is applied here as part of the multi-step reduction.

Quasi-steady-state (QSS) approach typically requires detailed sensitivity analysis, which demands a significant amount of data [120]. However, it follows an alternative method outlined by [108], which avoids the need for sensitivity analysis. Instead, to identify QSS candidates among species, a modified level of importance for each species i is defined as follows:

$$L_i = D_{Ti}[S_i]\tau_i \tag{3.21}$$

where τ_i represents the timescale of species i, indicating the chemical lifetime, and D_{Ti} is the global DRGEP coefficient, defined in Eq. 3.8. Species are ranked in ascending order based on their L_i values, as described in Eq. 3.21, with smaller L_i values signifying likely QSS species. To simplify the calculation of Eq. 3.21, the product of concentration $[S_i]$ and timescale τ_i can be approximated by the integral of the concentration, which is readily obtained from the solution of the coagulation scheme, Eq. 3.1. Previously, some researchers have determined QSS species concentrations by analytically solving linear systems using the constraint that QSS species exhibit only linear coupling [112, 108]. Furthermore, optimization has been emerged as a useful tool for dealing with QSSA problems by [115]. In the present chapter, an optimizer based on python3 has been developed to figure out concentrations of QSS species, ensuring the simulation results align with the original models without QSSA in this chapter. The tool minimizes the overall error defined in Eq. 3.2, adjusting QSS species concentrations computationally.

3.3.4 Conservation Analysis

Conservation Analysis is a method to discover the linear quantity relations among species concentrations which holds over the duration of the simulation, if any [121]. If such relations exist, they allow to simplify the representation of the chemical system; note that contrary to the previous methodologies discussed in Sections 3.3.1 - 3.3.3, Conservation Analysis consists in an exact reformulation of the original kinetic scheme, without any loss of information and/or accuracy [122]. The existence of conservation relations indicates that the ODE system of model (Eq. 3.1) can be expressed as a system of differential algebraic equations:

$$\frac{d\mathbf{S}(t)}{dt} = \mathbf{N}\mathbf{v}(t) \tag{3.22}$$

where $\mathbf{S}(t) = [\mathbf{S}_1(t), \mathbf{S}_2(t), \cdots \mathbf{S}_p(t)]$ is the vector of $p = n_S$ species concentrations, $\mathbf{v}(t) = [\mathbf{v}_1(t), \mathbf{v}_2(t), \cdots \mathbf{v}_q(t)]$ is the vector of $q = n_R$ reactions rates and $\mathbf{N}$ is the stoichiometric matrix with p rows and q columns, relating the species to the reactions.

The rank of $\mathbf{N}$ is denoted by p_0. It follows that there are p_0 independent species and $(p - p_0)$ dependent species. Independent rows form an $p_0 \times q$ matrix $\mathbf{N_R}$ that is of full rank, and an $(p - p_0) \times q$ matrix $\mathbf{N_0}$ that comprises the dependent rows of the matrix. Through a series of transformations, a matrix $\mathbf{L_0}$ can be derived that establishes relations among independent species, dependent species, and constants [123]:

$$\frac{d\mathbf{S}(t)}{dt} = \begin{bmatrix} \frac{d\mathbf{S_i}(t)}{dt} \\ \frac{d\mathbf{S_d}(t)}{dt} \end{bmatrix} = \begin{bmatrix} \mathbf{N_R} \\ \mathbf{N_0} \end{bmatrix} \mathbf{v}(t) = \begin{bmatrix} \mathbf{I} \\ \mathbf{L_0} \end{bmatrix} \mathbf{N_R}\mathbf{v}(t) \tag{3.23}$$

where $\mathbf{I}$ represents a unit matrix. This equation can be written separately as:

$$\frac{d\mathbf{S_i}(t)}{dt} = \mathbf{N_R}\mathbf{v}(t) \quad \text{and} \quad \frac{d\mathbf{S_d}(t)}{dt} = \mathbf{L_0}\mathbf{N_R}\mathbf{v}(t) \tag{3.24}$$

The quantity relations among species are then expressed in terms of dependent and independent species as:

$$\frac{d\mathbf{S_d}(t)}{dt} - \mathbf{L_0}\frac{d\mathbf{S_i}(t)}{dt} = \mathbf{0} \tag{3.25}$$

By integrating Eq. 3.25, the conservative relations are:

$$\mathbf{S_d(t)} - \mathbf{L_0}\mathbf{S_i}(t) = \mathbf{T} \tag{3.26}$$

where $\mathbf{S_d}(t)$ denotes the dependent species which can be expressed from independent species $\mathbf{S_i}(t)$ and the vector $\mathbf{T}$ consisting of constant values.

3.3.5 Multi-step reduction process

[108] observed that optimizing the sequence of reduction steps, including potential repetitions of specific steps, can significantly improve the level of reduction achievable within a given error threshold. The procedure comprises several stages: 1. Reducing species; 2. Reducing reactions; 3. Lumping similar species; 4. Applying Quasi-Steady State Assumptions; 5. Performing conservation analysis. The initial step involves eliminating species and reactions through DRGEP steps due to the redundancies in the original models. After each iteration, which involves removing a species or reaction, the system representing the remaining network may undergo substantial changes. Consequently, it is essential to recompute the DRGEP ranking after each removing. Elimination of species and reactions was performed alternately until no more species or reactions could be removed. The eliminations using DRGEP are followed by chemical lumping, which is a one step process acting on the species only. Following lumping, the Quasi-Steady State Assumption (QSSA) is used to reduce the number of species for which a differential equation must be solved. The final step is conservation analysis, which again reduces the number of independent species and differential equations. Note that this process links dependent and independent species so that no change can be done afterwards (refer to Fig. 3.3). The whole process is designed to be automated, requiring no intermediate inputs or expert decisions. Since DRGEP acts on species and reactions, two orders may be considered. In what follows, the ordering SR and RS will be applied to the two typical schemes detailed in Section 3.2. SR indicates the process start with reducing species and followed by reducing reactions, and RS is the reverse.

3.4 Practical cases

3.4.1 Reference models for validation

The performance of the reduction algorithm is assessed by considering two widely-used and newly-revised coagulation models which are described in section 3.2.1 and 3.6.1. The extrinsic pathway model [15] is a hallmark in coagulation modeling and serves as the foundation for many studies in the field. The intrinsic pathway model [5], on the other hand, is derived from another hallmark model [19]

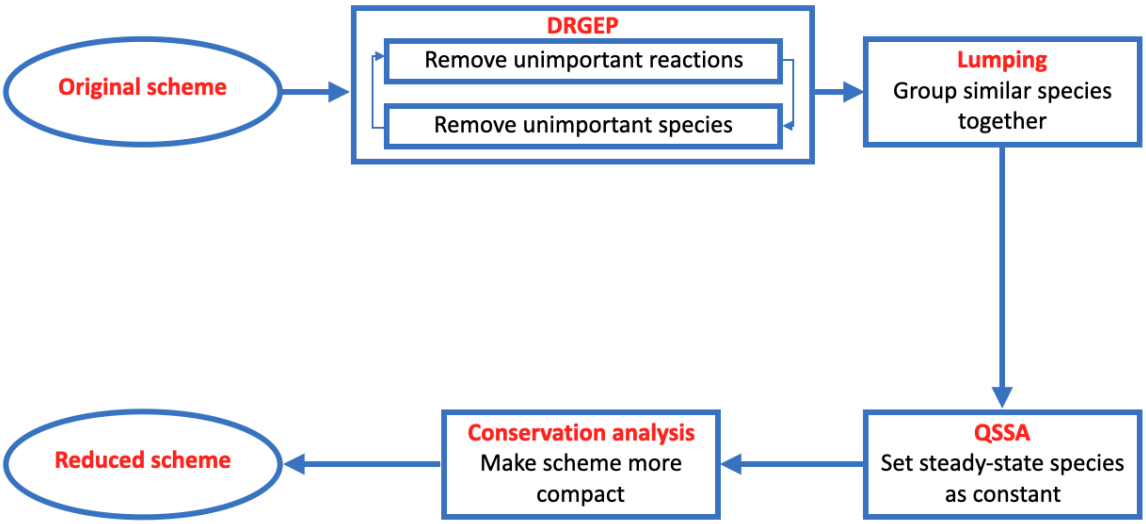

Figure 3.3: Schematic of multi-step reduction. Starting with the original schemes, the process involves a series of reduction steps to derive a simpler and more compact reduced scheme. The Directed Relation Graph with Error Propagation (DRGEP) technique is applied to eliminate insignificant reactions and species. Then, the system undergoes 'Lumping' to group similar species, followed by the Quasi-Steady-State Approximation (QSSA) to treat certain species concentrations as constant valued. The final conservation analysis ensures the reduced scheme maintains essential dynamical properties, culminating in a simplified yet accurate representation of the original scheme.

that specifically accounts for intrinsic pathway. The original complex models do not directly fit experimental data due to uncertainties in clotting factor concentrations, which are difficult to measure simultaneously in a single sample. Nevertheless, these models remain a critical reference in the field. After optimizing clotting factor concentrations, the complex model aligns well with experimental observations. This optimization is a separate effort and is not discussed further in this chapter. More details about the optimisation are provided previously.

3.4.2 Numerical setup

In order to consider all methods comprehensively, the criterion for DRGEP, the tolerance fo Lumping and threshold for QSSA are set moderately. The user-defined criterion for DRGEP is set to 5%. The predefined tolerance for lumping in Eq. 3.15 is 0.1 for both the extrinsic and intrinsic pathway models. However, despite using the same tolerance, the effect of lumping differs between the two models. Similarly, the QSSA threshold for Eq. 3.21 to define the candidates is also set to 0.1.

3.4.3 Optimization of methods sequences

The reduction methodologies for both extrinsic and intrinsic way models are illustrated in Figs. 3.4 and 3.5. For the extrinsic pathway model, the orders of DRGEP did not influence remarkably the reduced scheme obtained at the end of the procedure (refer to Fig. 3.4). For the intrinsic pathway model, the number of reactions after reduction is affected by the RS/SR ordering very slightly (by only 1), while the number of species is not (refer to Fig. 3.5). Therefore, for both extrinsic and intrinsic pathway models, all the reduction results discussed in the remaining sections were simulated according to the SR ordering.

3.4.4 Reduction of extrinsic pathway model

The reduction of the extrinsic pathway model resulted in a decrease in the number of species from 35 to 19 and a reduction in the number of reactions from 46 to 23, which is detailed in Table 3.1, while Fig. 3.4a shows the effects of each steps. Starting from the original scheme with 35 species and 46 reactions, the first species reduction using DRGEP (S) lowers the number of species to 30, while the number of reactions decreases to 38. This is followed by reaction reduction using DRGEP (R), which results in a drop in the number of reactions to 32, while the number of

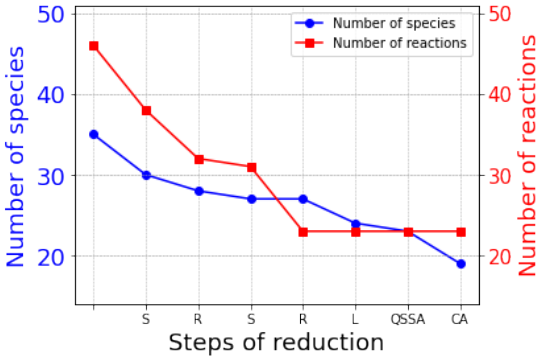

(a) Extrinsic pathway model: SR

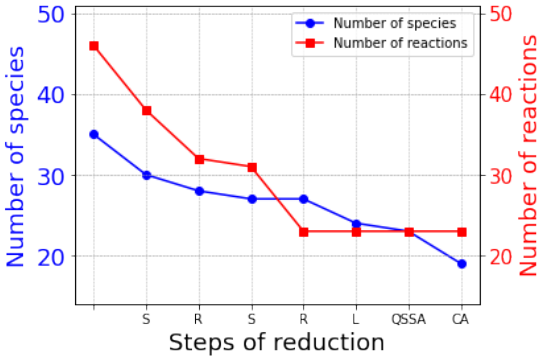

(b) Extrinsic pathway model: RS

Figure 3.4: Reduction process of extrinsic pathway models: number of species (blue line with circles) and number of reactions (red line with squares). On the abscissa axis, 'S' stands for species reduction using DRGEP, 'R' for reactions reduction using DRGEP, 'L' for lumping, 'QSSA' for Quasi-Steady State approximation step and 'CA' for conservation analysis.

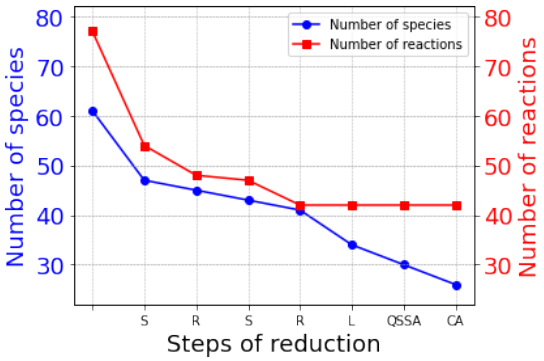

(a) Intrinsic pathway model: SR

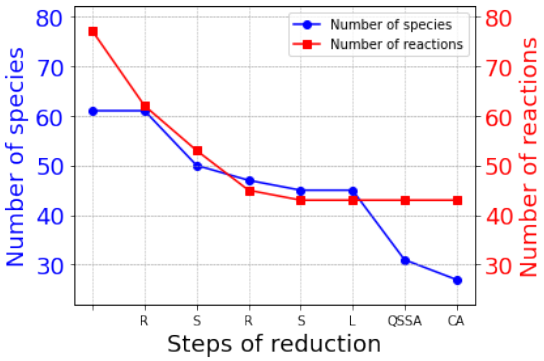

(b) Intrinsic pathway model: RS

Figure 3.5: Reduction process of intrinsic models: number of species (blue line with circles) and number of reactions (red line with squares). On the abscissa axis,'S' stands for species reduction using DRGEP, 'R' for reactions reduction using DRGEP, 'L' for lumping, 'QSSA' for Quasi-Steady State approximation and 'CA' for conservation analysis.

species decreases to 28. A second round of species reduction (S) further decreases the number of species by 1, with the number of reactions going to 31. The second reactions reduction (R) leads to 23 reactions and 27 species. The number of reactions remains constant at 23 from this point onward. As the reduction process continues, lumping (L) leads to another decline, reducing the number of species to 24. The application of QSSA reduces the number of species to 23. Finally, Conservation Analysis (CA) achieves the most compact model, reducing the system to 19 species. The final error is remarkably low, at only 2.3%. This small error margin indicates a high similarity in thrombin generation between the reduced and the original models, as depicted in Fig. 3.6a.

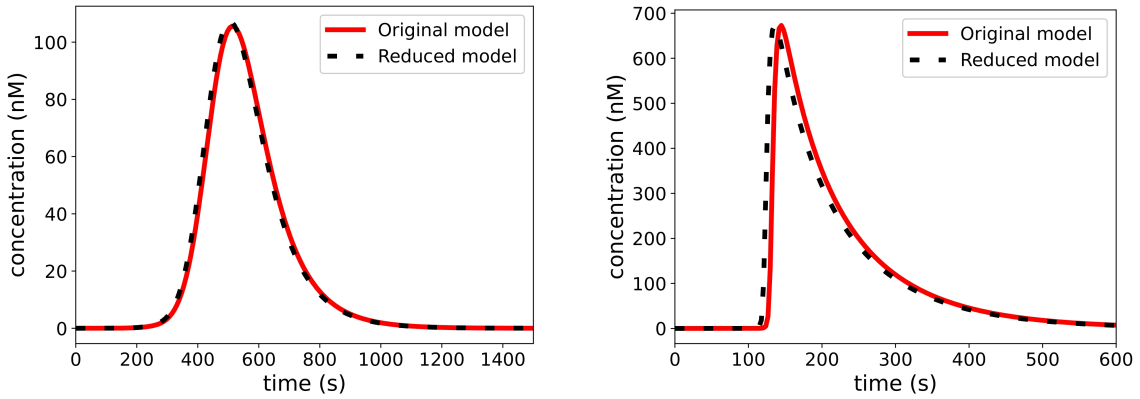

(a) Extrinsic pathway model

(b) Intrinsic pathway model

Figure 3.6: Thrombin generation (a) Extrinsic pathway; (b) Intrinsic pathway. Comparison between original model (solid red lines) and reduced model (dashed black lines).

Table 3.1:: Comparison of original and reduced extrinsic pathway models. (user-defined criterion for DRGEP: 5%; chemical lumping tolerance: 0.1; QSSA threshold: 0.1).

	Original Model	**Reduced Model**
Number of species	35	19
Number of reactions	46	23
Reduction ratio of species	–	45%
Reduction ratio of reactions	–	50%
Error	–	2.3%

Of course, some species are more important than others in the kinetic

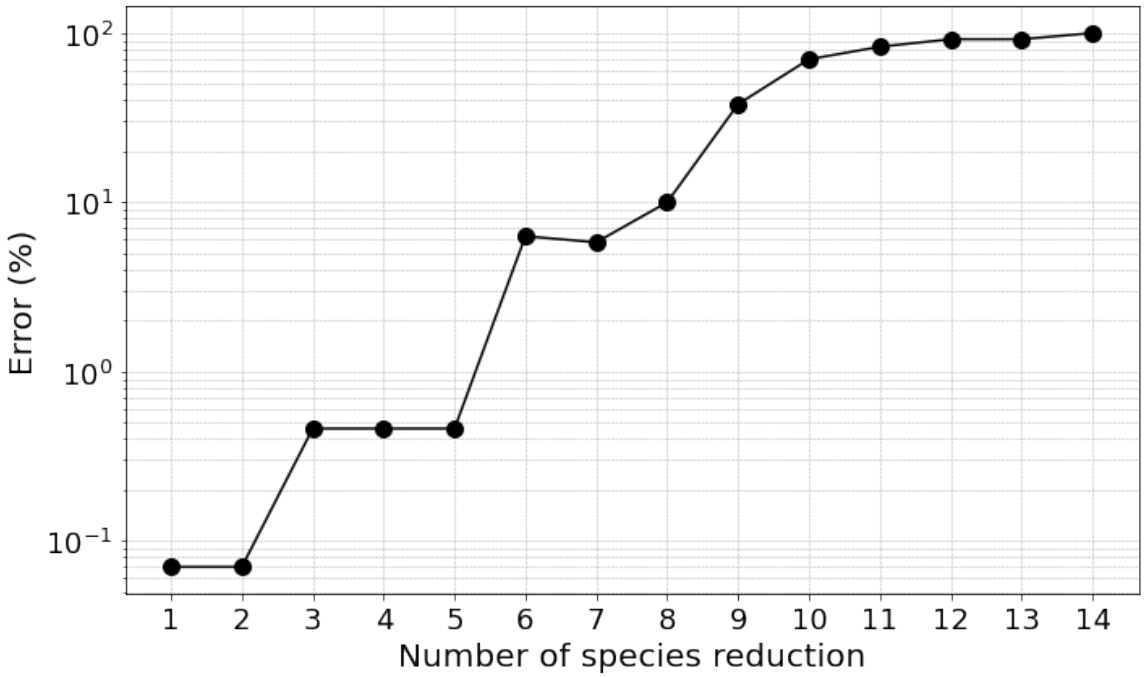

Figure 3.7: The error in Eq. 3.2 as a function of of number of species reduction by DRGEP in the extrinsic pathway model (until the error reaches 100%).

mechanisms; this results in a non-homogeneous increase in the error in the DRGEP phase, as illustrated in Fig. 3.7, which shows how the error (Eq. 3.2) evolves as the number of species removed for the extrinsic model increases. The error remains constant when the first and second, third and fifth species are removed; it is especially after the removal of the sixth species (TF) that the error increases considerably, going from 0.46% to 6.3%. Interestingly, the error decreases slightly when the 7th species is removed. However, beyond this point, the error gradually increases, reaching approximately 10% after the removal of the 8th species. The increase becomes more pronounced, rising sharply to around 40%, a level that is no longer acceptable. Finally, the error escalates to 100% upon the removal of the 14th species, indicating a complete loss of accuracy.

3.4.5 Reduction of the intrinsic pathway model

The intrinsic pathway model underwent a multi-step reduction process, resulting in a scheme with 26 species and 42 reactions, compared to the original scheme's 61 species and 77 reactions (refer to Table 3.2). The reduction process is depicted in Fig. 3.5a, showcasing the sequence of steps from the original to the final reduced

model. Starting from the original scheme with 61 species and 77 reactions, the first species reduction step (S) using DRGEP significantly lowers the number of species to 48, while the number of reactions drops to 54. The subsequent reaction reduction step (R) further reduces the number of reactions to 49, while the species count drops to 45. A second species reduction step (S) leads to a gradual decline in species count to 43, while the reaction count continues to decrease to 48. The second reaction reduction step (R) reduces the number of reactions to 42, while its impact on species count is minimal, decreasing by only one species. Lumping (L) further reduces the number of species to 34, while the number of reactions stabilizes at 42 and remains constant through the QSSA and Conservation Analysis (CA) steps. The final reduced model contains 26 species and 42 reactions. Upon comparison, the reduced model closely aligns with the detailed one, demonstrating only a 3.5% error, as shown in Fig. 3.6b, which indicates a good preservation of the behavior of original model, although a very slight shift to the left exists.

Table 3.2:: Comparison of original and reduced intrinsic pathway models. (user-defined criterion for DRGEP: 5%; chemical lumping tolerance: 0.1; QSSA threshold: 0.1).

	Original Model	**Reduced Model**
Number of species	61	26
Number of reactions	77	42
Reduction ratio of species	–	46%
Reduction ratio of reactions	–	45%
Error	–	3.5%

3.4.6 Robustness and generality

Reduction algorithms do not always preserve the generality of the original models. To assess the robustness of the reduced models in simulating haemophilia A conditions, the initial concentration of factor VIII was varied from 100% (the normal level in original models) to 10% (100%, 50%, 10%), as documented by [5]. Fig. 3.8 presents the comparison of thrombin generation dynamics between the original and reduced models under different factor VIII concentrations (100%, 50%, and 10%). Both the extrinsic and intrinsic pathway schemes are analyzed to assess the robustness of the reduced models in simulating haemophilia A conditions.

The thrombin generation of the original and reduced extrinsic pathway models

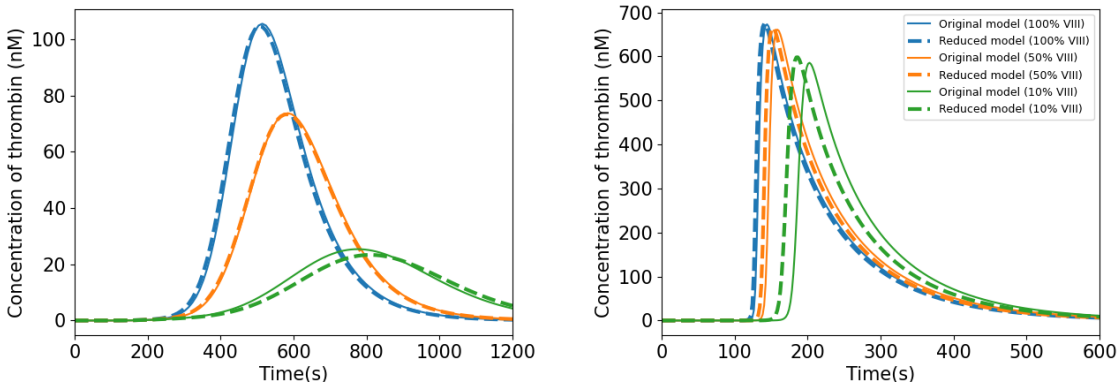

(a) Extrinsic pathway scheme

(b) Intrinsic pathway scheme

Figure 3.8: Thrombin generation across a range of VIII concentrations (100%, 50%, 10%. Each color represents a different concentration level. Solid lines indicate simulations obtained from original models, while dashed lines represent simulations obtained from reduced models. Blue: normal (100%) VIII; Orange: 50% VIII; Green: 10% VIII.

show excellent agreement across all tested concentrations of factor VIII, as illustrated in Fig. 3.8a. The error between the original and reduced models increases as factor VIII concentration decreases, particularly at 10% VIII. Before reaching peak thrombin concentration, a visible gap emerges between the original and reduced models, indicating that the reduced model does not fully capture the early-phase thrombin generation dynamics at lower VIII levels (10% VIII). After the peak, the discrepancy between the original and reduced models diminishes, and the two profiles converge. This suggests that the reduction method effectively preserves late-phase thrombin decay, even under low factor VIII conditions. The overall trend suggests that the reduced model performs best at normal factor VIII levels but slightly deviates under conditions of severe deficiency. Future refinements could focus on improving early-stage thrombin prediction in the extrinsic pathway model. However, overall agreement between the original and reduced models remains strong.

A similar pattern was observed for the intrinsic pathway model (Fig. 3.8b), although with a more pronounced trend to underestimate τ_{max} (see the left shift in Fig. 3.8b). The difference between the original and reduced models increases as factor VIII concentration decreases. This effect is particularly noticeable at 10% factor VIII. However, unlike the profile of extrinsic pathway model in Fig 3.8a, the peak thrombin concentration is slightly higher in the reduced model at 10% factor VIII levels rather than being underestimated. Additionally, the time to peak

($\tau_{\max}$) occurs earlier, indicating that the reduced model predicts a faster thrombin response compared to the original model. Before and after the peak, the difference between the original and reduced models remains notable. Despite these differences, the general trend of thrombin generation with decreasing factor VIII levels is well captured, demonstrating that the reduced model retains the essential characteristics of haemophilia A conditions.

For both pathway models, the agreement confirms that the reduction process, designed for normal concentrations of factor VIII, faithfully preserves the ability of the models to reflect the impact of haemophilia A on thrombin generation.

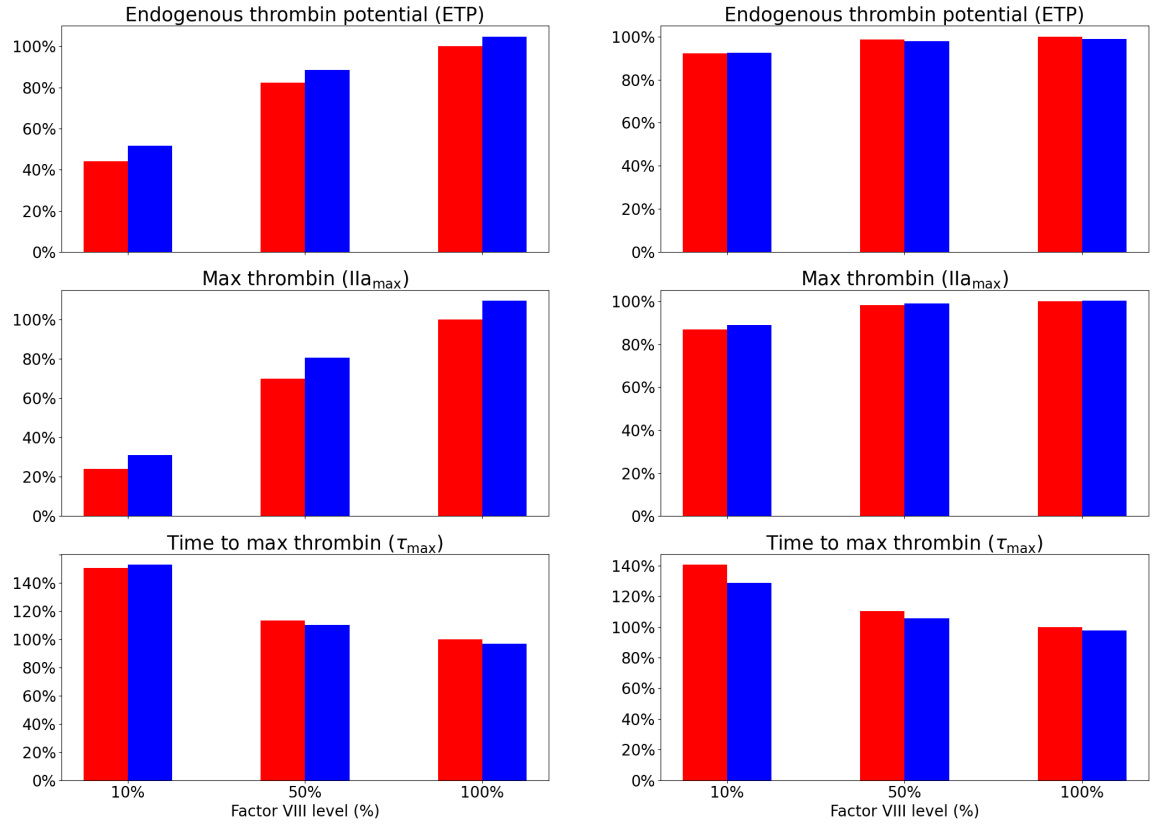

(a) Extrinsic pathway scheme

(b) Intrinsic pathway scheme

Figure 3.9: Thrombin generation metrics for both extrinsic and intrinsic pathway models under different factor VIII concentrations. RED: original models; BLUE: reduced models. The reduced model closely emulates the original in terms of ETP, IIa_{max}, and τ_{max}, validating the effectiveness of the reduction approach in capturing essential thrombin generation characteristics even at diminished factor VIII levels.

To further highlight the robustness and accuracy of the reduced model compared

to the original model across different factor VIII concentrations, Fig. 3.9 displays different quantities of interest under different conditions. For the extrinsic pathway, both original and reduced models exhibit a decrease in ETP as the factor VIII level decreases, which is expected due to the diminishing coagulation factors (refer to Fig. 3.9a). The reduced model closely follows the trend of the original model, indicating that essential dynamics are well-preserved. Similar to ETP, IIa_{max} decreases with lower factor VIII levels. The minor discrepancies observed suggest some nuances in peak thrombin generation that the reduced model approximates slightly differently. τ_{max} generally increases as factor VIII levels decrease, indicating slower thrombin generation under reduced coagulation factor concentrations. This trend is also very well captured by the reduced model, even if the generation of thrombin from the reduced model is a little bit faster than the one of the original model. Fig. 3.9b provides a comparative analysis for the intrinsic pathway scheme under similar varying conditions of factor VIII. ETP measurements in the intrinsic pathway mirror those observed in the extrinsic pathway, with a consistent reduction in thrombin potential as factor VIII decreases, even if the change is not so obvious as for the extrinsic pathway. IIa_{max} declines with decreasing factor VIII, which is well captured by both models. The increase in τ_{max} at lower factor VIII levels observed in the intrinsic pathway is similar to that in the extrinsic pathway, although τ_{max} of the reduced model is slightly smaller than that of the original model, consistently with the observation made in Fig. 3.8b.

3.5 Conclusion

The multi-stage reduction strategy introduced in this chapter for coagulation models proved effective when applied to both extrinsic and intrinsic pathways. By incorporating Direct Relation Graph with Error Propagation (DRGEP), chemical lumping, Quasi Steady State Assumption (QSSA), and conservation analysis, the methodology has demonstrated its efficacy by significantly reducing the complexity of detailed coagulation models while maintaining high fidelity to the original models' dynamic behavior.

Applied to a extrinsic pathway model originally encompassing 46 reactions and 35 species, the technique effectively reduced it to a more simplified model with 23 reactions and 19 species. This reduced model not only preserved the essential dynamics of thrombin generation but also performed robustly under varied factor VIII levels, a crucial feature for simulating haemophilia conditions. A substantial reduction was also obtained for the intrinsic pathway model (reactions from 77 to

42 and species from 61 to 26), while maintaining an excellent agreement with the original configuration, reinforcing the method's applicability and accuracy. Notably, the reduced models recover the dynamics of thrombin very nicely as shown in Fig. 3.8 in different levels of VIII, even they are adapted from the normal initial VIII level.

The findings confirm that the reduced models not only capture thrombin generation with high fidelity but also conserve the predictive capability of the original schemes for clinical scenarios, such as in haemophilia treatment. This highlights the efficacy of the multi-step, physics-based reduction approach in the simplification of complex coagulation models automatically, ensuring that they remain both accurate and robust for clinical use. However, lumping, similar to QSSA, may not be essential for regular applications but becomes particularly useful in computationally demanding tasks, such as parameter optimization [73], control systems [57] and sensitivity analysis [65].

In this chapter, the scheme reduction methodology is applied exclusively to thrombin generation assays (TGA), although it could be adapted to underflow configurations. The reduced model obtained from this multi-step reduction method is more physically meaningful and robust, which facilitates the application of real diffusion coefficients for CFD. This is particularly advantageous since intrusive reduction methods often replace real species with meta-species, which can obscure the true diffusion behavior of the system. Similarly, adapting the methodology to the case of kinetic schemes including Michaelis-Menten type enzymatic reactions would not pose any major difficulty, even if the application case chosen here only includes n-order reactions (n between 1 and 4). These adaptations will be the subject of future investigations.

This study relies on deterministic models, which describe the coagulation cascade through a set of ODEs with fixed parameters. Apart from them, another type of model is the stochastic models, such as kinetic Monte Carlo methods [51], which account for molecular fluctuations [124]. However, in this study, a deterministic framework is chosen due to its suitability for thrombin generation assays (TGA), where the reaction volume is at the μL scale [125] assuming that the reactions take place in a perfectly-stirred reactor. Additionally, deterministic models are more computationally efficient [51, 124] and more practical for integration with Computational Fluid Dynamics (CFD) simulations. For these reasons, this study focuses on deterministic models. However, in extreme small volume (nL and pL), molecular fluctuations become significant [51, 124], making stochastic modeling more relevant. Future work should explore model reduction for stochastic models of which the computation cost is very significant.

3.6 Details of models

All mathematical models used in this chapter are summarized in this section.

3.6.1 Original models

This subsection introduces the original models for the coagulation cascade, of both the extrinsic and intrinsic pathways. The extrinsic model, which is initiated by the presence of tissue factor (TF), is critical for the rapid response to injury. Table 3.3 lists the initial concentrations of clotting factors, based on the work by [5], while Table 3.4 outlines the chemical reactions that define this pathway. On the other hand, the intrinsic pathway, which can be triggered by contact activation and is important for amplifying the coagulation process, is detailed similarly in Table 3.5 and 3.6 for initial concentrations and reactions scheme respectively.

Table 3.3:: The concentration of factors in the original model of extrinsic pathway [5]. The other initial concentrations are set to 0.

Factor	VII	$VIIa$	X	IX	II	$VIII$	V	$TFPI$	$ATIII$	TF
Concentration (nM)	6.67	0.0667	106.67	60.0	933.0	0.4667	13.33	1.667	2267.0	0.001

3.6.2 Reduced models

As final results of this study, reduced models are proposed to approximate the coagulation models in Section 3.6.1 while retaining key dynamic behaviors. This section contains tables that describe reduced versions of both the extrinsic and intrinsic pathway models. For the extrinsic pathway, Table 3.7 displays key initial concentrations (concentrations of which is not 0 at time t = 0). Table 3.7 also provides details on the lumped species and their combinations and information about the QSS species as well. Table 3.8 details the kinetics of the reduced extrinsic pathway. Additionally, conservation relations applied to the reduced model are documented in Table 3.9. For the intrinsic pathway, Table 3.10 lists the initial concentrations, lumped species and QSS species, the kinetics is detailed in Table 3.11 and complemented by Table 3.12, where conservation relations are outlined.

Table 3.4:: Chemical scheme defining the original model of extrinsic pathway [5].

No.	Reaction	k_1	k_{-1}	k_{cat}
1	$TF + VII \longleftrightarrow TF{=}VII$	$3.2 \times 10^6\ M^{-1}s^{-1}$	$3.1 \times 10^{-3}\ s^{-1}$	
2	$TF + VIIa \longleftrightarrow TF{=}IIa$	$2.3 \times 10^7\ M^{-1}s^{-1}$	$3.1 \times 10^{-3}\ s^{-1}$	
3	$TF{=}VIIa + VII \longrightarrow TF{=}VIIa + VIIa$	$4.4 \times 10^5\ M^{-1}s^{-1}$		
4	$Xa + VII \longrightarrow Xa + VIIa$	$1.3 \times 10^7\ M^{-1}s^{-1}$		
5	$IIa + VII \longrightarrow IIa + VIIa$	$2.3 \times 10^4\ M^{-1}s^{-1}$		
6	$TF{=}VIIa + X \longleftrightarrow TF{=}VIIa{=}X \longrightarrow TFVIIa{=}Xa$	$2.5 \times 10^7\ M^{-1}s^{-1}$	$1.1\ s^{-1}$	$6.0\ s^{-1}$
7	$TF{=}VIIa + Xa \longleftrightarrow TF = VIIa{=}Xa$	$2.2 \times 10^7\ M^{-1}s^{-1}$	$19.0\ s^{-1}$	
8	$TF{=}VIIa + IX \longleftrightarrow TF{=}VIIa{=}IX \longrightarrow TF{=}VIIa + IXa$	$1.0 \times 10^7\ M^{-1}s^{-1}$	$2.4\ s^{-1}$	$1.8\ s^{-1}$
9	$II + Xa \longrightarrow IIa + Xa$	$7.5 \times 10^3\ M^{-1}s^{-1}$		
10	$IIa + VIII \longrightarrow IIa + VIIIa$	$2.0 \times 10^7\ M^{-1}s^{-1}$		
11	$VIIIa + IXa \longleftrightarrow IXa{=}VIIIa$	$1.0 \times 10^7\ M^{-1}s^{-1}\ s^{-1}$	5.0×10^{-3}	
12	$IXa{=}VIIIa + X \longleftrightarrow IXa{=}VIIIa{=}X \longrightarrow IXa{=}VIIIa + Xa$	$1.0 \times 10^8\ M^{-1}s^{-1}$	$1 \times 10^{-3}\ s^{-1}$	$8.2\ s^{-1}$
13	$VIIIa \longleftrightarrow VIIIa_1 + VIIIa_2$	$6.0 \times 10^{-3}\ s^{-1}$	$2.2 \times 10^4\ s^{-1}$	
14	$IXa{=}VIIIa{=}X \longrightarrow IXa + X + VIIIa_1 + VIIIa_2$	$1.0 \times 10^{-3}\ s^{-1}$		
15	$IXa{=}VIIIa \longrightarrow IXa + VIIIa_1 + VIIIa_2$	$1.0 \times 10^{-3}\ s^{-1}$		
16	$IIa + V \longrightarrow IIa + Va$	$2.0 \times 10^7\ M^{-1}s^{-1}$		
17	$Xa + Va \longleftrightarrow Xa{=}Va$	$4.0 \times 10^8\ M^{-1}s^{-1}$	$0.2\ s^{-1}$	
18	$Xa{=}Va + II \longleftrightarrow Xa{=}Va{=}II \longrightarrow Xa{=}Va + mIIa$	$1.0 \times 10^8\ M^{-1}s^{-1}$	$103.0\ s^{-1}$	$63.5\ s^{-1}$
19	$Xa{=}Va + mIIa \longrightarrow Xa{=}Va + IIa$	$1.5 \times 10^7\ M^{-1}s^{-1}$		
20	$Xa + TFPI \longleftrightarrow Xa{=}TFPI$	$9.0 \times 10^5\ M^{-1}s^{-1}\ s^{-1}$	$3.6 \times 10^{-4}\ s^{-1}$	
21	$TF{=}VIIa{=}Xa + TFPI \longleftrightarrow TF{=}VIIa{=}Xa{=}TFPI$	$3.2 \times 10^8\ M^{-1}s^{-1}\ s^{-1}$	$1.1 \times 10^{-4}\ s^{-1}$	
22	$TF{=}VIIa{=}Xa + TFPI \longrightarrow TF{=}VIIa{=}Xa{=}TFPI$	$5.0 \times 10^7\ M^{-1}s^{-1}$		
23	$Xa + ATIII \longrightarrow Xa{=}ATIII$	$1.5 \times 10^3\ M^{-1}s^{-1}$		
24	$mIIa + ATIII \longrightarrow mIIa{=}ATIII$	$7.1 \times 10^3\ M^{-1}s^{-1}$		
25	$IXa + ATIII \longrightarrow IXa{=}ATIII$	$4.9 \times 10^2\ M^{-1}s^{-1}$		
26	$IIa + ATIII \longrightarrow IIa{=}ATIII$	$7.1 \times 10^3\ M^{-1}s^{-1}$		
27	$TF{=}VIIa + ATIII \longrightarrow TF{=}VIIa{=}ATIII$	$2.3 \times 10^2\ M^{-1}s^{-1}$		
28	$IXa + X \longleftrightarrow IXa{=}X \longrightarrow IXa + Xa$	$1.0 \times 10^6\ M^{-1}s^{-1}$	$0.5s^{-1}$	$5.0 \times 10^{-4}\ s^{-1}$

Table 3.5:: The concentration of factors in the original model of intrinsic pathway [5]. The other initial concentrations are set to 0.

Factor	VII	$VIIa$	X	IX	II	$VIII$	V	$TFPI$	$ATIII$	XII
Concentration (nM)	6.67	0.0667	106.67	60.0	933.0	0.4667	13.33	1.667	2267.0	226.7
Factor	PK	C_{1NH}	α_{AT}	α_{AP}	XI					
Concentration (nM)	300.0	1667.0	30000.0	667.0	20.67					

Table 3.6:: Chemical scheme defining the original model of intrinsic pathway [5].

No.	Reaction	k_1	k_{-1}	k_{cat}
1	$TF + VII \longleftrightarrow TF{=}VII$	3.2×10^6 $M^{-1}s^{-1}$	3.1×10^{-3} s^{-1}	
2	$TF + VIIa \longleftrightarrow TF{=}VIIa$	2.3×10^7 $M^{-1}s^{-1}$	3.1×10^{-3} s^{-1}	
3	$TF{=}VIIa + VII \longrightarrow TF{=}VIIa + VIIa$	4.4×10^5 $M^{-1}s^{-1}$		
4	$Xa + VII \longrightarrow Xa + VIIa$	1.3×10^7 $M^{-1}s^{-1}$		
5	$IIa + VII \longrightarrow IIa + VIIa$	2.3×10^4 $M^{-1}s^{-1}$		
6	$TF{=}VIIa + X \longleftrightarrow TF{=}VIIa{=}X \longrightarrow TF{=}VIIa{=}Xa$	2.5×10^7 $M^{-1}s^{-1}$	1.1 s^{-1}	6.0 s^{-1}
7	$TF{=}VIIa + Xa \longleftrightarrow TF{=}VIIa{=}Xa$	2.2×10^7 $M^{-1}s^{-1}$	19.0 s^{-1}	
8	$TF{=}VIIa + IX \longleftrightarrow TF{=}VIIa{=}IX \longrightarrow TF{=}VIIa + IXa$	1.0×10^7 $M^{-1}s^{-1}$	2.4 s^{-1}	1.8 s^{-1}
9	$II + Xa \longrightarrow IIa + Xa$	7.5×10^3 $M^{-1}s^{-1}$		
10	$IIa + VIII \longrightarrow IIa + VIIIa$	2.0×10^7 $M^{-1}s^{-1}$		
11	$VIIIa + IXa \longleftrightarrow IXa{=}VIIIa$	1.0×10^7 $M^{-1}s^{-1}$	5.0×10^{-3}	
12	$IXa{=}VIIIa + X \longleftrightarrow IXa{=}VIIIa{=}X \longrightarrow IXa{=}VIIIa + Xa$	1.0×10^8 $M^{-1}s^{-1}$	1.0×10^{-3} s^{-1}	8.2 s^{-1}
13	$VIIIa \longleftrightarrow VIIIa_1 + VIIIa_2$	6.0×10^{-3} s^{-1}	2.2×10^4 s^{-1}	
14	$IXa{=}VIIIa{=}X \longrightarrow IXa + X + VIIIa_1 + VIIIa_2$	1.0×10^{-3} s^{-1}		
15	$IXa{=}VIIIa \longrightarrow IXa + VIIIa_1 + VIIIa_2$	1.0×10^{-3} s^{-1}		
16	$IIa + V \longrightarrow IIa + Va$	2.0×10^7 $M^{-1}s^{-1}$		
17	$Xa + Va \longleftrightarrow Xa{=}Va$	4.0×10^8 $M^{-1}s^{-1}$	0.2 s^{-1}	
18	$Xa{=}Va + II \longleftrightarrow Xa{=}Va{=}II \longrightarrow Xa{=}Va + mIIa$	1.0×10^8 $M^{-1}s^{-1}$	103.0 s^{-1}	63.5 s^{-1}
19	$Xa{=}Va + mIIa \longrightarrow Xa{=}Va + IIa$	1.5×10^7 $M^{-1}s^{-1}$		
20	$Xa + TFPI \longleftrightarrow Xa{=}TFPI$	9.0×10^5 $M^{-1}s^{-1}$	3.6×10^{-4} s^{-1}	
21	$TF{=}VIIa{=}Xa + TFPI \longleftrightarrow TF{=}VIIa{=}Xa{=}TFPI$	3.2×10^8 $M^{-1}s^{-1}$	1.1×10^{-4} s^{-1}	
22	$TF{=}VIIa{=}Xa + TFPI \longrightarrow TF{=}VIIa{=}Xa{=}TFPI$	5.0×10^7 $M^{-1}s^{-1}$		
23	$Xa + ATIII \longrightarrow Xa{=}ATIII$	1.5×10^3 $M^{-1}s^{-1}$		
24	$mIIa + ATIII \longrightarrow mIIa{=}ATIII$	7.1×10^3 $M^{-1}s^{-1}$		
25	$IXa + ATIII \longrightarrow IXa{=}ATIII$	4.9×10^2 $M^{-1}s^{-1}$		
26	$IIa + ATIII \longrightarrow IIa{=}ATIII$	7.1×10^3 $M^{-1}s^{-1}$		
27	$TF{=}VIIa + ATIII \longrightarrow TF{=}VIIa{=}ATIII$	2.3×10^2 $M^{-1}s^{-1}$		
28	$BocVPRMCA + IIa \longleftrightarrow BocVPRMCA{=}IIa \longrightarrow BocVPR + AMC + IIa$	1.0×10^8 $M^{-1}s^{-1}$	6.1×10^3 s^{-1}	53.8 s^{-1}
29	$XII \longrightarrow XIIa$	5.0×10^{-3} M		
30	$XIIa + XII \longleftrightarrow XIIa{=}XII \longrightarrow XIIa + XIIa$	1.0×10^8 $M^{-1}s^{-1}$	750.0 s^{-1}	3.3×10^{-2} s^{-1}
31	$XIIa + PK \longleftrightarrow XIIa{=}PK \longrightarrow XIIa + K$	1.0×10^8 $M^{-1}s^{-1}$	3.6×10^3 s^{-1}	40.0 s^{-1}
32	$XII + K \longleftrightarrow XII{=}K \longrightarrow XIIa + K$	1.0×10^8 $M^{-1}s^{-1}$	45.3 s^{-1}	5.7 s^{-1}
33	$PK + K \longrightarrow K + K$	2.7×10^4 $M^{-1}s^{-1}$		
34	$K \longrightarrow Kinhibited$	1.1×10^{-2} s^{-1}		
35	$XIIa + C_1inh \longrightarrow XIIa{=}C_1inh$	3.6×10^3 $M^{-1}s^{-1}$		
36	$XIIa + ATIII \longrightarrow XIIa{=}ATIII$	21.6 $M^{-1}s^{-1}$		
37	$XI + IIa \longleftrightarrow XI{=}IIa \longrightarrow XIa + IIa$	1.0×10^8 $M^{-1}s^{-1}$	5.0 s^{-1}	1.3×10^{-4} s^{-1}
38	$XIIa + XI \longleftrightarrow XIIa{=}XI \longrightarrow XIIa + XIa$	7.0×10^8 $M^{-1}s^{-1}$	200.0 s^{-1}	2.0×10^{-3} s^{-1}
39	$XIa + XI \longleftrightarrow XIa{=}XI \longrightarrow XIa + XIa$	0.8×10^6 $M^{-1}s^{-1}$		
40	$XIa + ATIII \longrightarrow XIa{=}ATIII$	3.2×10^2 $M^{-1}s^{-1}$		
41	$XIa + C_1inh \longrightarrow XIa{=}C_1inh$	1.8×10^3 $M^{-1}s^{-1}$		
42	$XIa + \alpha_1AT \longrightarrow XIa{=}\alpha_1AT$	1.0×10^2 $M^{-1}s^{-1}$		
43	$XIa + \alpha_2AP \longrightarrow XIa{=}\alpha_2AP$	4.3×10^3 $M^{-1}s^{-1}$		
44	$XIa + IX \longleftrightarrow XIa{=}IX \longrightarrow XIa + IXa$	1.0×10^8 $M^{-1}s^{-1}$	41.0 s^{-1}	7.7 s^{-1}
45	$IXa + X \longleftrightarrow IXa{=}X \longrightarrow IXa + Xa$	1.0×10^5 $M^{-1}s^{-1}$	$2.6 \times 10^{-1}s^{-1}$	6.7×10^{-4} s^{-1}
46	$Xa + VIII \longleftrightarrow Xa{=}VIII \longrightarrow Xa + VIIIa$	1.0×10^8 $M^{-1}s^{-1}$	2.1 s^{-1}	$2.3 \times 10^{-2}s^{-1}$

Table 3.7:: Details of species in the reduced model of extrinsic pathway including one QSS species and two lumped species. This table displays the initial concentrations of the key species. The other initial concentrations are set to 0.

Name of species	Concentration (nM)	Type of species
X	106.67	
IX	60.0	
II	933.0	
$VIII$	0.4667	
V	13.33	
$TFPI$	1.667	
$ATIII$	2267.0	
$L1$	0.0	Lumped species: $TF = VIIa = IX$, $TF = VIIa = X$ and $TF = VIIa = Xa$
$L2$	0.0	Lumped species: $VIIIa1$ and $VIIIa2$
$QSS1$	0.0	QSS Species: $Xa = ATIII$

Table 3.8:: Reactions in the reduced model of extrinsic pathway including one QSS species and two lumped species.

No.	Reaction	k_1	k_{-1}	k_{cat}
1	TF=VIIa + X $\longrightarrow$ L_1 $\longrightarrow$ TF=VIIa$^+$Xa	2.5×10^7 $M^{-1}s^{-1}$	3.6 s^{-1}	
2	TF=VIIa + IX $\longleftrightarrow$ L_1 $\longrightarrow$ TF=VIIa + IXa	1.0×10^7 $M^{-1}s^{-1}$	0.5 s^{-1}	0.4 s^{-1}
3	II + Xa $\longrightarrow$ IIa + Xa	7.5×10^3 $M^{-1}s^{-1}$		
4	IIa + VIII $\longrightarrow$ IIa + VIIIa	2.0×10^7 $M^{-1}s^{-1}$		
5	VIIIa + IXa $\longrightarrow$ IXa=VIIIa	1.0×10^7 $M^{-1}s^{-1}$		
6	IXa=VIIIa + X $\longrightarrow$ IXa=VIIIa=X	1.0×10^7 $M^{-1}s^{-1}$		
7	IXa=VIIIa=X $\longrightarrow$ IXa=VIIIa + Xa	1.0×10^7 $M^{-1}s^{-1}$		
8	VIIIa $\longrightarrow$ $L_2 + L_2$	6.0×10^{-3} s^{-1}		
9	IIa + V $\longrightarrow$ IIa + Va	2.0×10^7 $M^{-1}s^{-1}$		
10	Xa + Va $\longleftrightarrow$ Xa=Va	4.0×10^8 $M^{-1}s^{-1}$	0.2 $M^{-1}s^{-1}$	
11	Xa=Va + II $\longleftrightarrow$ Xa=Va=II $\longrightarrow$ Xa=Va + mIIa	1.0×10^8 $M^{-1}s^{-1}$	103.0 s^{-1}	63.5 s^{-1}
12	Xa=Va + mIIa $\longrightarrow$ Xa=Va + IIa	1.5×10^7 $M^{-1}s^{-1}$		
13	L_1 + TFPI $\longrightarrow$ TF=VIIa=Xa=TFPI	6.0×10^7 $M^{-1}s^{-1}$		
14	mIIa + ATIII $\longrightarrow$ mIIa=ATIII	7.1×10^3 $M^{-1}s^{-1}$		
15	IXa + ATIII $\longrightarrow$ IXa=ATIII	4.9×10^2 $M^{-1}s^{-1}$		
16	IIa + ATIII $\longrightarrow$ IIa=ATIII	7.1×10^3 $M^{-1}s^{-1}$		

Table 3.9:: Conservation relations in reduced model of extrinsic pathway

#	Equation
1	$[TF = VIIa = Xa = TFPI] + [TF = VIIa] + [L_1] = 0.001$
2	$[IIa] + [II] + [Xa = Va = II] + [IIa = ATIII] + [mIIa] + [mIIa = ATIII] = 933.0$
3	$[Xa = Va] + [Va] + [Xa = Va = II] + [V] = 13.33$

Table 3.10:: Details of species in the reduced intrinsic pathway model including four QSS species and six lumped species. This table displays the initial concentrations of the key species. The other initial concentrations are set to 0.

Factor	Concentration (nM)	Description
X	106.67	
IX	60.0	
II	933.0	
$VIII$	0.4667	
V	13.33	
$ATIII$	2267.0	
$L1$	0.0	$VIIIa1$ and $VIIIa2$
$L2$	0.0	AMC and $BocVPR$
$L3$	226.7	lumped species: XII and $XII = K$
$L4$	20.67	lumped species: $XIIa = XI$ and XI
$L5$	0.0	lumped species: $XIa = \alpha 1AT$, $XIa = \alpha 2AT$ and $XIa = C1inh$
$L6$	2334.0	lumped species: $\alpha 2AT$ and $C1inh$
$QSS1$	0.0	QSS Species: $mIIa = ATIII$
$QSS2$	0.0	QSS Species: $IIa = ATIII$
$QSS3$	300.0	QSS Species: PK
$QSS4$	30000.0	QSS Species: $\alpha 1AT$

Table 3.11:: Reactions in the reduced intrinsic pathway model including four QSS species and six lumped species.

No.	Reaction	k_1	k_{-1}	k_{cat}
1	$\mathrm{II} + \mathrm{Xa} \longrightarrow \mathrm{IIa} + \mathrm{Xa}$	7.5×10^3 $\mathrm{M^{-1}s^{-1}}$		
2	$\mathrm{IIa} + \mathrm{VIII} \longrightarrow \mathrm{IIa} + \mathrm{VIIIa}$	2.0×10^7 $\mathrm{M^{-1}s^{-1}}$		
3	$\mathrm{VIIIa} + \mathrm{IXa} \longleftrightarrow \mathrm{IXa{=}VIIIa}$	1.0×10^7 $\mathrm{M^{-1}s^{-1}}$	5.0×10^{-3} $\mathrm{s^{-1}}$	
4	$\mathrm{IXa{=}VIIIa} + \mathrm{X} \longrightarrow \mathrm{IXa{=}VIIIa{=}X}$	1.6×10^8 $\mathrm{M^{-1}s^{-1}}$		
5	$\mathrm{IXa{=}VIIIa{=}X} \longrightarrow \mathrm{IXa{=}VIIIa} + \mathrm{Xa}$	29.0 $\mathrm{M^{-1}s^{-1}}$		
6	$\mathrm{IXa{=}VIIIa} \longrightarrow \mathrm{IXa} + \mathrm{L_1} + \mathrm{L_1}$	1.0×10^{-3} $\mathrm{s^{-1}}$		
7	$\mathrm{IIa} + \mathrm{V} \longrightarrow \mathrm{IIa} + \mathrm{Va}$	2.0×10^7 $\mathrm{M^{-1}s^{-1}}$		
8	$\mathrm{Xa} + \mathrm{Va} \longleftrightarrow \mathrm{Xa{=}Va}$	4.0×10^8 $\mathrm{M^{-1}s^{-1}}$	0.2 $\mathrm{s^{-1}}$	
9	$\mathrm{Xa{=}Va} + \mathrm{II} \longleftrightarrow \mathrm{Xa{=}Va{=}II} \longrightarrow \mathrm{Xa{=}Va} + \mathrm{mIIa}$	1.0×10^8 $\mathrm{M^{-1}s^{-1}}$	103.0 $\mathrm{s^{-1}}$	63.5 $\mathrm{s^{-1}}$
10	$\mathrm{Xa{=}Va} + \mathrm{mIIa} \longrightarrow \mathrm{Xa{=}Va} + \mathrm{IIa}$	1.5×10^7 $\mathrm{M^{-1}s^{-1}}$		
11	$\mathrm{Xa} + \mathrm{ATIII} \longrightarrow \mathrm{Xa{=}ATIII}$	1.5×10^3 $\mathrm{M^{-1}s^{-1}}$		
12	$\mathrm{mIIa} + \mathrm{ATIII} \longrightarrow \mathrm{QSS_4}$	7.1×10^3 $\mathrm{M^{-1}s^{-1}}$		
13	$\mathrm{IIa} + \mathrm{ATIII} \longrightarrow \mathrm{QSS_3}$	7.1×10^3 $\mathrm{M^{-1}s^{-1}}$		
14	$\mathrm{BocVPRMCA} + \mathrm{IIa} \longleftrightarrow \mathrm{BocVPRMCAIIa} \longrightarrow \mathrm{L_2} + \mathrm{L_2} + \mathrm{IIa}$	1.0×10^8 $\mathrm{M^{-1}s^{-1}}$	6100.0 $\mathrm{s^{-1}}$	53.8 $\mathrm{s^{-1}}$
15	$\mathrm{L_3} \longrightarrow \mathrm{XIIa}$	3.0×10^{-3} $\mathrm{s^{-1}}$		
16	$\mathrm{XIIa} + \mathrm{QSS_1} \longrightarrow \mathrm{XIIa{=}PK}$	1.0×10^8 $\mathrm{M^{-1}s^{-1}}$		
17	$\mathrm{XIIa{=}PK} \longrightarrow \mathrm{XIIa} + \mathrm{K}$	40.0 $\mathrm{M^{-1}s^{-1}}$		
18	$\mathrm{L_3} + \mathrm{K} \longleftrightarrow \mathrm{L_3} \longrightarrow \mathrm{XIIa} + \mathrm{K}$	6.2×10^6 $\mathrm{M^{-1}s^{-1}}$	17.2 $\mathrm{s^{-1}}$	2.2 $\mathrm{s^{-1}}$
19	$\mathrm{XIIa} + \mathrm{L_4} \longleftrightarrow \mathrm{L_4} \longrightarrow \mathrm{XIIa} + \mathrm{XIa}$	4.0×10^6 $\mathrm{M^{-1}s^{-1}}$	87.3 $\mathrm{s^{-1}}$	8.7×10^{-4} $\mathrm{s^{-1}}$
20	$\mathrm{XIa} + \mathrm{L_4} \longrightarrow \mathrm{XIa} + \mathrm{XIa}$	4.5×10^5 $\mathrm{M^{-1}}$ $\mathrm{s^{-1}}$		
21	$\mathrm{XIa} + \mathrm{QSS_2} \longrightarrow \mathrm{l_5}$	1.0×10^2 $\mathrm{M^{-1}s^{-1}}$		
22	$\mathrm{XIa} + \mathrm{L_6} \longrightarrow \mathrm{L_5}$	1.3×10^3 $\mathrm{M^{-1}s^{-1}}$		
23	$\mathrm{XIa} + \mathrm{IX} \longleftrightarrow \mathrm{XIa{=}IX} \longrightarrow \mathrm{XIa} + \mathrm{IXa}$	1.0×10^8 $\mathrm{M^{-1}s^{-1}}$	41.0 $\mathrm{s^{-1}}$	7.7 $\mathrm{s^{-1}}$
24	$\mathrm{IXa} + \mathrm{X} \longleftrightarrow \mathrm{IXa{=}X} \longrightarrow \mathrm{IXa} + \mathrm{Xa}$	1.0×10^5 $\mathrm{M^{-1}s^{-1}}$	2.6×10^{-1} $\mathrm{s^{-1}}$	6.7×10^{-4} $\mathrm{s^{-1}}$
25	$\mathrm{Xa} + \mathrm{VIII} \longleftrightarrow \mathrm{Xa{=}VIII} \longrightarrow \mathrm{Xa} + \mathrm{VIIIa}$	1.0×10^8 $\mathrm{M^{-1}s^{-1}}$	2.1 $\mathrm{s^{-1}}$	2.3×10^{-2} $\mathrm{s^{-1}}$

Table 3.12:: Conservation relations in reduced model of intrinsic pathway

No.	Equation
1	$[V] + [Va] + [Xa = Va] + [Xa = Va = II] = 13.3$
2	$[XIa] + [l3] + [XIa = IX] = 20.67$
3	$[X] + [IXa = X] + = 106.67$
4	$[VIII] + [Xa = VIII] = 0.467$

Chapter 4

A simplified computational model of coagulation cascade in venous valves

Abstract

The previous chapters have has explored optimization and model reduction based on thrombin generation assays (TGA). In this chapter, the analysis is extended to an open system by developing a simplified 0-D model designed to assess the risk of thrombosis in venous valves. The complex hemodynamic characteristics of venous valve regions derived from 3D simulations have been simplified into a single mass transfer coefficient k_{flow}, and integrated into two distinct coagulation models: one including platelets and another focusing solely on plasma-based reactions. The study investigates the impact of these simplified hemodynamics on thrombin generation under various stimulus conditions, relevant to deep vein thrombosis (DVT). Results reveal that the mechanical behavior of venous valves and the presence or absence of platelets significantly affect the thrombin generation process. This research addresses the critical question of how venous hemodynamics, in combination with biochemical interactions, contribute to DVT.

4.1 Introduction

DVT is a condition characterized by the formation of blood clots in the deep veins. Specifically, the thrombus is primarily likely to locate in the venous valve sinus. It is a major public health concern due to its association with severe complications. If a part of the thrombus dislodges and travels to the lungs, it can result in pulmonary embolism (PE), a life-threatening complication [126, 127]. The medical significance of DVT lies in its high morbidity and mortality rates, particularly among hospitalized patients, postoperative individuals, and those with underlying conditions such as cancer or thrombophilia, as these populations are at an increased risk of thrombus formation and subsequent embolization [128]. Anticoagulant therapy remains the primary treatment strategy for DVT and specific treatment plans vary depending on the situation [129]. Therefore, it is necessary to improve modeling frameworks to enhance risk assessment and personalized treatment strategies.

Hemodynamics plays a crucial role in DVT pathogenesis, particularly in venous valves where stasis can promote coagulation. As shown in Figure 4.1, the valves regulate blood flow direction by opening and closing in response to pressure differentials within the vessel/vein. During the opening phase, a pressure drop across the valve initiates forward flow, forcing the leaflets apart and increasing the orifice size. As the valve reaches equilibrium, the flow stabilizes, creating distinct velocity profiles: high axial velocity in the vessel/vein center and vortex formation within the sinus due to detached streamlines at the leaflet tips. These vortices play a crucial role in mixing and preventing prolonged blood stasis. During the closing phase, a reduction in forward flow and potential retrograde pressure cause the leaflets to move toward each other, gradually reducing the orifice size. Finally, in the fully closed state, the valve leaflets come into contact, preventing retrograde blood flow and ensuring unidirectional circulation. Throughout this process, altered shear rates and turbulence contribute to thrombus initiation and propagation [130].

Moreover, muscle contraction and respiratory-induced venous return influence clot development by modulating local flow conditions [131]. In veins, the skeletal muscle pump is the primary driver of valve dynamics. When the leg muscles contract, they compress the deep veins between themselves and the bones, generating a pressure that enhances blood flow velocity and more effectively flushes the sinus region. In contrast, when a person is at bed rest, the calf muscle pump remains inactive, and blood flow is primarily maintained by the respiratory pump. Under this condition, venous return is significantly slower, leading to prolonged residence times of blood in the valve pockets, which increases the risk of Deep Vein Thrombosis (DVT).

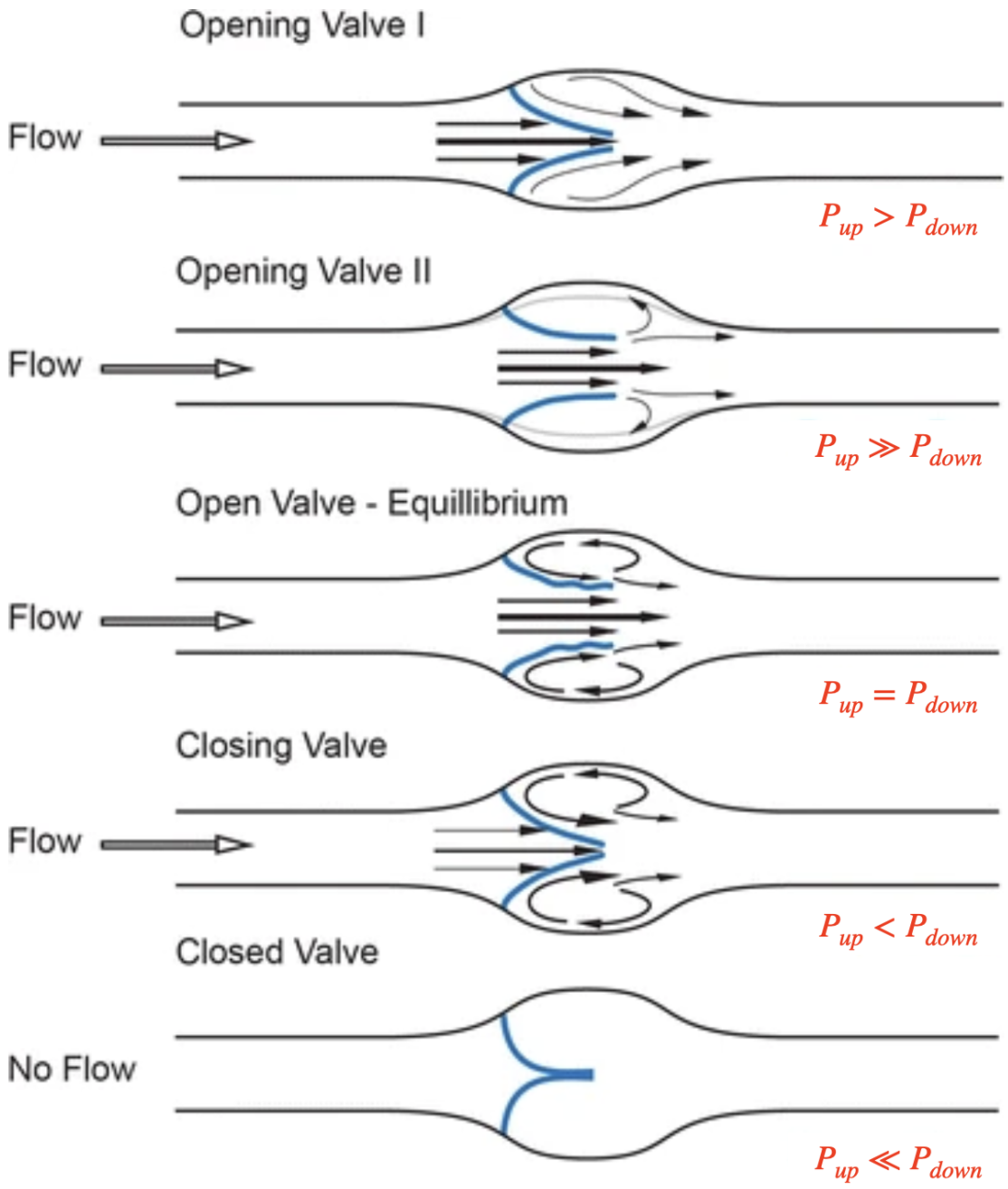

Figure 4.1: The dynamic behavior of venous valve leaflets (blue) follows distinct phases: opening, equilibrium, closing, and fully closed. The pressure drop across the vessel dictates the flow direction (indicated by black hollow arrows), while differential forces on either side of the valve leaflets (P_{up}, P_{down}) regulate their movement and determine the orifice size. Black arrows illustrate key flow patterns and velocity variations within the valve pocket. The gray line represents vessel/vein distension during the valve's opening phase. Adapted from [11].

Simulations provide insights into shear stress distributions, velocity profiles, and residence times, which are critical in understanding how clots initiate and grow in venous circulation. Elizondo et al. [59] used a 0-D model that ignored macro-scale geometry, simplifying computation but overlooking important spatial dynamics and the roles of platelets is misunderstood. In [69, 66], the geometry complexity of venous valves was not considered and the reactions scheme is simple. In all these models, the only factor that emphasizes venous flow is low shear rate, even the flow in venous valves is very complex. In [67], a 2-D sinus-like geometry was used for simulation, even the geometry remained static over time.

Despite advances in CFD-based thrombosis modeling, these models still face several limitations. One major challenge of aforementioned models is the oversimplification of hemodynamics and deformation, where many models assume valves as unmoved solid walls rather than incorporating patient-specific geometries, which are crucial for accurately predicting thrombus formation. The interaction between blood flow and deformable structures is crucial in the case of cardiac or venous valves. Fluid-structure interaction (FSI) methods are naturally suited for these issues.

However, large-scale 3D FSI simulations come with high computational costs, making them difficult for real-time clinical applications. For instance, the 3D simulations performed by Thibaud et al. [13] were executed on 192 computing cores (80 for the solid domain and 112 for the fluid domain) of the ADASTRA HPC cluster at GENCI/CINES. These simulations covered only about 1 second of physical time but required a total runtime ranging from 24 to 36 hours. This high cost also blocks biochemistry coupling with FSI, which hinders the ability to simulate thrombus initiation and progression precisely.

To address these gaps, in this chapter, the 3-D FSI simulations results are simplified to a single representative transport coefficient, allowing for the integration of reaction schemes with fluid profiles. The impacts of stimulus and effect coefficient on thrombin generation are investigated under different types of coagulation schemes. This study enhances the analysing and understandings of the biomechanical and biochemical interactions in valve leaflets.

4.2 Methods and Materials

4.2.1 Mathematical models

A mathematical representation is used to model the dynamics of the chemical species' concentration within a localized reaction zone, as illustrated in Figure 4.2. This model describes the evolution of chemical concentrations within the reaction zone under two key assumptions: (1) the concentrations are spatially homogeneous, effectively treating the zone as a perfectly stirred reactor; (2) mass exchange occurs with the external environment at a rate of k_{flow}. The introduction of this mass exchange term marks a key distinction from the equations discussed in Chapters 2 and 3, where the system was previously assumed to be closed. Here, the model is extended to an open system, allowing for interactions with its surroundings [58].

$$\frac{d\bar{C}_i}{dt} = R_i + k_{flow}(C_i^{up} - \bar{C}_i) \tag{4.1}$$

Eq. (4.1) describes the temporal evolution of the average concentration $\bar{C}_i$ of species i in a reaction zone within the venous system. The term R_i accounts for the biochemical reaction rates. The second term, $k_{flow}(C_i^{up} - \bar{C}_i)$, represents the transport of species into and out of the region due to blood flow, where C_i^{up} is the upstream concentration, and k_{flow} is the mass transfer coefficient governing exchange dynamics. Mass balance of the reaction zone requires:

$$V(t+dt)\bar{C}_i(t+dt) - V(t)\bar{C}_i(t) = Q^+ C_i^{up} dt - Q^- \bar{C}_i dt \tag{4.2}$$

where $V(t)$ is the volume (in m^3) of blood in the zone at time t, and $\bar{C}(t)$ is the average concentration of the species (in mol/m^3). The terms Q^+, and Q^-, denote the inflow and outflow flow rates (in m^3/s) across the boundary between the zone of interest and the rest of the vein respectively (see Figure 4.2). From mass conservation, it is clear that

$$Q^+ = Q^- + \frac{dV}{dt} \tag{4.3}$$

To first order deviation, Eq. (4.2) is equivalent to:

$$\frac{dVC}{dt} = Q^+ C_i^{up} - Q^- \bar{C}_i \tag{4.4}$$

Then inject (4.3) into (4.4), the rate of change of average concentration in reaction zone is:

$$\frac{d\bar{C}_i}{dt} = \frac{Q^+}{V}(C_i^{up} - \bar{C}_i) \tag{4.5}$$

Eq. 4.5 defines the mass transfer in the (bottom) zone of the sinus of venous valves. Then consider the source term of the chemical reaction:

$$\frac{d\bar{C}_i}{dt} = R_i + \frac{Q^+}{V}(C_i^{up} - \bar{C}_i) \tag{4.6}$$

Compare Eq. 4.1 and Eq. 4.8:

$$k_{flow} = \frac{Q^+}{V} \tag{4.7}$$

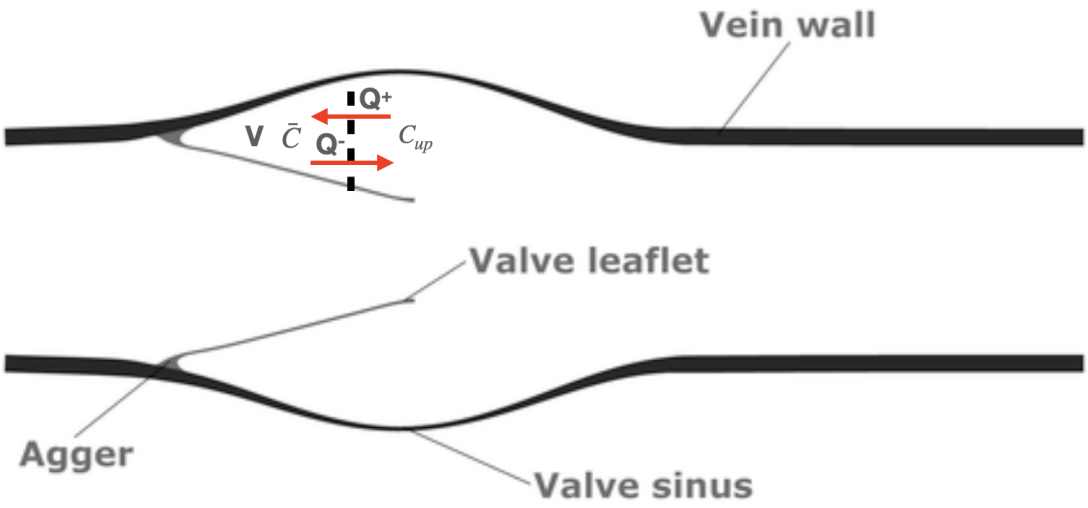

Figure 4.2: Schematic of venous valves with notations used in section 4.2.1. Modified from [12]. Reaction zones of venous leaflets enclosed by the vein walls, leaflets and dashed black lines. V: Represents the volume of blood flow in the venous valve region. Q^+: The inflow rate into the venous valve region. Q^-: The outflow rate from the venous valve region. C^{up}: The concentration of species in the incoming blood flow. $\bar{C}$: The concentration of species in the reaction zone.

These formulas are based on the assumption that the reaction zone is relatively small and well-mixed where spatial gradients are negligible. This simplification allows for a single averaged concentration $\bar{C}_i$ rather than a full spatially dependent reaction-diffusion model. Additionally, venous valves and vein wall motions induce periodic variations in blood flow, which contribute to the homogenization of species concentrations, making the assumption of a well-mixed zone more reasonable.

4.2.2 3D Fluid-Structure Interaction (FSI) Simulation for Venous Valves and mass transfer coefficient k_{flow}

In the studies conducted by Thibaud et al. [13, 132], a three-dimensional model of a venous vein with valves designed based on experimental anatomical observations was simulated under physiologically relevant conditions. Blood was modeled as an incompressible Newtonian fluid governed by the Navier–Stokes equations, while the valve leaflets were treated as deformable hyperelastic solids. The fluid–structure interaction (FSI) simulations were carried out using the YALES2BIO solver suite. A partitioned and body-fitted scheme was employed to couple fluid and solid domains. Interface conditions were imposed using a Dirichlet–Neumann boundary condition, and convergence was accelerated with Aitken method.

Figure 4.3 illustrates the axial velocities of 3D simulations from [13] capturing the flow dynamics at key time points throughout a single cycle. At the start of the cycle (t = 0.01 s, panel a), the valve leaflets are fully closed, effectively preventing retrograde flow. The velocity remains minimal, with low-velocity recirculation zones forming within the sinus region. As forward flow increases (t = 0.1 s, panel b), the valve begins to open, and small regions of increased velocity emerge near the leaflet tips, marking the initial separation of the leaflets. At t = 0.5 s (panel c), the valve reaches its fully open state, allowing maximum axial velocity in the center of the vessel, as indicated by the strong red region. The sinus region exhibits distinct recirculating vortices due to localized flow separation. As the inflow starts to decrease (t = 1.0 s, panel d), the velocity declines, and the valve leaflets gradually move back toward closure, with velocity gradients forming near the closing edges. By t = 1.2 s (panel e), the valve is almost fully closed, and axial velocity drops significantly. The cycle nears completion, and the valve returns to its fully closed state, marking the beginning of a new flow cycle. Figure 4.3 aligns with the valve dynamics described in Figure 4.1.

To assess the influence of the calf muscle pump on venous valve dynamics, the inflow boundary condition was modified to a sinusoidal profile with a peak velocity approximately twice that of the bed-rest configuration. The geometric parameters of the vein model included a valve diameter of 10 mm, a uniform leaflet thickness of 70 μm, a sinus length equal to one valve diameter, and a sinus depth of 1.2 times the vessel radius.

As defined in Figure 4.2, a boundary (dashed line) is needed to enclose the reaction zone. This region is identified as high-risk due to local flow stagnation and biochemical accumulation observed in artificial valve experiments.

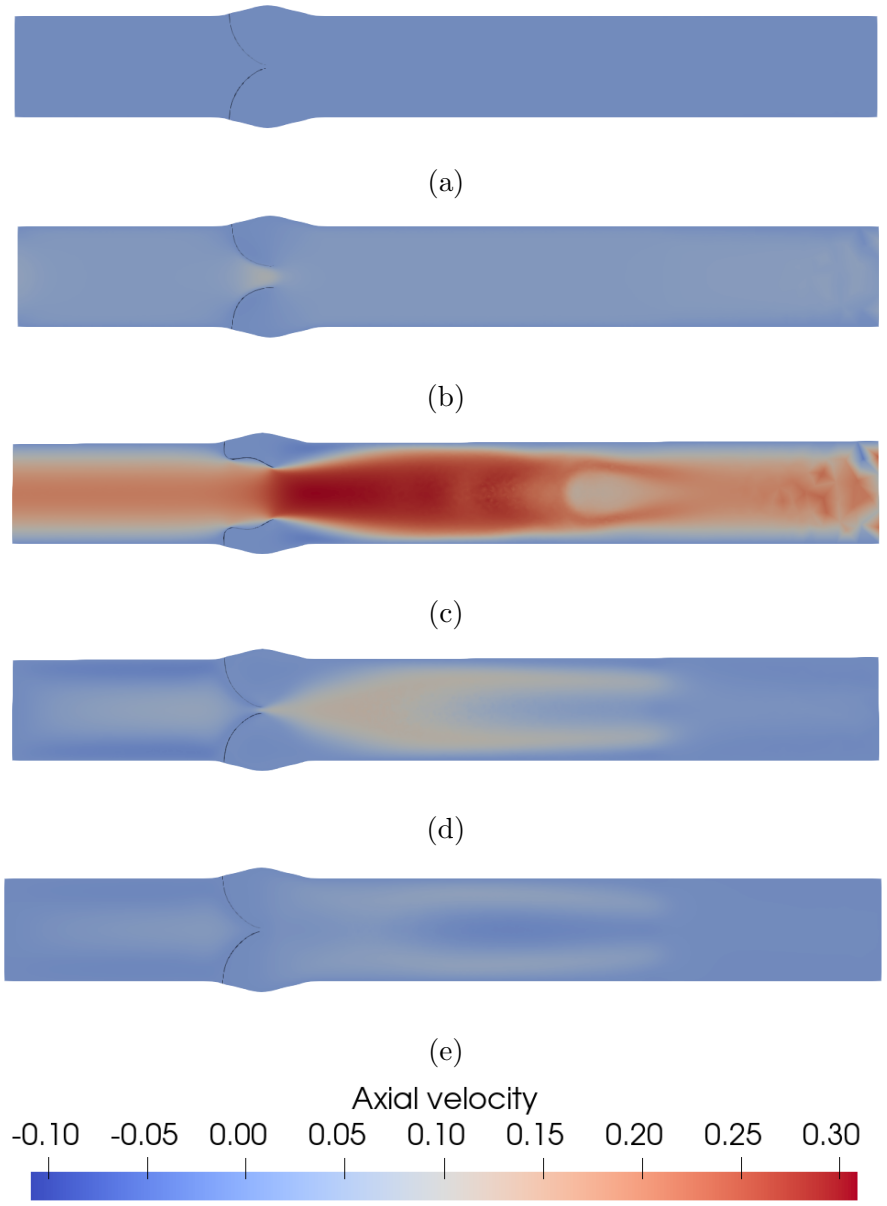

Figure 4.3: Axial velocity distributions at different time points illustrating the venous valve cycle. The snapshots correspond to distinct phases of the cycle: (a) fully closed at t = 0.01 s, (b) early opening at t = 0.1 s, (c) fully open at t = 0.5 s, (d) transition to closure at t = 1 s, and (e) nearly closed at t = 1.2 s. The color scale represents axial velocities, with red indicating high forward flow and blue representing low or reversed flow. This analysis is based on Thibaud's PhD thesis work [13].

The selection of the boundary of reaction zone is based on experimental observations from Figure 4.4a in simulation. According to the observation, thrombus formation is primarily localized from the bottom of the sinus to approximately 25% of its depth in an artificial venous valve system. By setting the boundary at 25% depth, the simulation focuses on the region where clotting is most likely to initiate and progress, as observed in the experiment. If the boundary is placed farther from the sinus, the mass transfer coefficient k_{flow} increases due to a larger exchange surface with the surrounding blood flow. Conversely, selecting a boundary closer to the sinus could decrease the mass transfer coefficient, as almost no flow exist at the extremely bottom.

As in Eq. 4.7, the computation of the mass transfer coefficient k_{flow} requires values for Q^+ and V, which are derived from 3D fluid-structure interaction (FSI) simulations conducted by Thibaud et al. [132, 13]. From these 3D FSI simulations, the inflow rate (Q^+) and local volume (V) were extracted by Paraview to quantify the mass transfer coefficient. Figure 4.4b shows how the boundary defines the control volume in this chapter.

In Figure 4.5, the mass transfer coefficients were measured according to 3-D simulations under theses conditions are exhibited. The reduced flow dynamics during bed rest correspond to a lower mass transfer coefficient k_{flow}, while the dynamics with muscle pump is more intensive. The red curve demonstrates minimal fluctuations in no muscle contraction condition, remaining relatively flat over time. Conversely, the blue curve illustrates the effect of muscle contraction on the dynamic behavior of the venous valves. The coefficient k_{flow} shows larger and periodic peaks.

4.2.3 Mass transfer efficiency α

The mass transfer between the sinus and the outer flow of fresh blood is characterized by the k_{flow} coefficient derived above from mass conservation. Moreover, its numerical values correspond to simplified fluid-structure interactions recently performed by Thibaud et al. [132, 13]. Assuming that the corresponding time evolution displayed in Figure 4.5 can be strongly affected by these modeling choices, a prefactor coefficient α is introduced as in Eq. 4.8 to ease further parametric studies about the effect of the efficiency of the mass transfers on the thrombin dynamics in the sinus region:

$$\frac{d\bar{C}_i}{dt} = R_i + \alpha k_{flow}(C_i^{up} - \bar{C}_i) \tag{4.8}$$

The function of α can be understood in terms of its effect on venous

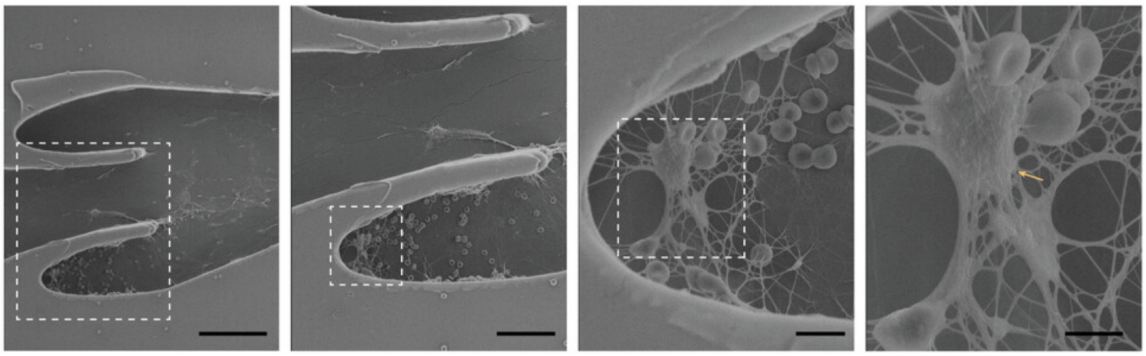

(a)

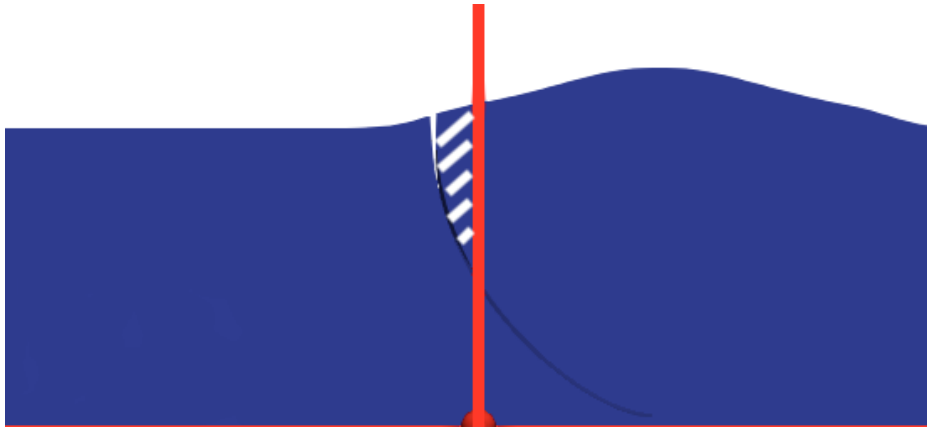

(b)

Figure 4.4: (a) Scanning electron micrographs of various sections (increasing magnification from left to right) of the Vein-Chips after thrombus have formed. thrombus are rich in fibrin and red blood cells, devoid of platelets and contain leukocytes. Scale bars from left to right, 100, 50, 10, and 5 μm. Adapted from [14]. (b) The boundary (red line) of the control volume (hatched area) in Paraview.

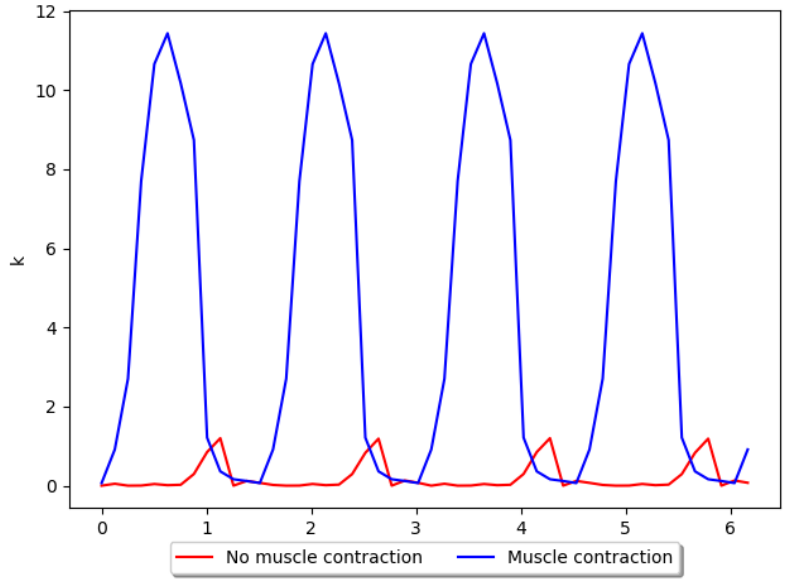

Figure 4.5: The influence of muscle contraction on the parameter k (Computed via Eq. 4.7) over time. The blue curve represents the system with muscle contraction, indicating dynamic oscillations of k_{flow} under blood flow driven by muscle activity. The red curve, representing the system without muscle contraction.

hemodynamics. For example, when $\alpha = 0$, the transport term vanishes mimicking a condition where venous valves lose their normal function. When $\alpha > 0$, the transport mechanism is active, allowing for a controlled inflow and outflow of biochemical species. Greater α values mimick situations where the mass exchange between the inner and outer regions are larger, e.g. because of stronger valve motion.

4.2.4 Chemical schemes

Platelets play a less important role in DVT compared to the arterial system. Unlike arterial thrombi, which are characterized by vast platelet aggregates, venous thrombi lack such structures [133]. Instead, fibrin cross-linking forms large fibrin strands that entangle blood cells, resulting DVT. Consequently, the chemical model excluding platelets and proposed by Butenas et al. [15], as shown in Table 2.1, is used as a first step. On the other hand, activated platelets support coagulation by expressing elevated levels of phosphatidylserine (PS) on their surface, a key marker of platelet activation [134]. However, in the venous system, platelets do not aggregate or adhere to the endothelium. As illustrated in [133], platelet membrane coagulation influences both the tenase complex (comprising factor IXa and cofactor VIIIa) and

the prothrombinase complex (comprising factor Xa and cofactor Va). Consequently, a coagulation model developed by Susree et al. [16] that incorporates the surface binding sites of platelets is employed as an alternative to the model of Butenas et al. [15]. In this model, platelets neither adhere to the endothelium nor aggregate with each other, reflecting the physical principles underlying DVT formation. The scheme is displayed in Tables 4.1 and 4.2, in which AP stands for activated platelets and PL represents inactivated platelets. AP_i represents the competitive biding sites of the coagulation factors on the surface of a platelet. For example, AP_5 stands for number of biding sites of factor V on an activated platelet.

Table 4.1:: Reactions of the coagulation cascade platelets-based model [16].

Reaction	k_1 $(\mathbf{nM^{-1}s^{-1}})$	k_{-1} $(\mathbf{s^{-1}})$	k_{cat} $(\mathbf{s^{-1}})$
$PL + AP \longrightarrow 2\,AP$	0.3		
$PL + IIa \longrightarrow AP + IIa$	0.37		
$TF + VII \longleftrightarrow TF{=}VII$	3.2×10^{-3}	3.1×10^{-3}	
$TF + VIIa \longleftrightarrow TF{=}VIIa$	0.023	3.1×10^{-3}	
$TF{=}VIIa + VII \longrightarrow TF{=}VIIa + VIIa$	4.4×10^{-4}		
$VII + Xa \longrightarrow VIIa + Xa$	0.013		
$VII + IIa \longrightarrow VIIa + IIa$	2.3×10^{-5}		
$TF{=}VIIa + IX \longrightarrow TF{=}VIIa + IXa$	243.0		0.26
$TF{=}VIIa + X \longrightarrow TF{=}VIIa + Xa$	450.0		1.15
$II + Xa \longrightarrow IIa + Xa$	7.5×10^{-6}		
$VIIIa \longrightarrow VIII_i$	3.7×10^{-3}		
$Va \longrightarrow V_i$	2.8×10^{-3}		
$I + IIa \longrightarrow Ia$	3160		59
$IX/IXa + AP_9 \longleftrightarrow IXm/IXam$	0.01	0.0257	
$IXam + VIIIam \longleftrightarrow VIIIam{=}IXam$	0.01	0.005	
$X/Xa + AP_{10} \longleftrightarrow Xm/Xam$	0.029	3.3	
$Xm + VIIIam{=}IXam \longrightarrow Xam + VIIIam{=}IXam$	63		8.33
$Xam + Vam \longleftrightarrow Vam{=}Xam$	0.4	0.2	
$II/IIa + AP_2 \longleftrightarrow IIm/IIam$	0.01	5.9	
$IIm + Xam{=}Vam \longrightarrow IIam + Xam{=}Vam$	1060		22.4
$VIII/VIIIa + AP_8 \longleftrightarrow VIIIm/VIIIam$	4.3×10^{-3}	2.1×10^{-3}	
$VIIIm + IIam \longrightarrow VIIIm + IIam$	200		0.9

Table 4.1:: (continued)

Reaction	k_1 $(\mathbf{nM^{-1}s^{-1}})$	k_{-1} $(\mathbf{s^{-1}})$	k_{cat} $(\mathbf{s^{-1}})$
$\mathrm{VIIIm} + \mathrm{Xam} \longrightarrow \mathrm{VIIIm} + \mathrm{Xam}$	20		0.023
$\mathrm{V/Va} + \mathrm{AP_5} \longleftrightarrow \mathrm{Vm/Vam}$	0.057	0.17	
$\mathrm{Vm} + \mathrm{IIam} \longrightarrow \mathrm{Vm} + \mathrm{IIam}$	71.7		0.23
$\mathrm{Vm} + \mathrm{Xam} \longrightarrow \mathrm{Vm} + \mathrm{Xam}$	10.4		0.046
$\mathrm{ATIII} + \mathrm{Xa} \longrightarrow \mathrm{ATIII} + \mathrm{X}_i$	3.06×10^{-6}		
$\mathrm{ATIII} + \mathrm{IXa} \longrightarrow \mathrm{ATIII} + \mathrm{IX}_i$	2.22×10^{-4}		
$\mathrm{ATIII} + \mathrm{IIa} \longrightarrow \mathrm{ATIII} + \mathrm{II}_i$	1.79×10^{-4}		
$\mathrm{ATIII} + \mathrm{TF{=}VIIa} \longrightarrow \mathrm{ATIII} + \mathrm{TF{=}VII}_i$	4.5×10^{-8}		
$\mathrm{TFPI} + \mathrm{Xa} \longleftrightarrow \mathrm{Xa{=}TFPI}$	4.381	5.923×10^{-8}	
$\mathrm{Xa{=}TFPI} + \mathrm{TF{=}VIIa} \longleftrightarrow \mathrm{Xa{=}TFPI} + \mathrm{TF{=}VIIi}$	0.05		

Table 4.2:: Concentration of coagulation factors, platelets and the number of biding sites in the platelets-based model. The binding sites are listed as the count on per activated platelet [16].

Clotting Factors (nM)									
ATIII	I	II	IX	TF	TFPI	VII	VIII	V	X
3400	7000	1400	90	0.025	2.5	10	0.7	20	170
Platelets and the binding sites.									
PL			P2	P5	P8	P9	P9a		
0.415 nM ($2.5 \times 10^5/\mu l$)			2000	2700	750	250	550		

4.3 Results

4.3.1 Thrombin generation in venous valves

Using the platelets-free model

The thrombin generation in Figure 4.6 illustrates the differences between scenarios with and without muscle contraction using the platelet-free model under three conditions: (i) no inhibitors (Both the initial concentrations of ATIII and TFPI were set to 0), (ii) ATIII inhibition only (The initial concentration of TFPI was set to 0.), and (iii) both ATIII and TFPI inhibition. Notably, the results show negligible differences among these three conditions, suggesting that the strong mass transfer effect dominates the system. In Figure 4.6a, muscle contraction introduces cyclic flow conditions that lead to oscillatory thrombin dynamics, reflecting periodic increases and decreases in thrombin concentration. In contrast, Figure 4.6b shows thrombin dynamics without muscle contraction, where thrombin steadily oscillate around 0 nM similarly. This indicates no significant risk of clot formation, as 2 nM thrombin appears to be an threshold concentration to initiate fibrin clot formation in a flowing system [135].

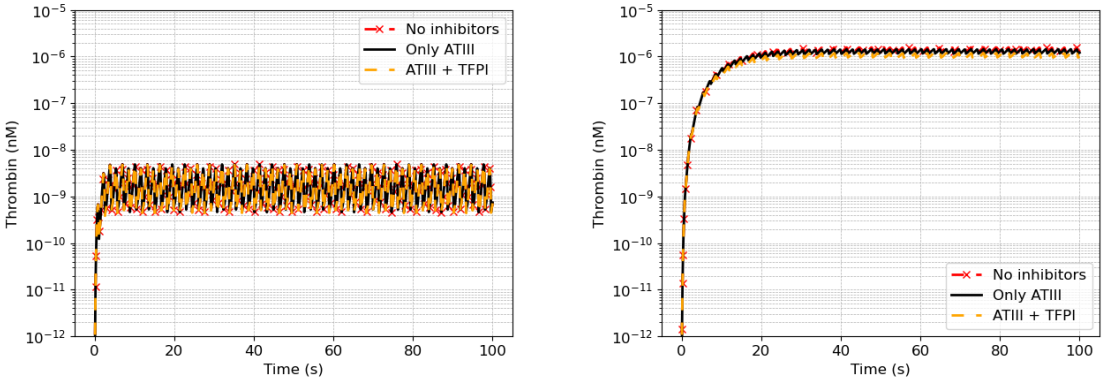

Figure 4.6: Comparison of thrombin generation with and without muscle contraction using the no-platelets model in Table 2.1. (a) Thrombin generation dynamics under the influence of muscle contraction. (b) Thrombin generation dynamics without muscle contraction.

Using the platelets-based model

The results in Figure 4.7 illustrate the dynamics of thrombin generation and platelet activation under conditions with and without muscle contraction using the platelets-based model. Figure 4.7a represents thrombin generation without muscle contraction. In the absence of inhibitors, thrombin levels rapidly reach peak at approximately 1400 nM within 180 s, indicating an unregulated coagulation process. With ATIII alone, the peak thrombin levels are significantly reduced to around 300 nM, occurring at approximately 300 seconds. The combination of ATIII and TFPI further significantly delays thrombin generation.

In contrast, Figure 4.7c illustrates thrombin generation in the presence of muscle contraction. Compared to the no-contraction case, thrombin initiation is significantly delayed, occurring at approximately 220 seconds in the absence of inhibitors, with a peak concentration reaching about 1350 nM. The presence of ATIII further prolongs the initiation time around 340 seconds reducing the peak thrombin concentration to around 1000 nM. When both ATIII and TFPI are included, the delay becomes even more pronounced, with thrombin generation beginning at 580 seconds and the peak concentration decreasing to 890 nM approximately. These results highlight the strong regulatory role of inhibitory mechanisms under muscle contraction conditions.

Platelet activation dynamics, shown in Figures 4.7b and 4.7d, parallel the thrombin trends. Without muscle contraction (Figure 4.7b), the fraction of activated platelets (= all the platelets are activated) reaches 1 rapidly within 50 s in the absence of inhibitors. With ATIII, the activation fraction reaches at peak after 100 s, while the addition of TFPI reduces the fraction to around 0.3 after 25 s and allows another increasing to 1 from 150s to 250s. In the presence of muscle contraction (Figure 4.7d), platelet activation is slower, with peak fractions reaches 1 around 300 seconds without inhibitors and the oscillation is very large. For ATIII alone, the fraction extenda 0.3 after 380s, and with both ATIII and TFPI, the maximum fraction remains below 0.1 before 550s time.

4.3.2 Effects of anticoagulant drugs

Anticoagulant drugs can help prevent or treat DVT when normal natural inhibitors work improperly. Because the components of venous thrombosis is fibrin intead of platelets plug, anti-platelet therapy is not commonly prescribed in the treatment of (recurrent) Venous Thrombo-Embolism (VTE), and anticoagulant drugs are more effective in combatting the disease [43, 6]. Fondaparinux (Fpx) is a typical anticoagulant drug used in venous thrombosis, acting on Xa [6]. The inhibitory

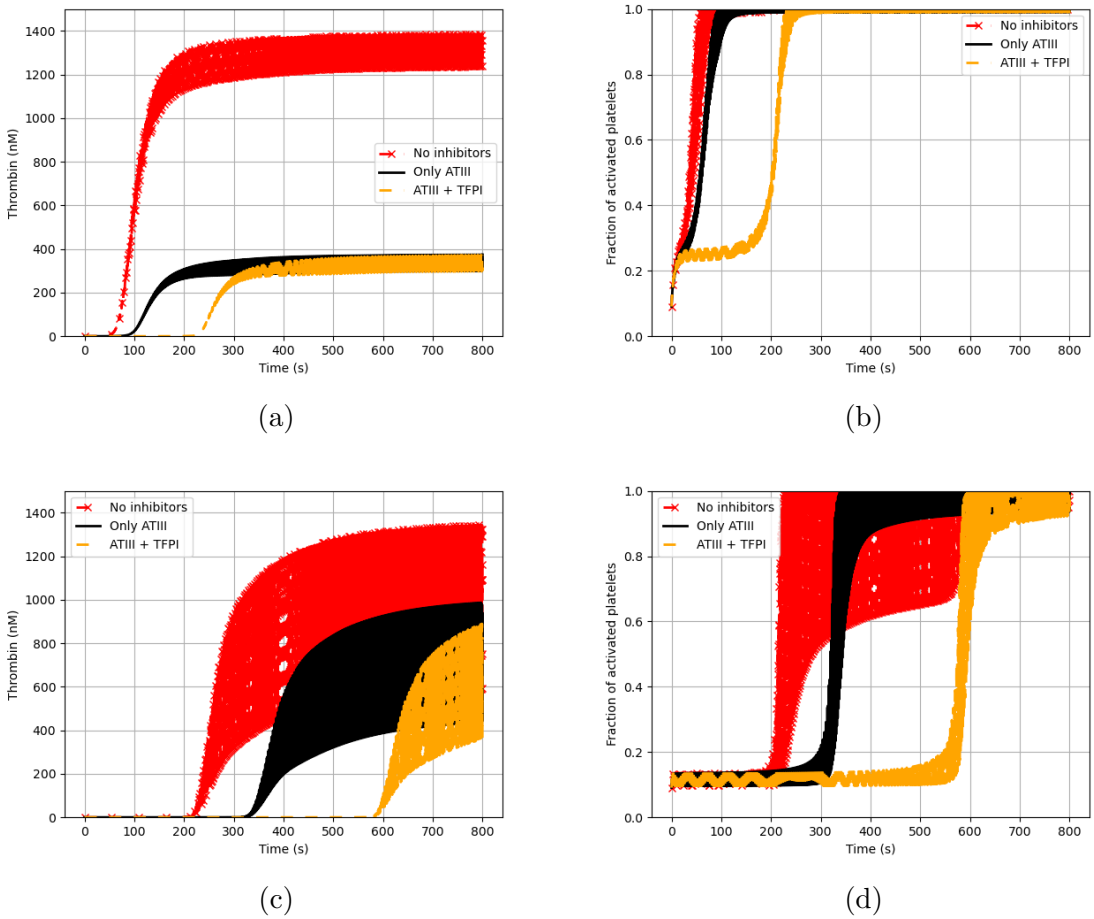

Figure 4.7: Comparison of thrombin generation under different conditions with and without muscle contraction using the platelets-based model. The model used is described in Table 4.1. (a) thrombin generation without muscle contraction; (b) platelets activation without muscle contraction; (c) thrombin generation with muscle contraction; (d) platelets activation with muscle contraction.

effects on thrombin generation in the valve was evaluated computationally. The simulations focused on the platelets-based model (Table 4.1) and the mechanism concerning Fpx is given in Table 2.15.

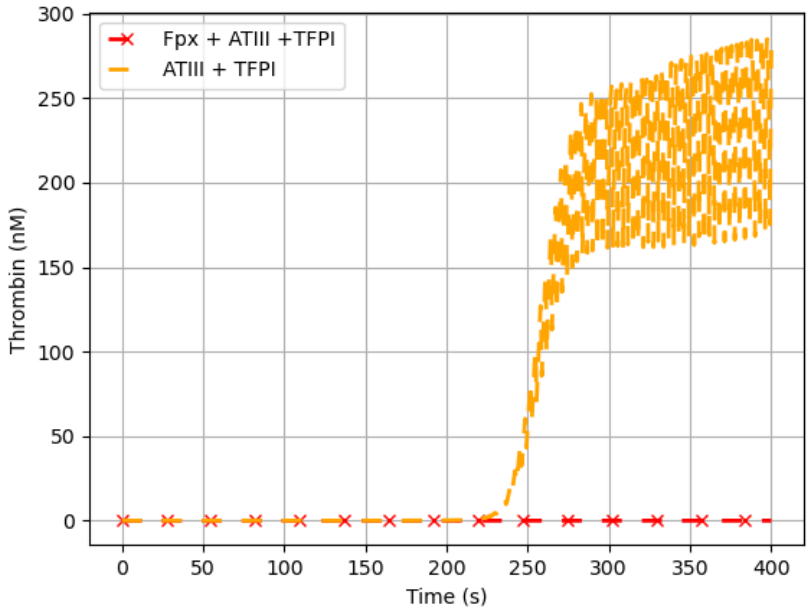

Figure 4.8: Comparison of thrombin generation between scenarios with and without Fpx. No muscle contraction and natural inhibitors function normally.

Figure 4.8 compares thrombin generation under two scenarios: with and without Fpx, regulating by natural inhibitors (ATIII and TFPI). In the presence of Fpx (100 nM), thrombin generation is completely suppressed, as indicated by the red curve. Without Fpx, thrombin generation begins before 250 seconds, with a rapid increase in concentration and oscillatory behavior, reaching peaks near 280 nM.

Notably, Fondaparinux (Fpx) primarily delays the initiation of thrombin generation rather than directly inhibiting its production, as modeled using the Fpx schemes outlined in Table 2.15. As shown in Figure 4.9, the time to 2 nM thrombin increases significantly with rising Fpx concentrations under respiratory-driven flow conditions (black line). This delay results from the anticoagulant effect of Fpx, which enhances the inhibition of factor Xa via its interaction with antithrombin (ATIII). However, this effect diminishes when the muscle pump is active. As indicated by the red line in Figure 4.9, thrombin generation time remains largely unchanged despite increasing Fpx concentrations, suggesting that the enhanced flow dynamics associated with muscle contraction override the anticoagulant's effect.

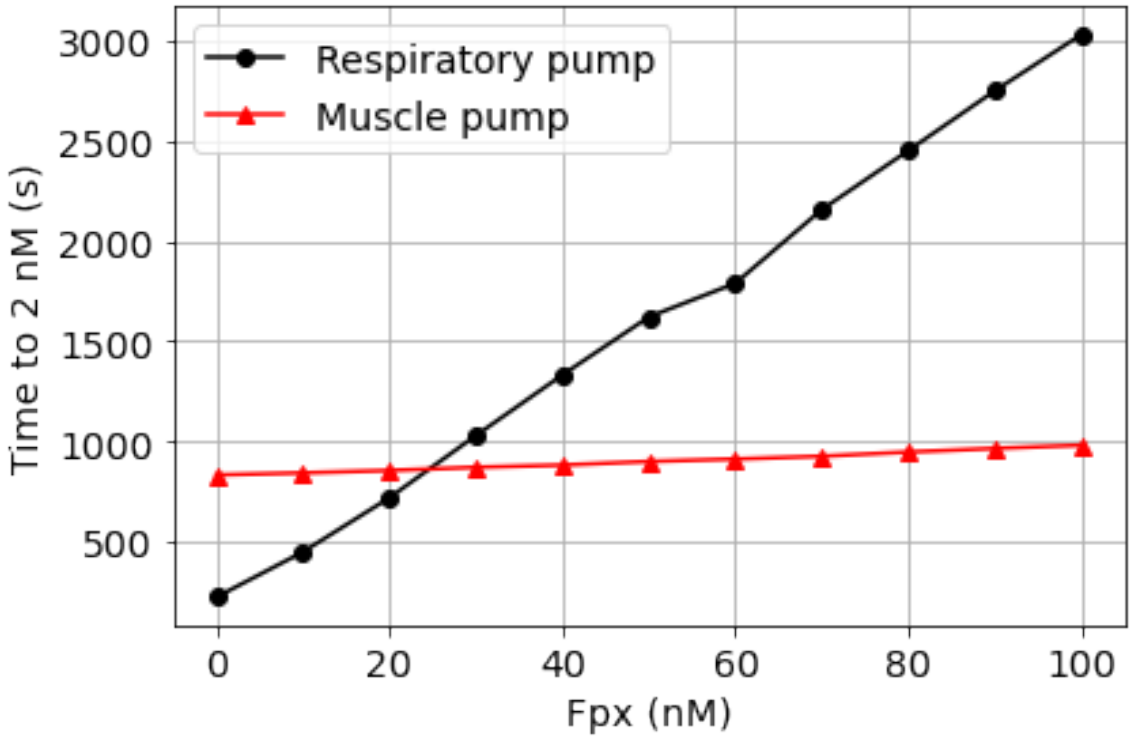

Figure 4.9: Effect of Fpx concentrations on time to 2 nM thrombin (initiation of thrombin),under blood flow driven by respiratory (black line with circle) and muscle (red line with triangle) pumps.

4.3.3 Effect of the efficiency of the mass transfer α on thrombin generation

Figure 4.10 provides insights into the effect of α on thrombin-related properties, comparing models with and without platelets. For the average thrombin concentration (Figures 4.10a and 4.10b), the no-platelets model shows a relatively (not absolutely) sharp decline in thrombin concentration as α increases, with concentrations approaching negligible levels beyond $\alpha = 0.6$. In contrast, the platelet-based model exhibits an increasing trend, with thrombin concentrations reaching approximately 400 nM at $\alpha = 1.4$. The time to steady-state oscillation (Figures 4.10c and 4.10d) reveals different dynamics as well. In the no-platelets model, the time to steady-state rapidly decreases with increasing α, which means the thrombin generation reaches steady-state faster under stronger flow. Conversely, in the platelet-based model, the time initially decreases for $\alpha < 0.4$, then sharply increases to approximately 400 seconds at $\alpha = 0.6$ before plateauing. Regarding the amplitude of steady-state oscillations (Figures 4.10e and 4.10f), the no-platelets model shows a relatively (not absolutely) rapid decline in oscillation amplitude with increasing α, with the absolute amplitudes nearing zero. On the other hand, the platelet-based model demonstrates a steady increase in oscillation amplitude, reaching an amplitude above 90 nM at $\alpha = 1.5$.

The opposite behaviors under varying α can be attributed to the fundamental differences in how thrombin generation and regulation occur in the presence and absence of platelets. In the platelets-free model, thrombin concentration declines with increasing α due to the enhanced transport effect, which results in the rapid washout of clotting factors. Beyond $\alpha = 0.6$, thrombin concentrations approach negligible levels because the reactants are mostly flushed out once entering the reaction zone. In contrast, the platelet-based model shows an increasing thrombin concentration with α due to the crucial role of platelets in amplifying coagulation. Platelets provide a surface for procoagulant reactions, particularly the assembly of the tenase (IXa=VIIIa) and prothrombinase (Xa=Va) complexes, which significantly enhance thrombin production. As α increases, moderate transport effects facilitate the continuous replenishment of clotting factors at the platelet surface without prematurely washing them away.

4.3.4 Threshold of thrombin activation

Figure 4.11 visually demonstrates how thrombin generation peaks are influenced by the tissue factor (TF) concentration and the effect coefficient (α). In figure 4.11a,

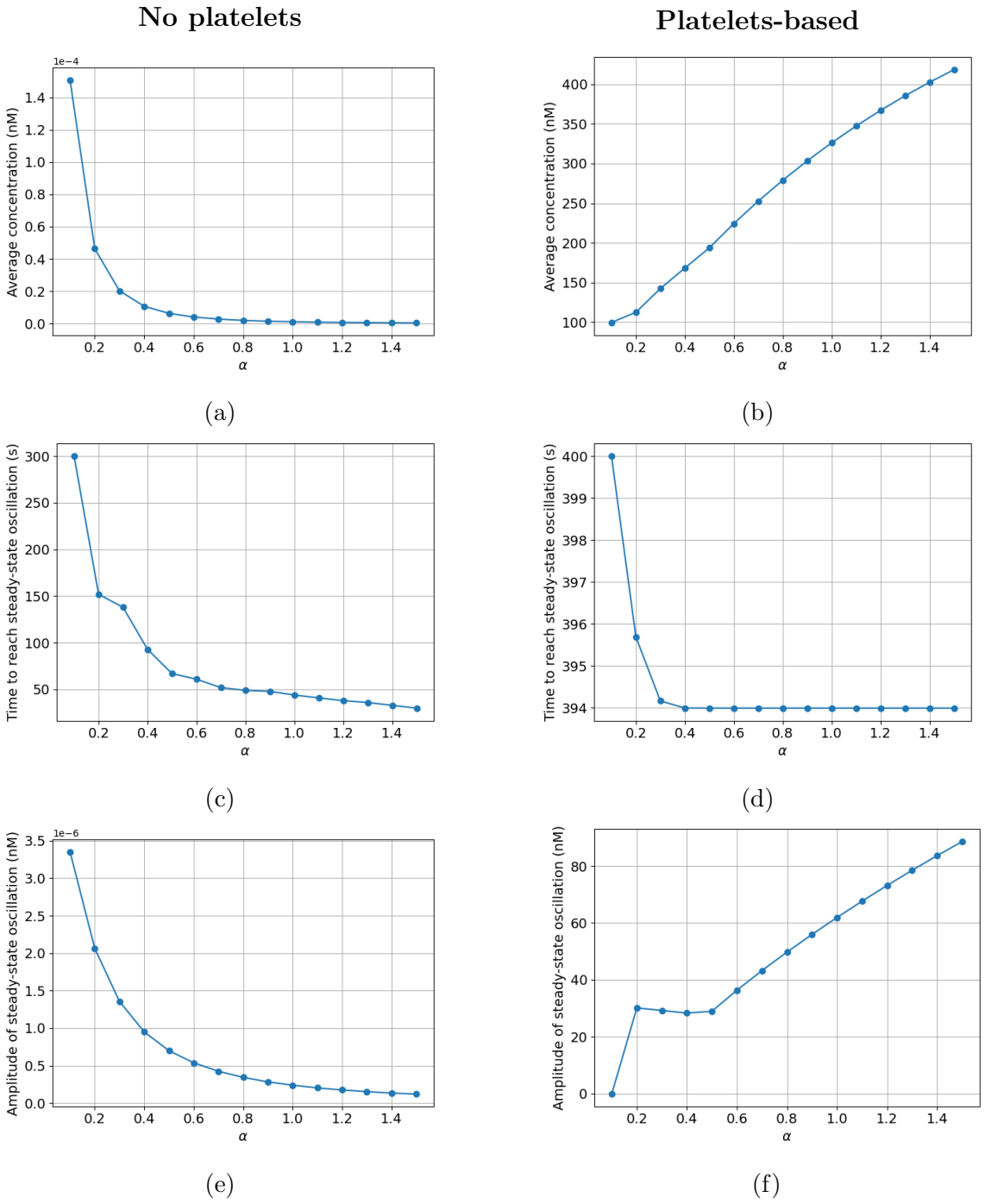

Figure 4.10: Effect of α on various thrombin-related properties in the platelet-free platelets (left column) and the platelet-based model (right column); blood flow is driven by the respiratory pump. (a) Average thrombin concentration vs α for the no platelets model. (b) Average thrombin concentration vs α for the platelet-based model. (c) Time to steady-state oscillation for the no platelet model. (d) Time to steady-state oscillation for the platelet-based model model. (e) Amplitude of oscillation vs α for the no platelet model. (f) Amplitude oscillation vs α for the platelet-based model.

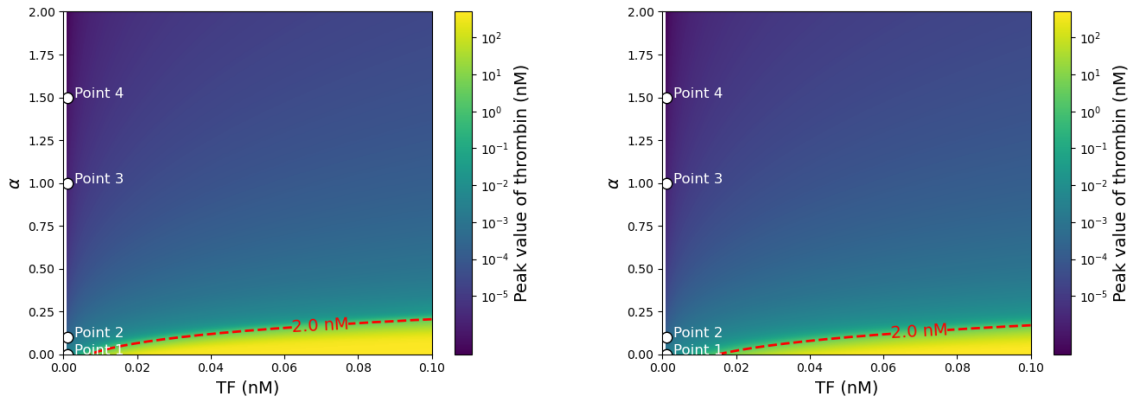

Figure 4.11: Contour representing the peak thrombin generation (nM) as a function of tissue factor (TF) concentration and the effect coefficient (α). The filled contours indicate the peak thrombin values, while the dashed red line marks the threshold of 2 nM thrombin generation. Specific points (TF = 0.001 nM, $\alpha = 0$ (Point 1), 0.1 (Point 2), 1 (Point 3), 1.5 (Point 4)) are highlighted since they correspond to simulations discussed in previous sections. under blood flow (a) driven by respiratory pump; (b) driven by calf msucle pump.

the filled contours represent the peak thrombin values across these parameters under blood flow driven by respiratory pump. The dashed red line specifically indicates the 2 nM threshold for thrombin generation, which serves as a critical marker for substantial clot formation. Figure 4.11b illustrates the peak thrombin concentrations under blood flow conditions driven by the muscle pump. Compared to Figure 4.11a, the red dashed line representing the 2 nM threshold shifts downward, indicating a reduced region where thrombin concentrations exceed 2 nM. This suggests that muscle pump activity decreases the probability of thrombin initiation. Additionally, the yellow region, which corresponds to peak thrombin values above 10 nM, is moderately smaller, also indicating the inhibitory effect of muscle pump on thrombin accumulation and clot formation. Four distinct points are labeled on the plot to represent specific parameter sets corresponding to simulations discussed earlier. Point 1 (TF = 0.001 nM, $\alpha = 0$) relates to the original model in a closed system. Point 2 (TF = 0.001 nM, $\alpha = 0.1$) and Point 4 (TF = 0.001 nM, $\alpha = 1.5$) are conditions explored in left column (No platelets) in Figure 4.10. Point 3 (TF = 0.001 nM, $\alpha = 1$) pertains to the thrombin generation in Figure 4.7a. These points emphasize the interplay between chemical stimulus (TF concentration) and effect coefficient (α), showcasing how variations in these parameters can dramatically affect thrombin production.

4.4 Conclusions

A simple 0-D model for coagulation in venous leaflets was developed and used in this chapter, using a mass transfer coefficient measured from results of 3-D model to mimick the exchanges between the sinus region and the outer flow on the first hand, and two different coagulation models for assessing the thombin dynamics on the other hand. Notably, since valve dysfunction is one of the primary contributors to deep vein thrombosis (DVT), modeling abnormal valve behavior is essential. However, this aspect is not addressed in the present thesis due to the lack of relevant and sufficient 3D simulation data.

The oscillations observed in Figure 4.6 indicate a regulatory effect of flow that prevents the over-accumulation of thrombin. The maximum thrombin values remain close to zero throughout the simulation, indicating that according to the platelet-free model, there is no significant risk of DVT as long as the venous valves are functioning properly and the TF level is normal.

Figure 4.7 underscores the critical impact of hemodynamic factors (effect coefficient; muscle contraction) on thrombin generation and platelet activation dynamics in platelet-based model. Muscle contraction slows and reduces thrombin generation and platelet activation in Figure 4.7, indicating its potential protective role against hypercoagulation. In addition, inhibitors not only lower thrombin levels and activation fractions but also delay the timing of these processes.

For clinical application, Fpx suppresses thrombin generation under normal conditions where natural inhibitors (ATIII and TFPI) are functional without muscle pump, demonstrating the value of this model in simulating DVT treatment (Figure 4.8).

In Figure 4.10, the effects of α on thrombin generation are carefully analysed. The results show that α may has different effects for different models, indicating that the selection of models is critical for simulation as well. In the platelet-free model, increasing α leads to a suppression of thrombin generation, a reduction in oscillation amplitude, and a faster convergence to steady-state conditions. This behavior can be attributed to the fact that a higher α value enhances the removal of activated coagulation factors and intermediate complex from the reaction zone, thereby limiting the accumulation of thrombin and other procoagulant species. As a result, thrombin production is significantly reduced, and the system stabilizes more rapidly.

Unlike the platelet-free model, thrombin formation in the platelet-based model shows a growing trend with increasing α. Thrombin concentration initially increases

as α rises from 0 to 1.5 due to the greater availability of platelet surface binding sites, which facilitate the assembly of procoagulant complexes and enhance localized thrombin production. In parallel, the delay time, defined as the period required to reach a critical thrombin concentration, decreases with α because increased transport accelerates the supply of clotting factors to the platelet surfaces, reducing the time needed to initiate coagulation. These findings highlight the critical role of transport dynamics in thrombosis, demonstrating that while increasing α suppresses thrombin generation in the platelet-free model, it enhances coagulation in the platelet-based model by improving reactant availability at platelet surfaces. The opposite trends indicate the 0-D model is a swift approach to assess coagulation models' practicality.

In Figure 4.11, the clear gradient underscores the sensitivity of thrombin generation to both the chemical stimulus and the effect coefficient. The findings provide predictions and insights into the mechanistic understanding of thrombin generation, which inform thrombotic risk.

Chapter 5

Conclusions and perspectives

This chapter is a summary of this thesis. Perspectives are concluded based on the results as well.

5.1 Main results

5.1.1 Chapter 2

In this thesis, The question:"How well can a coagulation model be fitted?" is answered. A comprehensive approach to optimizing coagulation models is presented, focusing on understanding the complexity of the models landscapes and identifying global minima. A key finding is that the complexity is significantly influenced by the number of variables, their selection and loss functions, even when the model structure and reactions remain unchanged.

Through the application of classical gradient-based optimization methods, it was observed that these algorithms often struggle to escape local minima, especially in complex landscapes. To overcome this challenge, a hybrid optimization strategy was developed, combining gradient-based methods with evolutionary strategies such as CMA-ES. This two-step approach was shown to be effective in navigating complex landscapes, ultimately leading to the identification of global minima.

The optimization was applied to various practical scenarios, highlighting both its strengths and limitations. When targeting experimental data, optimization with and without rate constant adjustments showed that while optimizing concentrations alone

provided moderate improvements, including rate constants yielded better alignment with experimental results. Under hemophilia A conditions, the models captured thrombin generation from experiment data at varying Factor VIII levels, yet the gaps in accuracy indicated limitations in current model structures. For anticoagulation therapy with a fixed Fondaparinux (Fpx), the optimized models performs similarly. Multi-species optimization revealed that while improvements were achieved for VIIa, the dynamics of thrombin and Xa remained largely unsatisfactory. This suggests that the typical models used in this paper cannot perfectly reflect the dynamics of multiple species at the same time.

5.1.2 Chapter 3

The multi-stage reduction strategy developed in this thesis for coagulation models has been successfully validated for both the extrinsic and intrinsic pathways. By utilizing a combination of Direct Relation Graph with Error Propagation (DRGEP), lumping techniques, the Quasi Steady State Assumption (QSSA), and conservation analysis, this approach has proven highly effective in significantly reducing the complexity of detailed coagulation models while preserving their dynamic accuracy.

When applied to both the extrinsic and intrinsic pathways models, the reduction approach simplified the models significantly. This reduced versions retained the core dynamics of thrombin generation and exhibited robust performance across varying factor VIII levels, which is essential for simulating conditions like hemophilia. This consistency validates the method's applicability and reliability. These results demonstrate the effectiveness of the multi-step, physics-informed reduction strategy in simplifying complex coagulation models while ensuring they remain accurate and robust for clinical applications.

5.1.3 Chapter 4

This chapter explored the dynamic interactions between blood flow and clotting factor concentrations within the sinus leaflets using a 0D under-flow model, revealing the impacts fo different factors on thrombin generation. It provides a detailed characterization of how changes in hemodynamics influence the temporal profiles of thrombin, offering valuable insights into the conditions under which thrombosis might occur. In this chapter, the role of platelets was also investigated. The analysis shows that platelets significantly impact the coagulation process by supporting thrombin generation through surface interactions. Additionally, it was found

that the combination of stimulus and the transport coefficient has a threshold that must be surpassed to generate considerable thrombin levels, indicating the interplay between biochemical and physical factors in coagulation. Furthermore, the functions of natural inhibitors, such as ATIII and TFPI, and anticoagulant drugs, like Fondaparinux, were analyzed. These inhibitors and drugs effectively modulate thrombin generation and prevent unregulated coagulation, demonstrating the values of numerical simulations in therapeutic applications. These findings not only enhance the understanding of valve mechanics and thrombin generation dynamics but also help potential pathways to optimize DVT treatment.

5.1.4 Summary

In conclusion, this thesis advances the computational modeling of the coagulation cascade. First, a novel hybrid optimization framework combining gradient-based and evolutionary algorithms was developed to overcome the challenge of complex landscapes. Second, a multi-step model reduction strategy was proposed to simplify coagulation networks without sacrificing predictive accuracy, enhancing both interpretability and computational efficiency. Finally, a 0-D thrombosis model of venous valves incorporating transport effects was derived from 3-D FSI simulations. This approach provides a new framework for simulating clot formation under flow, offering insights into the hemodynamic regulation of thrombosis. Moreover, Chapters 2 and 3 lay the methodological groundwork for the applications explored in Chapter 4. The reduced models and well-tuned parameters from earlier chapters can used to simulate clotting under flow conditions informed by 3-D FSI data.

Nevertheless, this work still has some limitations to be overcome. Firstly, the current optimization framework focuses only on tuning the initial concentrations of clotting factors. However, other parameters, particularly kinetic rate constants are also influential. Secondly, while the reduced models developed in this thesis have demonstrated strong performance in closed systems, they have not been systematically validated in open systems such as flowing blood environments. Thirdly, the 0-D thrombosis model assumes only ideal venous valve function. In reality, valve dysfunction plays a critical role in DVT development.

5.2 Perspectives

5.2.1 Optimization framework to include kinetic parameters

By allowing kinetic parameters to vary within physiological ranges, the model could better simulate individual patient responses to coagulation stimulus, inhibitors and treatments. This optimization would also enable the development of more accurate models under different conditions. In the practice of this thesis, we found that optimization with more freedom yields better results, as rate constants are also patient-specific. However, implementing such an approach is challenging. These parameters are difficult to measure and validate directly, and the inclusion of too many parameters introduces catastrophic complexity, making the optimization process computationally intensive and prone to uncertainties. Further research and advancements are needed to address these challenges, enabling the effective incorporation of kinetic parameter optimization into clotting factors.

5.2.2 Integration with machine learning

The integration of coagulation models with machine learning (ML) algorithms presents significant opportunities to enhance both the predictive and practical utility of these models. By combining patient datasets with ML algorithms, it becomes possible to incorporate parameters that are traditionally difficult to model mathematically, such as age, gender, smoking status, and other lifestyle factors. This allows for a more comprehensive understanding of patient-specific coagulation dynamics and the prediction. Additionally, ML can address challenges posed by chemical stiffness in complex 2-D or 3-D reaction-diffusion-advection equation models. These models often face computational difficulties due to the wide range of reaction timescales. ML-based techniques, such as surrogate modeling or neural networks, can be used to approximate the solutions of stiff equations, significantly optimize time steps while for simulation.

5.2.3 Model reduction under flow

Hemodynamics play a critical role in coagulation processes, as discussed in Chapter 4. Future work could explore whether reduced-order models of 0D models under flow are more suitable for integration with CFD than reduced-order models of 0D in closed systems. By incorporating hemodynamic effects, such as shear rates and

flow-induced transport of biochemical species, reduced models could better represent real-life cases. This approach would be significant for studying thrombus formation in complex geometries, such as venous valves or heart. Coupling these reduced models with computational fluid dynamics (CFD) simulations would enable efficient and accurate predictions of clotting behavior under different flow conditions.

5.2.4 Patient-specific modeling

While most patient-specific coagulation models researches emphasize on spatial specificity, such as the localization of thrombus formation, there is an increasing need to focus on temporal specificity. Real-time data integration is an example of this approach, where dynamic information, including blood coagulation profiles, platelet counts, and clotting factor levels, is continuously monitored through wearable devices or laboratory systems. Incorporating temporal variability allows models to reflect patient-specific changes over time, such as the evolution of coagulation dynamics during treatment or after surgical interventions.

References

[1] Anubhuti Saha, Ashutosh Bajpai, Vinay Krishna, and Shantanu Bhattacharya. Evolving paradigm of prothrombin time diagnostics with its growing clinical relevance towards cardio-compromised and covid-19 affected population. *Sensors*, 21:2636, 04 2021.

[2] Thati Madhusudhan, Bryce Kerlin, and Berend Isermann. The emerging role of coagulation proteases in kidney disease. *Nature Reviews Nephrology*, 12, 11 2015.

[3] Iqbal Jaffer. The blood compatibility challenge part 1: Blood-contacting medical devices: The scope of the problem. *Acta Biomaterialia*, 94, 06 2019.

[4] Vijay Vedula Jessica C Cardenas Peter K Henke Franck Nicoud Xiao Yun Beverley J Hunt Keefe B Manning Connor Watson, Hicham Saaid. Venous thromboembolism: Review of clinical challenges, biology, assessment, treatment, and modeling. 2024.

[5] Alexandre Ranc, Salome Bru, Simon Mendez, Muriel Giansily-Blaizot, Franck Nicoud, and Rodrigo Méndez Rojano. Critical evaluation of kinetic schemes for coagulation. *PLOS ONE*, 18(8):1–16, 08 2023.

[6] T. Orfeo, S. Butenas, K. E. Brummel-Ziedins, M. Gissel, and K. G. Mann. Anticoagulation by factor xa inhibitors. *J Thromb Haemost*, 8(8):1745–53, 2010.

[7] M. T. Stobb, K. B. Neeves, D. M. Monroe, S. S. Sindi, K. Leiderman, and A. L. Fogelson. Mathematical modeling identifies clotting factor combinations that modify thrombin generation in normal and factor viii-, ix-, or xi-deficient blood. *Res Pract Thromb Haemost*, 8(7):102570, 2024.

[8] V. Govindarajan, V. Rakesh, J. Reifman, and A. Y. Mitrophanov. Computational study of thrombus formation and clotting factor effects under venous flow conditions. *Biophys J*, 110(8):1869–1885, 2016.

[9] Rodrigo Mendez Rojano, Mansur Zhussupbekov, and James F Antaki. Multi-constituent simulation of thrombus formation at lvad inlet cannula connection: Importance of virchow's triad. *Artif. Organs*, 45(9):1014–1023, 2021.

[10] R. M. W. de Laat-Kremers, Q. Yan, M. Ninivaggi, M. de Maat, and B. de Laat. Deciphering the coagulation profile through the dynamics of thrombin activity. *Sci Rep*, 10(1):12544, 2020.

[11] Eleni Bazigou and Taija Mäkinen. Flow control in our vessels: Vascular valves make sure there is no way back. *Cellular and molecular life sciences : CMLS*, 70, 08 2012.

[12] Andrew J. Narracott. *The Venous System*, pages 127–142. Springer International Publishing, Cham, 2017.

[13] Barthelemy Thibaud. *Simulation de l'interaction fluide-structure dans les valves veineuses*. PhD thesis, Université de Montpellier, December 2024.

[14] Navaneeth Krishna Rajeeva Pandian, Brandon K Walther, Rishi Suresh, John P Cooke, and Abhishek Jain. Microengineered human vein-chip recreates venous valve architecture and its contribution to thrombosis. *Small*, 16(49):2003401, 2020.

[15] Saulius Butenas, Thomas Orfeo, Matthew T Gissel, Kathleen E Brummel, and Kenneth G Mann. The significance of circulating factor ixa in blood. *J. Biol. Chem.*, 279(22):22875–22882, 2004.

[16] A.M. Susree and B.M. Anand. Reaction mechanisms and kinetic constants used in mechanistic models of coagulation and fibrinolysis. *Math. Model. Nat. Phenom*, 11(6):71–90, 2016.

[17] Kenneth G Mann. Is there value in kinetic modeling of thrombin generation: Yes. *Journal of thrombosis and haemostasis*, 10(8):1463, 2012.

[18] Matthew F Hockin, Kenneth C Jones, Stephen J Everse, and Kenneth G Mann. A model for the stoichiometric regulation of blood coagulation. *J. Biol. Chem.*, 277(21):18322–18333, 2002.

[19] Manash S Chatterjee, William S Denney, Huiyan Jing, and Scott L Diamond. Systems biology of coagulation initiation: kinetics of thrombin generation in resting and activated human blood. *PLoS Comput. Biol.*, 6(9):e1000950, 2010.

[20] Aaron L Fogelson, Yasmeen H Hussain, and Karin Leiderman. Blood clot formation under flow: the importance of factor xi depends strongly on platelet count. *Biophys. J.*, 102(1):10–18, 2012.

[21] M. J. Owen, J. R. Wright, E. G. D. Tuddenham, J. R. King, A. H. Goodall, and J. L. Dunster. Mathematical models of coagulation-are we there yet? *J Thromb Haemost*, 22(6):1689–1703, 2024.

[22] HC Hemker, S Kerdelo, and RMW Kremers. Is there value in kinetic modeling of thrombin generation? no (unless...). *Journal of Thrombosis and Haemostasis*, 10(8):1470–1477, 2012.

[23] B. Dahlback. Blood coagulation and its regulation by anticoagulant pathways: genetic pathogenesis of bleeding and thrombotic diseases. *J Intern Med*, 257(3):209–23, 2005.

[24] Dougald Monroe, Maureane Hoffman, and Harold Roberts. Platelets and thrombin generation. *Arteriosclerosis, thrombosis, and vascular biology*, 22:1381–9, 10 2002.

[25] Jody L. Kujovich. Coagulopathy in liver disease: a balancing act. *Hematology*, 2015(1):243–249, 12 2015.

[26] Stephanie Smith, Richard Travers, and James Morrissey. How it all starts: Initiation of the clotting cascade. *Critical Reviews in Biochemistry and Molecular Biology*, 50, 05 2015.

[27] Boram Gu, Andris Piebalgs, Yu Huang, Colin Longstaff, Alun D. Hughes, Rongjun Chen, Simon A. Thom, and Xiao Yun Xu. Mathematical modelling of intravenous thrombolysis in acute ischaemic stroke: Effects of dose regimens on levels of fibrinolytic proteins and clot lysis time. *Pharmaceutics*, 11(3), 2019.

[28] Alisa Wolberg and Robert Campbell. Thrombin generation, fibrin clot formation and hemostasis. *Transfusion and apheresis science : official journal of the World Apheresis Association : official journal of the European Society for Haemapheresis*, 38:15–23, 03 2008.

[29] A. Kramoroff and J. M. Nigretto. In vitro factor xi activation mechanism according to an optimized model of activated partial thromboplastin time test. *Blood Coagulation & Fibrinolysis*, 12(4):289–299, 2001.

[30] Romy De Laat-Kremers, Tessa Peters, Rob Wagenvoord, and H. Hemker. The balance of pro- and anticoagulant processes underlying thrombin generation. *Journal of Thrombosis and Haemostasis*, 13, 11 2014.

[31] Ovilla R, Pérez F, Alvarez J, and Alvarado M. Hemophilia: review of the past and present. *Hematology & Transfusion International Journal*, 12:56–62, 08 2024.

[32] David Kumar, Erin Hanlin, Ingrid Glurich, Joseph Mazza, and Steven Yale. Virchow's contribution to the understanding of thrombosis and cellular biology. *Clinical medicine and research*, 8:168–72, 12 2010.

[33] Kerry Hitos, Mary Cannon, Stephen Cannon, Simon Garth, and John P Fletcher. Effect of leg exercises on popliteal venous blood flow during prolonged immobility of seated subjects: implications for prevention of travel-related deep vein thrombosis. *Journal of Thrombosis and Haemostasis*, 5(9):1890–1895, 2007.

[34] Peter Gloviczki and Monica L Gloviczki. Legs are a pathway to the heart: connections between chronic venous disease and heart failure. *European Heart Journal*, 42(40):4166–4168, 2021.

[35] Alexander GG Turpie. Venous thromboembolism: pathophysiology, clinical features, and prevention. *BMJ*, 325(7369):887–890, 2002.

[36] Peter Libby. Inflammation and atherosclerosis. *Circulation*, 105(9):1135–1143, 2002.

[37] Russell Ross. Atherosclerosis—an inflammatory disease. *New England Journal of Medicine*, 340(2):115–126, 1999.

[38] Björn Dahlbäck. The discovery of activated protein c resistance. *Journal of Thrombosis and Haemostasis*, 86(1):13–20, 2001.

[39] Ka Leung Chan and Cheuk Man Cheng. Hormonal contraceptives and venous thromboembolism: mechanisms, risks, and risk factors. *Thrombosis Research*, 100(3):157–165, 2000.

[40] Benjamin Rack, Brigitte Schlieter, and Stefan Janes. Cancer-associated thrombosis. *Thrombosis Research*, 114(3):201–207, 2004.

[41] Armando Tripodi. Thrombin generation assay and its application in the clinical laboratory. *Clinical Chemistry*, 62(5):699–707, 05 2016.

[42] Meera Chitlur, Geoff Rivard, and David Lillicrap. Thrombin generation assay: A powerful tool in the laboratory monitoring of von willebrand disease. *Haemophilia*, 18(3):307–314, 2012.

[43] Lana A Castellucci, Chris Cameron, Grégoire Le Gal, Marc A Rodger, Doug Coyle, Philip S Wells, Tammy Clifford, Esteban Gandara, George Wells, and Marc Carrier. Efficacy and safety outcomes of oral anticoagulants and antiplatelet drugs in the secondary prevention of venous thromboembolism: systematic review and network meta-analysis. *BMJ*, 347, 2013.

[44] S.M.C. Orfao, G. Jank, and K. Mottaghy. A new mathematical approach to modelling thrombin generation. *The International Journal of Artificial Organs*, 29(7):703–708, 2006.

[45] Sharene D. Bungay, Patricia A. Gentry, and Rodney D. Gentry. A mathematical model of lipid-mediated thrombin generation. *Mathematical Medicine and Biology: A Journal of the IMA*, 20(1):105–129, 03 2003.

[46] M E Nesheim, R P Tracy, and K G Mann. "clotspeed," a mathematical simulation of the functional properties of prothrombinase. *Journal of Biological Chemistry*, 259(3):1447–1453, 1984.

[47] M.A. Khanin and V.V. Semenov. A mathematical model of the kinetics of blood coagulation. *Journal of Theoretical Biology*, 136(2):127–134, 1989.

[48] Donghui Zhu. Mathematical modeling of blood coagulation cascade: kinetics of intrinsic and extrinsic pathways in normal and deficient conditions. *Blood Coagulation & Fibrinolysis*, 18(7):637–646, 2007.

[49] M. Anand, M. Y. Lee, and S. L. Diamond. Combining data-driven neural networks of platelet signalling with large-scale ode models of coagulation. *Sādhanā*, 43(11), 2018.

[50] Manash Chatterjee, Jeremy Purvis, Lawrence Brass, and Scott Diamond. Pairwise agonist scanning predicts cellular signaling responses to combinatorial stimuli. *Nat. Biotechnol.*, 28:727–32, 07 2010.

[51] K. Lo, W. S. Denney, and S. L. Diamond. Stochastic modeling of blood coagulation initiation. *Pathophysiol Haemost Thromb*, 34(2-3):80–90, 2005.

[52] Deyan Luan, Michael Zai, and Jeffrey D Varner. Computationally derived points of fragility of a human cascade are consistent with current therapeutic strategies. *PLoS computational biology*, 3(7):e142, 2007.

[53] G. Bocharov, A. Bouchnita, K. Bouzaachane, T. Galochkina, P. Kurbatova, P. Nony, V. Volpert, J. Clairambault, and V. Volpert. An individualized blood coagulation model to predict inr therapeutic range during warfarin treatment. *Mathematical Modelling of Natural Phenomena*, 11(6):28–44, 2017.

[54] J. L. Dunster, J. R. Wright, N. J. Samani, and A. H. Goodall. A system-wide investigation and stratification of the hemostatic proteome in premature myocardial infarction. *Front Cardiovasc Med*, 9:919394, 2022.

[55] D. Lee, S. Nayak, S. W. Martin, A. C. Heatherington, P. Vicini, and F. Hua. A quantitative systems pharmacology model of blood coagulation network describes in vivo biomarker changes in non-bleeding subjects. *J Thromb Haemost*, 14(12):2430–2445, 2016.

[56] Amor A. Menezes, Ryan F. Vilardi, Adam P. Arkin, and Mitchell J. Cohen. Targeted clinical control of trauma patient coagulation through a thrombin dynamics model. *Science Translational Medicine*, 9(371):eaaf5045, 2017.

[57] D. E. Ghetmiri, M. J. Cohen, and A. A. Menezes. Personalized modulation of coagulation factors using a thrombin dynamics model to treat trauma-induced coagulopathy. *NPJ Syst Biol Appl*, 7(1):44, 2021.

[58] A. L. Kuharsky and A. L. Fogelson. Surface-mediated control of blood coagulation: the role of binding site densities and platelet deposition. *Biophys J*, 80(3):1050–74, 2001.

[59] P. Elizondo and A. L. Fogelson. A mathematical model of venous thrombosis initiation. *Biophys J*, 111(12):2722–2734, 2016.

[60] K. Miyazawa, A. L. Fogelson, and K. Leiderman. Inhibition of platelet-surface-bound proteins during coagulation under flow i: Tfpi. *Biophys J*, 122(1):99–113, 2023.

[61] K. Miyazawa, A. L. Fogelson, and K. Leiderman. Inhibition of platelet-surface-bound proteins during coagulation under flow ii: Antithrombin and heparin. *Biophys J*, 122(1):230–240, 2023.

[62] V. I. Zarnitsina, A. V. Pokhilko, and F. I. Ataullakhanov. A mathematical model for the spatio-temporal dynamics of intrinsic pathway of blood coagulation. i. the model description. *Thromb Res*, 84(4):225–36, 1996.

[63] V.I. Zarnitsina, A.V. Pokhilko, and F.I. Ataullakhanov. A mathematical model for the spatio-temporal dynamics of intrinsic pathway of blood coagulation. ii. results. *Thrombosis Research*, 84(5):333–344, 1996.

[64] K. Leiderman and A. L. Fogelson. Grow with the flow: a spatial-temporal model of platelet deposition and blood coagulation under flow. *Math Med Biol*, 28(1):47–84, 2011.

[65] Jason Chen and Scott L. Diamond. Sensitivity analysis of a reduced model of thrombosis under flow: Roles of factor IX, factor XI, and γ-fibrin. *PLOS ONE*, 16(11):1–15, 11 2021.

[66] Z. Xu, J. Lioi, J. Mu, M. M. Kamocka, X. Liu, D. Z. Chen, E. D. Rosen, and M. Alber. A multiscale model of venous thrombus formation with surface-mediated control of blood coagulation cascade. *Biophys J*, 98(9):1723–32, 2010.

[67] E. V. Dydek and E. L. Chaikof. Simulated thrombin responses in venous valves. *J Vasc Surg Venous Lymphat Disord*, 4(3):329–35, 2016.

[68] J. Biasetti, P. G. Spazzini, J. Swedenborg, and T. C. Gasser. An integrated fluid-chemical model toward modeling the formation of intra-luminal thrombus in abdominal aortic aneurysms. *Front Physiol*, 3:266, 2012.

[69] Anass Bouchnita, Kirill Terekhov, Patrice Nony, Yuri Vassilevski, and Vitaly Volpert. A mathematical model to quantify the effects of platelet count, shear rate, and injury size on the initiation of blood coagulation under venous flow conditions. *PloS one*, 15(7):e0235392, 2020.

[70] Qudus Jimoh-Taiwo, Rashid Haffejee, and Malebogo Ngoepe. A mechano-chemical computational model of deep vein thrombosis. *Frontiers in Physics*, 10, 2022.

[71] K. N. Shankar, Y. Zhang, T. Sinno, and S. L. Diamond. A three-dimensional multiscale model for the prediction of thrombus growth under flow with single-platelet resolution. *PLoS Comput Biol*, 18(1):e1009850, 2022.

[72] Nicolas Ratto, Anass Bouchnita, Pierre Chelle, M. Marion, Mikhail Panteleev, D. Nechipurenko, Brigitte Poncet, and Vitaly Volpert. Patient-specific modelling of blood coagulation. *Bulletin of Mathematical Biology*, 83, 05 2021.

[73] A. Sagar, R. LeCover, C. Shoemaker, and J. Varner. Dynamic optimization with particle swarms (dops): a meta-heuristic for parameter estimation in biochemical models. *BMC Syst Biol*, 12(1):87, 2018.

[74] R. Wagenvoord, P. W. Hemker, and H. C. Hemker. The limits of simulation of the clotting system. *J Thromb Haemost*, 4(6):1331–8, 2006.

[75] Rodrigo Méndez Rojano, Simon Mendez, Didier Lucor, Alexandre Ranc, Muriel Giansily-Blaizot, Jean-François Schved, and Franck Nicoud. Kinetics of the coagulation cascade including the contact activation system: sensitivity analysis and model reduction. *Biomech. Model Mechanobiol.*, 18(4):1139–1153, 2019.

[76] Adithya Sagar and Jeffrey Varner. Dynamic modeling of the human coagulation cascade using reduced order effective kinetic models. *Processes*, 3(1):178–203, 2015.

[77] Kirk B Hansen and Shawn C. Shadden. Automated reduction of blood coagulation models. *Int. J. Numer. Method Biomed. Eng.*, 35, 2019.

[78] D. E. Lacroix. A reduced equation mathematical model for blood coagulation and lysis in quiescent plasma. *International Journal of Structural Changes in Solids – Mechanics and Applications*, 4:23–35, 2012.

[79] Bruce Furie and Barbara C Furie. Mechanisms of thrombus formation. *New England Journal of Medicine*, 359(9):938–949, 2008.

[80] Snehasish Ghosh, Archana Tripathi, Paramita Gayen, and Rituparna Sinha Roy. Peptide-based topical agents and intravenous hemostat for rapid hemostasis. *RSC Med. Chem.*, 11:1100–1111, 2020.

[81] Yu Guo, Min Wang, Qi Liu, Guoliang Liu, Shuang Wang, and Jiannan Li. Recent advances in the medical applications of hemostatic materials. *Theranostics*, 13:161–196, 2023.

[82] Keefe B Manning, Franck Nicoud, and Susan M Shea. Mathematical and computational modeling of device-induced thrombosis. *Curr. Opin. Biomed. Eng.*, 20:100349, 2021.

[83] C Watson, H Saaid, V Vedula, JC Cardenas, PK Henke, F Nicoud, XY Xu, BJ Hunt, and KB Manning. Venous thromboembolism: Review of clinical challenges, biology, assessment, treatment, and modeling. *Annals of Biomedical Engineering*, 52(3):467–486, Mar 2024.

[84] Sumith Yesudasan and Rodney D. Averett. Recent advances in computational modeling of fibrin clot formation: A review. *Computational Biology and Chemistry*, 83:107148, 2019.

[85] A.M. Susree and B.M. Anand. Reaction mechanisms and kinetic constants used in mechanistic models of coagulation and fibrinolysis. *Math. Model. Nat. Phenom*, 11(6):71–90, 2016.

[86] KM Ho and Warren Pavey. Applying the cell-based coagulation model in the management of critical bleeding. *Anaesth. Intensive. Care.*, 45(2):166–176, 2017.

[87] Yves Dargaud, Anne Lienhart, and Maureane Janbain. Use of thrombin generation assays to assess risk in hemophilia patients. *Thrombosis and Haemostasis*, 117(1):15–20, 2017.

[88] Armando Tripodi. Thrombin generation assay and its application in the clinical management of bleeding disorders. *Journal of Thrombosis and Haemostasis*, 14(6):1184–1189, 2016.

[89] Kathleen E Brummel-Ziedins and Alisa S Wolberg. Global assays of hemostasis. *Curr. Opin. Hematol.*, 21(5):395, 2014.

[90] Mark S. Alber, Adrian Buganza Tepole, William R. Cannon, Suvranu De, Salvador Dura-Bernal, Krishna C. Garikipati, George Em Karniadakis, William W. Lytton, Paris Perdikaris, Linda Petzold, and Ellen Kuhl. Integrating machine learning and multiscale modeling—perspectives, challenges, and opportunities in the biological, biomedical, and behavioral sciences. *NPJ Digit. Med.*, 2, 2019.

[91] Pierre Chelle, Claire Morin, Aurélie Montmartin, Michèle Piot, Michel Cournil, and Brigitte Tardy-Poncet. Evaluation and calibration of in silico models of thrombin generation using experimental data from healthy and haemophilic subjects. *Bull. Math. Biol.*, 80(8):1989–2025, 2018.

[92] Adithya Sagar and Jeffrey D. Varner. Dynamic modeling of the human coagulation cascade using reduced order effective kinetic models. *Processes*, 3(1):178–203, 2015.

[93] Gianni D'Angelo and Francesco Palmieri. Gga: A modified genetic algorithm with gradient-based local search for solving constrained optimization problems. *Inf. Sci.*, 547:136–162, 2021.

[94] M.E. Requena-Perez, A. Albero-Ortiz, J. Monzo-Cabrera, and A. Diaz-Morcillo. Combined use of genetic algorithms and gradient descent optmization methods for accurate inverse permittivity measurement. *IEEE Trans Microw. Theory. Tech.*, 54(2):615–624, 2006.

[95] Maksat Ashyraliyev, Johannes Jaeger, and Joke Blom. Parameter estimation and determinability analysis applied to drosophila gap gene circuits. *BMC systems biology*, 2:83, 10 2008.

[96] Gabriele Lillacci and Mustafa Khammash. Parameter estimation and model selection in computational biology. *PLOS Computational Biology*, 6(3):1–17, 03 2010.

[97] Ryan N Gutenkunst, Joshua J Waterfall, Fergal P Casey, Kevin S Brown, Christopher R Myers, and James P Sethna. Universally sloppy parameter sensitivities in systems biology models. *PLOS Computational Biology*, 3(10):1–8, 10 2007.

[98] Stephen G. Nash. Newton-type minimization via the lanczos method. *SIAM J Numer. Anal.*, 21(4):770–788, 1984.

[99] Ciyou Zhu, Richard H. Byrd, Peihuang Lu, and Jorge Nocedal. Algorithm 778: L-bfgs-b: Fortran subroutines for large-scale bound-constrained optimization. *ACM Trans. Math. Softw.*, 23(4):550–560, 1997.

[100] Jean Charles Gilbert. On the realization of the wolfe conditions in reduced quasi-newton methods for equality constrained optimization. *Siam Journal on Optimization*, 7:780–813, 08 1997.

[101] Christian Igel, Nikolaus Hansen, and Stefan Roth. Covariance matrix adaptation for multi-objective optimization. *Evol. Comput.*, 15(1):1–28, 2007.

[102] Gaetan K.W. Kenway, Charles A. Mader, Ping He, and Joaquim R.R.A. Martins. Effective adjoint approaches for computational fluid dynamics. *Prog. Aerosp. Sci1.*, 110:100542, 2019.

[103] Franck Nicoud. An adjoint-based method for the computation of gradients in coagulation schemes. *Int. J. Numer. Method Biomed. Eng.*, n/a(n/a):e3698, 2023.

[104] Saulius Butenas, Cornelis van 't Veer, and Kenneth G. Mann. Evaluation of the initiation phase of blood coagulation using ultrasensitive assays for serine proteases*. *Journal of Biological Chemistry*, 272(34):21527–21533, 1997.

[105] E. V. Dydek and E. L. Chaikof. Simulated thrombin generation in the presence of surface-bound heparin and circulating tissue factor. *Ann Biomed Eng*, 44(4):1072–84, 2016.

[106] R. Wagenvoord, P.W. Hemker, and H.C. Hemker. The limits of simulation of the clotting system. *Journal of Thrombosis and Haemostasis*, 4(6):1331–1338, 2006.

[107] Erik Sorensen, Greg Burgreen, William Wagner, and James Antaki. Computational simulation of platelet deposition and activation: I. model development and properties. *Annals of Biomedical Engineering*, 27:436–448, 07 1999.

[108] Quentin Cazères, Perrine Pepiot, Eleonore Riber, and Bénédicte Cuenot. A fully automatic procedure for the analytical reduction of chemical kinetics mechanisms for computational fluid dynamics applications. *Fuel*, 303:121247, 2021.

[109] Anne Felden, Perrine Pepiot, Lucas Esclapez, Eleonore Riber, and Bénédicte Cuenot. Including analytically reduced chemistry (ARC) in CFD applications. *Acta Astronautica*, 158:444–459, 2019.

[110] Simon Mendez, Alain Bérod, Christophe Chnafa, Morgane Garreau, Etienne Gibaud, Anthony Larroque, Stephanie Lindsey, Marco Martins Afonso, Pascal Mattéoli, Rodrigo Mendez Rojano, Dorian Midou, Thomas Puiseux, Julien Sigüenza, Pierre Taraconat, Vladeta Zmijanovic, and Franck Nicoud. *YALES2BIO: A General Purpose Solver Dedicated to Blood Flows*, chapter 7, pages 183–206. John Wiley & Sons, Ltd, 2022.

[111] W. T. Wu, M. A. Jamiolkowski, W. R. Wagner, N. Aubry, M. Massoudi, and J. F. Antaki. Multi-constituent simulation of thrombus deposition. *Sci Rep*, 7:42720, 2017.

[112] P. Pepiot-Desjardins and H. Pitsch. An efficient error-propagation-based reduction method for large chemical kinetic mechanisms. *Combustion and Flame*, 154(1):67–81, 2008.

[113] P. Pepiot-Desjardins and H. Pitsch. An automatic chemical lumping method for the reduction of large chemical kinetic mechanisms. *Combustion Theory and Modelling*, 12(6):1089–1108, 2008.

[114] H. Huang, M. Fairweather, J.F. Griffiths, A.S. Tomlin, and R.B. Brad. A systematic lumping approach for the reduction of comprehensive kinetic models. *Proceedings of the Combustion Institute*, 30(1):1309–1316, 2005.

[115] Casian Pantea, Ankur Gupta, James B. Rawlings, and Gheorghe Craciun. *The QSSA in Chemical Kinetics: As Taught and as Practiced*, pages 419–442. Springer Berlin Heidelberg, Berlin, Heidelberg, 2014.

[116] Chao Xu and Tianfeng Lu. An iterative dynamic chemical stiffness removal method for reacting flow simulations. *Propulsion and Energy*, 1(1):3, 2025.

[117] Jae Kyoung Kim, Krešimir Josić, and Matthew R. Bennett. The validity of quasi-steady-state approximations in discrete stochastic simulations. *Biophysical Journal*, 107(3):783–793, 2014.

[118] M.D. Ardema. Computational singular perturbation method for dynamic systems. *IFAC Proceedings Volumes*, 23(8, Part 3):409–413, 1990.

[119] U. Maas and S.B. Pope. Simplifying chemical kinetics: Intrinsic low-dimensional manifolds in composition space. *Combustion and Flame*, 88(3):239–264, 1992.

[120] T. Lovas, F. Mauss, C. Hasse, and N. Peters. Development of adaptive kinetics for application in combustion systems. *Proceedings of the Combustion Institute*, 29(1):1403–1410, 2002.

[121] Christine Reder. Metabolic control theory: A structural approach. *Journal of Theoretical Biology*, 135(2):175–201, 1988.

[122] Thomas J Snowden, Piet H van der Graaf, and Marcus J Tindall. Methods of model reduction for large-scale biological systems: a survey of current methods and trends. *Bulletin of mathematical biology*, 79:1449–1486, 2017.

[123] Ravishankar Rao Vallabhajosyula, Vijay Chickarmane, and Herbert M Sauro. Conservation analysis of large biochemical networks. *Bioinformatics*, 22(3):346–353, 2006.

[124] Davide Castaldi, Daniele Maccagnola, Daniela Mari, and Francesco Archetti. Stochastic simulation of the coagulation cascade: A petri net based approach. Euro-Par 2012: Parallel Processing Workshops, pages 248–262. Springer Berlin Heidelberg, 2012.

[125] G.E. Rivard, K.E. Brummel-Ziedins, K.G. Mann, L. Fan, A. Hofer, and E. Cohen. Evaluation of the profile of thrombin generation during the process of whole blood clotting as assessed by thrombelastography. *Journal of Thrombosis and Haemostasis*, 3(9):2039–2043, 2005.

[126] M.D. Silverstein, J.A. Heit, D.N. Mohr, T.M. Petterson, W.M. O'Fallon, and L.J. Melton. Trends in the incidence of deep vein thrombosis and pulmonary embolism: A 25-year population-based study. *Archives of Internal Medicine*, 158(6):585–593, 1998.

[127] J.A. Heit, F.A. Spencer, and R.H. White. The epidemiology of venous thromboembolism. *Journal of Thrombosis and Thrombolysis*, 41(1):3–14, 2015.

[128] G.E. Raskob, P. Angchaisuksiri, A.N. Blanco, H. Buller, A. Gallus, B.J. Hunt, E.M. Hylek, A. Kakkar, S.V. Konstantinides, M. McCumber, Y. Ozaki, A. Wendelboe, J.I. Weitz, and ISTH Steering Committee for World Thrombosis Day. Thrombosis: A major contributor to global disease burden. *Arteriosclerosis, Thrombosis, and Vascular Biology*, 38(5):1042–1053, 2018.

[129] C. Kearon, E.A. Akl, J. Ornelas, A. Blaivas, D. Jimenez, H. Bounameaux, M. Huisman, C.S. King, T.A. Morris, N. Sood, S.M. Stevens, J.R. Vintch, P. Wells, S.C. Woller, and L. Moores. Antithrombotic therapy for vte disease: Chest guideline and expert panel report. *Chest*, 149(2):315–352, 2016.

[130] Akshita Rana, Erik Westein, Be'eri Niego, and Christoph E. Hagemeyer. Shear-dependent platelet aggregation: Mechanisms and therapeutic opportunities. *Frontiers in Cardiovascular Medicine*, 6, 2019.

[131] F. Lurie, R.L. Kistner, B. Eklof, and D. Kessler. Mechanism of venous valve closure and role of the valve in circulation: A new concept. *Journal of Vascular Surgery*, 38(5):955–961, 2003.

[132] Thibaud Barthelemy, Ines Noguero Soler, Simon Mendez, and Franck Nicoud. Fluid-structure interaction modeling of deep vein valves. In *7th International Conference on Computational & Mathematical Biomedical Engineering*, volume 2, pages 672–675, July 2022.

[133] Milka Koupenova, Beate E. Kehrel, Heather A. Corkrey, and Jane E. Freedman. Thrombosis and platelets: an update. *European Heart Journal*, 38(11):785–791, 12 2016.

[134] Marco Heestermans, Géraldine Poenou, Anne-Claire Duchez, Hind Hamzeh-Cognasse, Laurent Bertoletti, and Fabrice Cognasse. Immunothrombosis and the role of platelets in venous thromboembolic diseases. *International Journal of Molecular Sciences*, 23(21), 2022.

[135] Kenneth G. Mann. Thrombin generation in hemorrhage control and vascular occlusion. *Circulation*, 124(2):225–235, 2011.